

Synthesis & optical properties of novel rare earth-doped aluminate nanophosphors

Su, Liap Tat

2008

Su, L. T. (2008). Synthesis & optical properties of novel rare earth-doped aluminate nanophosphors. Doctoral thesis, Nanyang Technological University, Singapore.

<https://hdl.handle.net/10356/13536>

<https://doi.org/10.32657/10356/13536>



**NANYANG
TECHNOLOGICAL
UNIVERSITY**

**SYNTHESIS & OPTICAL PROPERTIES OF NOVEL
RARE EARTH-DOPED ALUMINATE
NANOPHOSPHORS**

SU LIAP TAT

SCHOOL OF MATERIALS SCIENCE AND ENGINEERING

2008

SYNTHESIS & OPTICAL PROPERTIES OF NOVEL RARE
EARTH-DOPED ALUMINATE NANOPHOSPHORS

SU LIAP TAT

2008

**SYNTHESIS & OPTICAL PROPERTIES OF NOVEL
RARE EARTH-DOPED ALUMINATE
NANOPHOSPHORS**

SU LIAP TAT

School of Materials Science and Engineering

A thesis submitted to the Nanyang Technological University
in fulfillment of the requirement for the degree of
Doctor of Philosophy

2008

Acknowledgements

I would first like to thank the School of Materials Science and Engineering (MSE) for giving me the opportunity to work on this doctorate in the field of nanophosphors as well as for granting me the research fees waiver. In addition, I am also thankful to Advanced Material Resources (Europe) Ltd, UK for providing me financial help.

I would like to express my sincere appreciation to Assistant Professor Alfred Tok Iing Yoong, my research advisor. I benefited tremendously from my interaction with him and greatly appreciate his advice and guidance throughout my studies. He gave me the freedom and resources to pursue my research, supported, and encouraged me constantly.

I am also indebted to Associate Professor Tim White, Assistant Professor Zhili Dong, Assistant Professor Madhavi Srinivasan, Dr. Cristiano Ferraris, Dr. Martin Schreyer and Ms. Guo Jun who imparted their knowledge in crystallography, transmission electron microscopy, x-ray photoelectron spectroscopy and x-ray diffraction to me. I appreciate Mr. Nathaniel Ng for his help in the modeling work, and Mdm. Chan Soon Keng for proofreading this thesis. I would also like to thank the technical staff in the ceramic processing laboratory, especially Mr. Samsudin Bin Sarim for his help in the lab, and Dr. Sun Xiaolong for his friendship and support.

I would like to thank Dr. Jim L. Woodhead (Advanced Material Resources (Europe) Ltd, UK) who imparted his knowledge and skills in the areas of synthesis and chemistry to me during my training attachment (EDB-TAP program) with the company prior to this doctorate studies. I also appreciate Mr. Paul Doleman (Advanced Material Resources (Europe) Ltd, UK) for his help and support.

Lastly, I would like to thank my wife, Danyi, for her constant love and support. I want to thank her for understanding when I had to spend all my time preparing for exams and writing this thesis. I want to thank my baby girl, Jiayu, who brought laughter and tremendous fun to our family, and for introducing me to the reality and fun of parenting. I thank my parents-in-law who have taken good care of Jiayu so that I could concentrate on my studies. Last, but not least, I thank my parents for always loving me for who I am and giving me the help when I needed it the most.

Table of Contents

Acknowledgements	2
Table of Contents	4
List of Tables	6
List of Figures	6
Abstract	9
Chapter 1: Introduction	11
1.1 Background	11
1.2 Motivations	13
1.3 Aim of the study	15
1.4 Objectives	15
Chapter 2: Literature Review	18
2.1 Synthesis of Cerium doped YAG	19
2.1.1 Synthesis of the bulk phosphors (micron-sized)	19
2.1.2 Synthesis of the nanophosphors (<200 nm)	21
2.1.3 A lack of YAG: Ce ³⁺ with sizes of less than 10 nm	25
2.1.4 Synthesis of the nanophosphors with particle sizes < 10 nm	25
2.2 Optical Properties of the Cerium doped YAG phosphors	31
2.2.1 Electronic structure of YAG: Ce ³⁺ in the bulk state	32
2.2.2 A lack of the size-dependent optical studies for YAG: Ce ³⁺	36
2.2.3 Configurational Coordinate Diagram	36
2.2.4 Factors to be considered in the size-dependent optical study	40
2.2.5 The Brownian oscillator (BO) model	49
2.3 Summary	51
Chapter 3: Experimental Procedures	53
3.1 Introduction	53
3.2 Synthesis of the 30 nm nanophosphors via the chemical gelation	54
3.3 Synthesis of the 5 nm nanophosphors via the solvothermal method	55
3.4 Synthesis of the 250 nm nanophosphors via the solvothermal method	56
3.5 Characterisation of the chemical, physical and optical properties	57
3.6 The multimode Brownian oscillator model	63

3.7	Summary	64
Chapter 4: Results & Discussion		65
4.1	Synthesis of YAG: Ce ³⁺ nanophosphors via a chemical gelation	66
4.1.1	Crystallisation of YAG: Ce ³⁺ nanophosphors	67
4.1.2	Characterization of the YAG: Ce ³⁺ spherical particles	73
4.1.3	Polycrystalline to single crystal	80
4.1.4	HRTEM analysis of the single-crystal particle	84
4.1.5	Summary	87
4.2	Synthesis of YAG: Ce ³⁺ nanophosphors via a solvothermal method	88
4.2.1	Characterisation of the nanophosphor with a size of 5nm	89
4.2.2	Characterisation of the near cubic shaped nanophosphors with a size of 250 nm	96
4.2.3	Structural comparison between the undoped & Ce ³⁺ -doped YAG nanophosphors	106
4.2.4	Summary	110
4.3	Structural characterisation of YAG: Ce ³⁺ bulk phosphors	111
4.4	Optical Properties of YAG: Ce ³⁺	113
4.4.1	A comparison between the bulk and nanophosphors	114
4.4.2	Investigation of the surface defective sites	121
4.4.3	Investigation of the size-dependent electron-phonon coupling	126
4.4.4	Summary	130
Chapter 5: Conclusions & Recommendations		131
5.1	Synthesis of the YAG: Ce ³⁺ nanophosphors via the chemical gelation	131
5.2	Synthesis of YAG: Ce ³⁺ nanophosphors via solvothermal method	132
5.3	The size-dependent optical properties of YAG: Ce ³⁺	133
5.4	Recommendations for future work	134
References		136
Appendix A: Crystallography of YAG: Ce ³⁺		153
Appendix B: The Brownian oscillator model		160

List of Tables

Table 4-1: Theoretical and observed weight loss	Page 69
Table 4-2: Comparison of the FTIR bands (cm^{-1}) for organic capped nanophosphor, oleylamine, and oleic acid	95
Table 4-3: Spectra comparison between the bulk and nanophosphors	118
Table 4-4: Parameters used in the BO model	127

List of Figures

Figure 2-1: A general concept of phosphor synthesis process	Page 20
Figure 2-2: A two-microemulsion method in synthesizing CdSe nanocrystal	27
Figure 2-3: Energy level of Ce^{3+} in YAG	33
Figure 2-4: Luminescence spectra of $\text{YAG}:\text{Ce}^{3+}$	35
Figure 2-5: A configurational coordinate diagram [1]	37
Figure 2-6: The structures and Stokes shifts of the [2.2.1] and [2.2.2] cryptand ligands encapsulating a cerium ion (purple)[2]	42
Figure 2-7: A comparison of the Stokes shifts of the $[\text{Ce} \subset 2.2.1]^{3+}$ and $[\text{Ce} \subset 2.2.2]^{3+}$ based on the displacement of the configurational coordinate diagram	43
Figure 4-1: TG/DTA of the gel particles	68
Figure 4-2: XRD pattern of Ce^{3+} doped YAG	71
Figure 4-3: Crystallite sizes and surface areas as a function of temperatures	75
Figure 4-4: FESEM micrographs of $\text{YAG}:\text{Ce}^{3+}$ calcined at 900°C	76
Figure 4-5: FESEM micrographs of $\text{YAG}:\text{Ce}^{3+}$ calcined at 1000°C	77

Figure 4-6: FESEM micrographs of YAG: Ce ³⁺ calcined at 1300°C	78
Figure 4-7: (a) TEM image of the nanophosphors and TEM image at higher magnification (insert) (b) Particle size distributions of the nanophosphors	79
Figure 4-8: Particle size distributions of the chemical gelated YAG: Ce ³⁺	80
Figure 4-9: Formation of a pore within a grain [3]	81
Figure 4-10: (a) TEM of a single crystal nanoparticle; insert is the SAED of the selected particle <100> (indicated by the red circle) (b) HRTEM micrograph of the particle	82
Figure 4-11: FESEM micrographs of YAG: Ce ³⁺ calcined at 1600°C	83
Figure 4-12: FESEM micrographs of the commercially-available YAG: Ce ³⁺	83
Figure 4-13: (a) HRTEM image and (b to e) simulated images (Key: Y ³⁺ (red) ; Al(1) ³⁺ octahedrals (blue) ; Al(2) ³⁺ tetrahedrals (green) ; O ²⁻ (light blue))	85
Figure 4-14: Calculated HRTEM image via the Multislice method	87
Figure 4-15: A core-shell structure [4]	90
Figure 4-16: (a) TEM image of the nanophosphor and (b) its particle size distributions	92
Figure 4-17: (a) HRTEM of the nanophosphor (b) Observed and simulated electron diffraction patterns of the nanophosphor	93
Figure 4-18: FTIR spectrum for the organic capped nanophosphors	94
Figure 4-19: a C-C bond formation route [5]	99
Figure 4-20: (a) The branched oligomeric clusters and the electron diffraction pattern (insert)	100
Figure 4-21: The aggregation of nanoparticles and the electron diffraction pattern (insert)	101
Figure 4-22: XRD patterns of (a) YAG: Ce ³⁺ nanophosphor with incomplete crystallization (b) YAG: Ce ³⁺ nanophosphor with a size 250 nm (c) undoped YAG nanoparticle (d) ICSD#93634 [6]	102

Figure 4-23: (a) Nanophosphors with near cubic shaped (b) The particle size distributions	103
Figure 4-24: TEM images of the 250 nm nanophosphors	103
Figure 4-25: (a) A cubic single-phase nanophosphor and the electron diffraction pattern (insert) (b) HRTEM images of the particle's truncated corner	105
Figure 4-26: Nanophosphors with single crystal phase and the electron diffraction pattern (insert)	106
Figure 4-27: HRTEM images of the nanoparticle	107
Figure 4-28: (a) TEM images of the undoped YAG nanoparticles (b) The particle size distributions	107
Figure 4-29: (a) The small-angle electron diffraction pattern of the cubic array (b) A self-assembly cubic array	108
Figure 4-30: The Rietveld refined XRD pattern of the bulk phosphors	111
Figure 4-31: (a) FESEM image of the bulk phosphor (b) Its particle size distributions (c) TEM image of the phosphors (d) Electron diffraction pattern of (c) image (e) Simulated HRTEM image (f) Simulated electron diffraction pattern of (e) image (g) HRTEM image of (c)	113
Figure 4-32: High resolution curve fitted (solid lines) XPS spectrum of Ce 3d showing spin-orbit splitting ($3d_{5/2}$, $3d_{3/2}$)	115
Figure 4-33: PL and PLE spectra of the bulk and nanophosphors	117
Figure 4-34: (a) HRTEM image of the nanophosphor surfaces (b) A simulated HRTEM image (c) Atomic projection by the Multislice method (d) Atomic projection by ATOMS	122
Figure 4-35: FTIR spectrum of the nanophosphors	125
Figure 4-36: Measured and calculated spectra	128

Abstract

The potential of rare earth doped nanophosphors makes them appealing for a myriad of important applications such as white light emitting diodes (LEDs), displays, lasers, fluorescent labels, and solar cells. While the preparation of rare earth doped nanophosphors is a challenging task, it is technologically beneficial to produce nanoscale phosphors and to understand their size-dependent optical properties in order to support more opportunities for new applications. Currently, cerium-doped yttrium aluminum garnet (YAG: Ce³⁺) is the most complex oxide and its unique optical property makes it an ideal material for this study. However, there are problems in synthesizing the YAG: Ce³⁺ nanophosphors, especially the lacking in an approach to produce the nanophosphor with a size of less than 10 nm, and furthermore, not much is known about its size-dependent optical properties like the coupling strength of an electron-lattice relaxation.

This study aims to synthesize highly crystalline YAG: Ce³⁺ nanophosphors with particle sizes targeted at less than 10 nm, 100 nm, and 300 nm and study the size effects on the optical properties of YAG: Ce³⁺.

In order to resolve the synthesis problems, the solvothermal and chemical gelation methods were sought. All samples were characterized with respect to their physical, chemical, and optical properties with the objective to elucidate the size-dependence of the optical properties of YAG: Ce³⁺.

YAG: Ce³⁺ nanophosphors with sizes of 30 nm and both 5 nm and 250 nm were synthesized by chemical gelation and solvothermal method, respectively. The size-dependence of the optical properties of YAG: Ce³⁺ was manifested in the blueshift of emission peaks due to the reduction in the Stokes shift and covalency. The surface defects of the nanophosphors were determined by the high resolution transmission electron microscopy (HRTEM) to be the incomplete garnet lattices and nonbridging oxygen. These surface defects caused the poor luminescence efficiency observed in the nanophosphors as compared to that in the bulk sample. The results of the size-dependent electron-phonon coupling investigated through fitting the measured photoluminescence spectra within the framework of the Brownian oscillator (BO) model showed that the coupling strength decreased with reducing in phosphor sizes.

In conclusion, YAG: Ce³⁺ nanophosphors were successfully synthesized and achieved the target sizes through the chemical gelation and solvothermal methods. Their optical responses showed a size-dependence phenomenon and the factors that influenced the energy shift were attributed to the Stokes shift, covalency, surface states, and electron-phonon coupling. A good agreement between theory and experiment was obtained indicating a successful application of the BO model to explain the emission broad band of YAG: Ce³⁺.

Chapter 1: Introduction

1.1 Background

Nanophosphors are recently attracting much attention from academia and industry owing to the unique properties of the nanoscale regime. These properties do not simply arise from the scaling factor and may change with the phosphors size or shape [7]. For example, in semiconductor nanocrystals, the change in their optical properties is due to the confinement of electronic motion when the material's length scale is comparable or smaller than the electron Bohr radius of the bulk semiconductor material. Another example is the surface plasmon absorption phenomenon that causes the noble metal nanoparticles to appear with an intense colour.

Nanophosphors that are doped with rare earth ions are technologically important materials in display, lighting, lasers and a variety of other attractive applications [2, 8-11]. Currently, one application that drives the development of the nanophosphors is the production of white light emitting diodes (LEDs), which are in high demand for solid-state lighting (SSL) and back-light units (BLU) in displays [12]. Researchers and experts in academia and industry have been making consistent efforts to develop nanophosphors that are more efficient than the bulk materials in converting the source light (blue or UV-LEDs) into the desired white emission. This is an important research field because the success in it could further improve the performance and energy efficiency of white LEDs (or

better than the general lighting such as incandescent and fluorescent lamps) and could potentially reduce global consumption of electricity [13]. (It is interesting to note that global electricity use for lighting is estimated to be 20% of the total [13, 14])

Apart from the potential in achieving the enhanced efficiency by using the nanoscale phosphors, a few optical and structural properties such as a broad absorption spectrum, high concentration quenching limit, low coupling to phonons, dopant on a single crystallographic site, and regular particle morphology are expected to meet the requirements specified by the major white LEDs manufacturers [15]. Therefore, more efforts should be devoted to the synthesis and understanding of the optical phenomenon of the nanophosphors.

Fluorescent labelling by the rare earth doped nanophosphors for biological studies and clinical applications is of interest to academia and industry [16]. They are excellent up-conversion nanomaterials as they present large Stokes shifts, long fluorescence lifetimes, and their emissions are photostable and are generally sharp due to the intra $4f$ configuration of the rare earth dopants. In addition, their surfaces can be easily modified while maintaining their optical properties, making them suitable for use as biolabels. As such, their rapid developments have led them to the usage such as immunoassay [17], time-resolved fluorescence imaging [18], specific targeting [19], and DNA detection [20].

Another important area is in solar cell applications. The increasing awareness of limited energy resources on earth has initiated many investigations in

search of alternative means of renewable energy supply. While solar energy is an important source of clean energy, the efficiency of the current solar cell technology is still lower than fossil and nuclear sources technologies. Fortunately, many materials-based solutions are available to overcome this deficiency. One example is to couple the rare earth doped nanophosphors, an excellent up-conversion materials, with solar cells [21-26]. The nanophosphors are transparent colloids which can be coated easily on the cells to act as a luminescent layer that can absorb infrared radiation from the solar spectrum and emit as visible lights. By exciting electron-hole pairs across the cell, the emitted energy is able to provide an additional excitation (in addition to that occurring in silicon solar cells) that could enhance the solar cell's energy conversion efficiency.

1.2 Motivations

Since the synthesis of nanoscale materials is an important research field in nanoscience and nanotechnology, many research efforts have been devoted to producing high quality nanomaterials with more reliable, economical, and environmental friendly methods. However, the emphasis has been mainly on the synthetic methods for semiconductor nanocrystals and relatively less on rare earth doped nanophosphors with complex crystal structures. This is because the preparation of rare earth doped nanophosphors is a highly challenging task. For example, cerium-doped yttrium aluminium garnet (YAG: Ce^{3+}) requires high energy to overcome crystallization barriers and thus, achieving a pure garnet phase is generally very complex. Conventionally, YAG is synthesized by a solid-state reaction method which requires the heat treatment temperature above 1400 °C, but

this high reaction temperature would promote crystal growth into larger particle sizes, which is not favorable for the synthesis of nanomaterials. Furthermore, synthesizing nanophosphors with well-defined properties, such as controlled particle sizes and distributions as well as a controlled morphology, is an additional challenge to the preparative chemistry. Therefore, a material with a complex crystal structure is an ideal model for the study.

In this study, YAG was chosen because it belongs to the garnet family, which is probably the most complex crystal among all known oxides. Moreover, qualities such as low thermal expansion, high optical transparency, low acoustic loss, high threshold for optical damage, high hardness, and chemical and mechanical stability [27, 28] make the YAG an important solid-state laser host material. When it is doped with rare earth ion such as neodymium, it presents ideal spectroscopic properties as a laser material. YAG is also known for its creep resistance and is used in high temperature ceramic composites [29]. Currently, YAG: Ce³⁺ is an important phosphors material for white LEDs because its absorption lies in the emitting spectrum of the source light (or blue LEDs). And because of its strong blue absorption, YAG:Ce³⁺ is potentially useful for fluorescent labelling in biological systems as it can avoid the UV excitation and reduce the auto-fluorescence background [30].

In summary, it is technologically beneficial to produce cerium-doped YAG materials in nanosizes and to understand the size-dependence of their optical properties in order to support applications in diverse fields such as quantum electronics, non-linear optics, and photonics. It is notable that although the

synthesis of YAG: Ce³⁺ nanophosphors is difficult, it is equally rewarding because its success would provide a much-needed methodology to synthesize nanomaterials with complex crystal structures.

1.3 Aim of the study

The main aim of this study is to synthesize highly crystalline cerium doped yttrium aluminium garnet (YAG: Ce³⁺) nanophosphors with particle sizes targeted at less than 10 nm, 100 nm, and 300 nm and study the size effects on the optical properties of YAG: Ce³⁺.

1.4 Objectives

The study undertakes to achieve the following objectives as outlined below:

1. A synthetic method based on the emulsion technique is developed to produce the nanophosphors with a targeted size of less than 100 nm and at a much lower temperature than that required in a solid-state reaction method. This study involves a thorough understanding of the crystallisation process of the garnet crystal that linked the nature of the gel particles to their various stages of thermal behavior. The study is further extended to investigating the state of nuclei flocculation, the behavior of crystal growth, and the conservation of particle morphology at high temperatures.

2. An alternative synthetic method based on a nonhydrolytic approach is developed with the objective to obtain as synthesized YAG: Ce³⁺ with target sizes of less than 10 nm and 300 nm. This emphasis resolves the problem of crystal growth due to the post heat treatment process at high temperatures. Then, we seek to understand the formation of the nanophosphors with a controlled morphology through the usage of various precursors and with the aid of various capping agents, and we study the role of the cerium dopant plays in the formation of the nanophosphors.

3. Characterization of the structural properties of both the bulk and nanophosphors, such as crystallinity and atomic distributions (in particular to the surfaces of the nanophosphors), is discussed.

4. The size effects on the optical properties of the nanophosphors are studied and discussed. This fundamental study would involve an understanding of the size-dependence of the photophysical process relating to the structures and surface defects. Together with a theoretical model, this understanding is extended to account for the electron-phonon coupling with the purpose of elucidating the phonon relaxation and the coupling strength.

In summary, in order to achieve the research objectives in this study, two different synthesis methods based on the emulsion and solvothermal technique, respectively, are used to produce the nanophosphors with targeted sizes. All samples are characterized with respect to their physical, chemical, and optical properties with the objective to elucidate the size-dependence of the optical

properties of YAG: Ce³⁺. The physical insight of Ce³⁺ optical responses is further be unveiled by a theoretical model in particular on the size-dependence of the electron-phonon coupling strength.

In Chapter 2, the progress of related research is identified and discussed, and the areas that require further research works are highlighted. In Chapter 3, the synthesis and characterization procedures are presented. The results are presented and analysed critically in Chapter 4. Lastly, the research findings are summarized and recommendations for future studies are made in Chapter 5.

Chapter 2: Literature Review

Ce^{3+} doped yttrium aluminium garnet (YAG: Ce^{3+}) was first discovered by Blasse and Bril [31] in the early seventies. This finding excited the phosphor community because the emission of cerium ion in YAG host material is in the visible region of the electromagnetic spectrum, and unlike other Ce^{3+} activated phosphors, their emission spectra usually appeared in the high energy range, such as in the UV and blue [32, 33]. Currently, the YAG: Ce^{3+} nanophosphors have attracted much attention from the industry and academia due to their uses in a myriad of important applications (as highlighted in Chapter 1). However, there are problems in synthesizing the YAG: Ce^{3+} nanophosphors and still not much is known on the size-dependence of the optical properties, especially the electron-lattice relaxation process in the nanophosphors.

In this chapter, a review of work in the nanophosphors syntheses, size effects on the optical properties, and theoretical framework to model the observed optical responses is conducted with the objective to identify and discuss the progress made so far, and to highlight the areas that require further works. The review reports first on the syntheses of the nanophosphors and then the size-dependence of their optical properties.

2.1 Synthesis of Cerium doped YAG

The synthesis of YAG: Ce³⁺ is a challenging task and usually requires a very high reaction temperature in the solid-state reaction method to achieve a pure garnet phase. However, the solid-state reaction is a difficult and laborious method. Thus, there is a strong motivation to synthesize the material at a much lower temperature. Some of the significant synthesis methods are reviewed in this section.

2.1.1 Synthesis of the bulk phosphors (micron-sized)

Ropp [34] has described a detailed process for the manufacturing of YAG: Ce³⁺. The raw materials for the material formulation are yttrium oxalate hydrate, aluminium oxide, and cerium carbonate. They are blended and milled twice with blending in between. These mixed powders are then calcined at 1450 °C for 6 hours in air. After the heat treatment, the powders are crushed, milled, and sieved through a 325 mesh screen, so that free-flowing powders are obtained. The oxide powders are heat treated again at 1150 °C for 4 hours in 95% N₂ – 5% H₂ environment to ensure the cerium ion is stabilized in a trivalent state. This high temperature solid-state reaction method was summarized by Narita [35] (cf. in Figure 2-1).

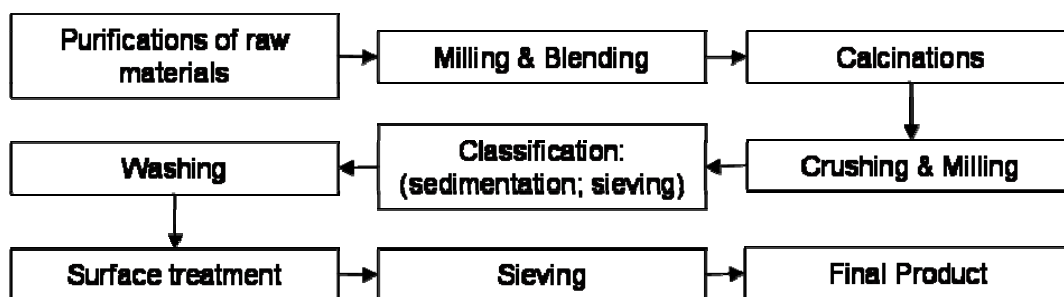


Figure 2-1: A general concept of phosphor synthesis process

Narita further highlighted the importance of fluxes (such as alkali or alkali-earth halides) in accelerating the crystal growth in a solid-state reactions method. For instance, in the synthesis of Zinc Sulfide, the presence of flux reduces the activation energy of crystal growth from ~89 to ~30 kcal/mol, so that they can melt at the calcination temperature and provide the liquid phase during the heat treatment. This liquid allows the ease of sliding and rotation of particles, which promotes the particle-to-particle contacts and leads to an enhancement in the particle growth. The aforementioned process description shows that the synthesis of YAG: Ce³⁺ through a solid-state reactions method is difficult and laborious because the materials require calcination at a very high temperature ~1500 °C and washing with a dilute acid to remove the residual flux reagent [1]. Furthermore, to achieve a phosphor size in nanoscales using a solid-state reactions method is not viable because the high temperature would have promoted large crystal growth. Therefore, it is imperative to employ a simple process to crystallize high quality garnet phosphors at low temperatures. In this study, nanophosphors are to be synthesized through a chemical route.

2.1.2 Synthesis of the nanophosphors (<200 nm)

This section specifically reviews the synthesis of garnet nanophosphors via the soft chemistry routes. The methods used so far are mainly based on the conventional chemical precipitation, reverse microemulsion, sol-gel, and thermal treatment method, targeting at reducing the nanophosphors sizes and crystallizing phosphors with a pure garnet phase at temperatures lower than that in the conventional solid-state reactions method.

Chemical precipitation

Chemical precipitation can be used to obtain pure yttrium aluminium garnet phase but only with a calcination temperature at 900 °C and above [36, 37]. This is because the intermediate phases such as perovskite and monoclinic are present when oxide powders are calcined below 1000 °C. This finding is clearly shown by the in-situ Raman monitoring of the synthesis of YAG using nitrates and hydroxides as the starting materials [38]. Alternatively, a phase evolution study using X-ray diffraction (XRD) and DTA/TG simultaneous thermal analysis also shows the same findings [39]. The chemical precipitated nanophosphors are usually irregular in morphology, larger than 20 nm in size, and they are highly agglomerated.

This chemical precipitation method can be better controlled when the chemical reactions are confined inside the aqueous-in-oil droplets (or emulsions). Emulsion is a mixture of oil and an aqueous phase and these mixed phases are

stabilized with the aid of surfactants. Reverse microemulsion is the system when aqueous droplets are in the nano-size range and are stabilized by the surfactants in the oil matrix. Vaqueiro *et al.* [40] investigated yttrium iron garnet nanophosphors using co-precipitation in a reverse microemulsion approach. The method produced carbonate precipitates ~ 3 nm in sizes. However, after calcination at 800 °C, the precipitates were no longer stabilized inside the droplets due to the loss of surfactants. They formed very large aggregates (~ 1 μm) composed of irregular garnet particles.

Sol-gel processing

Sol-gel processing is known to produce materials at low temperatures. For example, the alkoxide precursors are able to form yttrium iron garnet at temperatures above 675 °C [41]. Another example is the work by Veith *et al.* [42] which demonstrated that the alkoxide route can yield pure garnet phase at a low temperature of 700 °C. These examples show that sol-gel can provide a significant advantage because of the low temperature garnet formation and there are no other impurity phases such as perovskite and monoclinic co-existing with garnet. This finding is further confirmed by Iida *et al.* [38] who used in-situ Raman spectroscopy to investigate the transformation of YAG from the alkoxide precursor.

Solvothermal/ glycothermal

Another way to reduce the reaction temperature is to carry out the chemical reactions at some high pressure. This method is called the solvothermal in which the non-aqueous precursors are reacted inside an autoclave.

Li *et al.* [43] employed the solvothermal method to produce nano-sized YAG particles. The preparation involved mixing the carbonate precipitates with ethanol in the autoclave and heat treating the precursor at 290 °C with pressure increased to 10 MPa to form a garnet phase. Their TEM analysis showed that the YAG particles were spherical, monodispersed, and about 60 nm in size.

Another example of a solvothermal method is achieved by Kasuya *et al.* [44]. They synthesized cerium doped YAG nanophosphors with an average size in 20 nm. The precursors were stirred with a mixture of polyethylene glycol (PEG) and 1,4-butylene glycol, and the final mixtures were then heat treated at 300 °C for 2 hours with pressure increased to a maximum at 4.9 MPa in an autoclave. This process is also known as a glycothermal method because the glycol is used as the solvent for the reaction. The results of the FTIR analysis revealed that the oxygen atoms in PEG were coordinated to the metal ions in the nanophosphors. This coordination helps to passivate the oxygen vacancies at the surface of the nanophosphors, lead to an increase in quantum efficiency. Another notable feature of PEG is it has prevented the oxidation of cerium from trivalent to tetravalent state during and after the synthesis. Several reports using the similar process have been reported elsewhere [45-48].

There is another method called the polyol-mediated synthesis in which the glycol is used as a solvent but in a non-pressurized reaction. A detail review by Feldmann [49] shows the versatility of polyol process in synthesizing the well-dispersed nanophosphors. But this method can only produce phosphor with a size ~ 30 nm or greater due to the limited solubility of the precursors in diethylene glycol (DEG).

Combustion

Combustion is an effective method in synthesizing nanophosphors. Lu *et al.* [50, 51] has described the sol-gel polymer combustion [50, 52] for the synthesis of cerium doped yttrium aluminium garnet. The precursors were prepared by mixing the urea and metal nitrates with polyvinyl alcohol (PVA) to form an aqueous solution. The mixture was then calcined in a reduced atmosphere at 1000 °C for 4 hours and resulted in agglomerated particles with an average size of 35 nm. They found that the nanophosphors emitted low luminescence intensity for which they attributed the poor efficiency to the surface defective states. The origin of these surface states is due to the discontinuity in the lattice periodicity and is considered to be different from the bulk states. They further explained that the trap level is related to the oxygen vacancy whose energy level is between the ground and excited states of Ce^{3+} ion. Another type of sol-gel combustion is to use organic glycine as a fuel to synthesize garnet nanophosphors [53] which resulted in agglomerated phosphors with an average size of 40 nm.

Recently, Haranath *et al.* [54] have successfully synthesized cerium doped YAG using the combustion method with urea added as the fuel. The process was initiated by combusting a mixture of metal nitrates and water-ethanol solution in a quartz tube with the furnace pre-heated at ~ 600 °C. The dried mixture became foam during the vigorous reaction. The resulting particle size was ~ 40 nm and the quantum efficiency was about 54 %. The authors believed that further reduction in particle size to less than 5 nm could potentially enhance the photoluminescence efficiency.

2.1.3 A lack of YAG: Ce³⁺ with sizes of less than 10 nm

While the aforementioned soft-chemistry routes are able to crystallize garnet nanophosphors at a temperature lower than that in the solid-state reactions method, not much is known for synthesizing garnet nanophosphors with a size of less than 10 nm. The reported garnet phosphors sizes are still limited to the tenths of nanometers and they are agglomerated. Without being able to produce the phosphors with a size of less than 10 nm, the studies of the size-dependent optical properties are not possible. Therefore, in this study, the method of producing garnet nanophosphors with a size of less than 10 nm is investigated based on the nonhydrolytic approach which is discussed in the next section.

2.1.4 Synthesis of the nanophosphors with particle sizes < 10 nm

A detailed review of the nanophosphors or quantum dots was reported by Chander and Adair *et al.* [55, 56]. The reported phosphors with a size of less than

10 nm are mostly semiconductor and metallic materials. The synthesis requirements for metal and semiconductor quantum dots are different from the one required for insulating materials because both classes of materials have different crystallization energies. Nevertheless, these methods used for synthesizing the semiconductor and metal quantum dots could serve as references.

In general, the synthesis of quantum dots is very challenging because nanomaterials are thermodynamically unstable (when compared with bulk materials) [57]. The kinetic conditions must be carefully controlled so that the crystal growth can be inhibited. This means that the quantum dots have to be synthesized at a temperature that is sufficiently low and without any post-process heat treatment. The common chemical synthesis for producing quantum dots can generally be classified under hydrolytic and non-hydrolytic approaches.

Hydrolytic process

A common method of hydrolytic process is the reverse microemulsion. The droplet (aqueous core) in the oil matrix provides a confined environment where the chemical reactions can occur. For example, the semiconductor quantum dots CdSe, can form through ion-exchanges when Cd^{+} -containing-microemulsion is mixed with Se^{-} -containing-microemulsion and it is shown in Equation 2.1. This particular approach is called the two-microemulsion. The schematic diagram in Figure 2-2 shows that each aqueous droplet in oil is surrounded by surfactants. After the ion exchange, the CdSe quantum dot is formed inside every droplet.

However, for an insulating material such as the garnet, as described in Section 2.1.2, the formation of garnet phase requires calcination at 800 °C which causes ~3 nm micelles to aggregate and form ~1 µm particles [40]. Hence, the control of particle sizes of less than 10 nm through the reverse microemulsion technique is difficult.

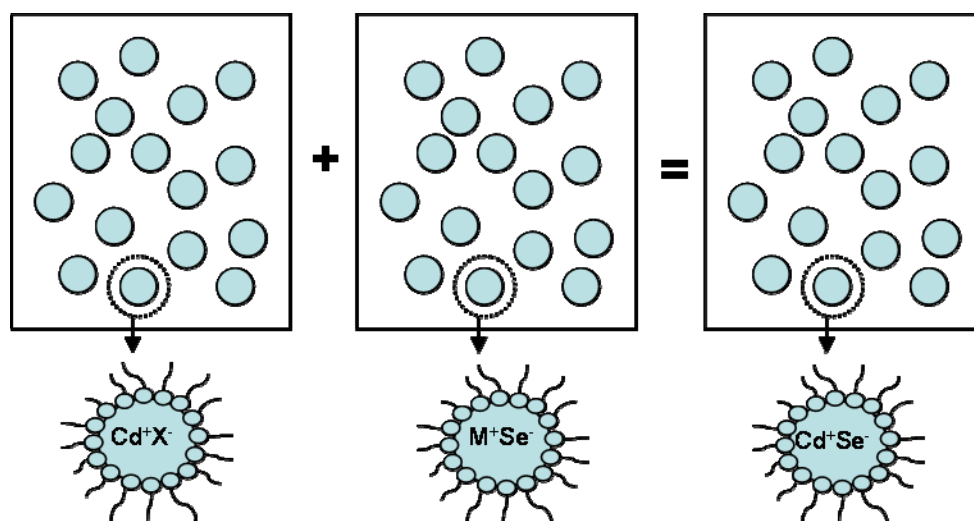
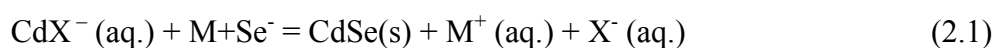


Figure 2-2: A two-microemulsion method in synthesizing CdSe nanocrystal

Non-hydrolytic process

One of the non-hydrolytic processes is solvothermal synthesis, a versatile method for preparing all classes of materials, namely metals, semiconductors, ceramics and polymers. The process involves utilizing a solvent to facilitate the chemical reaction of the precursors under a synergistic effect from both the

pressure and temperature. The conditions used in the process depend on the type of reactors. Typically, the pressure and temperature can range from 1 atm to 10,000 atm and 100 °C to 1000 °C, respectively. If the solvent used is an aqueous based (a case of hydrolytic process), the method is referred as hydrothermal and its process temperature is usually below the supercritical temperature of water at 374 °C. The morphology and size of the crystalline materials depend on the solvent's supersaturation, chemical concentration and kinetic control. In particular of quantum dots, it is essential that:

- i. The cation source in the precursor is soluble in the chosen solvent, and
- ii. A capping agent is available to stabilise the quantum dots by arresting the particle growth.

Some reagents can serve both as the solvent and capping agent, and some are only served as solvents that facilitate the chemical reactions. The review below will highlight some important reagents that have successfully been used to synthesize quantum dots.

Oleic acid and alkylamine (e.g. oleylamine) can serve as the capping agent in the synthesis of quantum dots. Their utilizations have been demonstrated in various high quality semiconductor and magnetic nanocrystals [4, 58-61]. (High quality means the particles are monodispersed and are highly crystalline).

Typically, the molecular precursors are thermally decomposed inside the templates formed by the oleic acid and/or alkylamine dispersed in the high boiling

solvent. An example is shown by Sun *et al.* [62] in the preparation of monodispersed magnetic nanocrystals. They prepared monodispersed Fe_3O_4 with a particle size less than 10 nm. These nanoparticles were obtained by reacting iron (III) acetylacetonate with alcohol in phenyl ether and were facilitated by the aid of oleic acid and oleylamine stabilizers at 265 °C. Due to the ease of process, a similar synthesis was scale-up by Park *et al.* [63]. They produced 40 g of magnetite nanocrystals (12 nm) in a single reaction without any further size-sorting process. They used the metal-oleate complex as the precursor and synthesized solvothermally using the mixture of oleic acid and 1-octadecene at 320 °C. The process is also versatile in producing a core-shell structure for a hybrid of semiconductor and metallic nanocrystals with the aid of oleic acid and oleylamine [64].

Non-magnetic quantum dots have also been successfully synthesized using oleic acid and/or alkylamine as the capping agents. For example, O'Brien *et al.* [65] synthesized 8 nm barium titanate nanocrystals by thermally decomposing the alkoxide precursors in the mixture of diphenyl ether and oleic acid at 140 °C. Upon cooling, 30 wt% of hydrogen peroxide was added to oxidize the nanocrystals. The particle size was highly uniform and they formed superlattices that extended over several microns due to the strong van der Waals forces. Rare-earths oxide nanocrystals, such as $\text{Y}_2\text{O}_3:\text{Eu}^{3+}$, were synthesized by Wang *et al.* [66] using carbonate-oleate complex solutions as the precursor. The precursor decomposed thermally in the oleylamine at 220-300 °C and formed nanocrystals. Other rare-earth phosphors such as rare-earth doped NaYF_4 nanocrystals or

nanorods (an up-conversion phosphors) had successfully been synthesized with the aid of oleic acid [22, 23, 67].

TOPO is another reagent that can provide nanocrystals with some degree of stabilization, but the size distribution varies and particles are irregular [68]. Fortunately, a combination of oleic acid/ alkylamine and TOP/ TOPO can improve the synthesis because they act as both a solvent and stabiliser. Synthesis of high quality CdSe nanocrystals with core-shell structures is possible when the mixture of hexadecylamine, TOPO, and TOP is used [69, 70]. Different morphologies such as CdSe tetrapods (with core in ~ 4 nm) are synthesized by controlling the acidity of the cadmium-oleic acid precursor and selenium-TOP precursor [71]. Monodispersity of the nanocrystals is still maintained at a size of 10 nm [72].

A coordinating organic solvent can have dual functions: It controls the crystallization route and stabilizes the nanocrystals from growing. An example of this type of solvent is benzyl alcohol [73, 74]. Niederberger and co-workers have demonstrated using benzyl alcohol as a versatile solvent in synthesizing various metal oxides nanoparticles at relatively low temperatures of 200-220 °C [75-78]. Another example is by Ba *et al.*, who has successfully synthesized indium tin oxide in benzyl alcohol [79].

Another form of stabilizer that can be used is the mercaptosuccinic acid. Chen and Kimura [80] have reported the preparation of gold nanoparticles by a solvothermal reduction route. In this method, the hydrogen tetrachloroaurate

tetrahydrate was reduced by sodium borohydride in the presence of the mercaptosuccinic acid.

In summary, in view of various synthesis methods, a hydrolytic approach is limited for synthesizing YAG nanophosphors (<10 nm). For instance, the reverse microemulsion can produce amorphous micelles but they require calcination which engenders crystal growth into larger size [40]. The high reactivity of water in sol-gel precursor leads to an uncontrollable crystallization [41]. Nevertheless, this approach can be used to synthesize nanophosphors of much larger sizes (>20 nm) so that it can be used for studying the size dependent optical properties. By contrast, the nonhydrolytic approach can yield high quality quantum dots which allows studies of their size-dependent optical phenomenon [70, 81-83]. Therefore, a non-hydrolytic process such as solvothermal is adopted in synthesizing garnet nanophosphors because it can reduce the reaction rates, which in turn leads to a better control in surface properties, particle sizes, morphology, and crystallization. In addition, in this study, oleic acid, alkylamine, and benzyl alcohol are chosen as the coordinating ligands due to their successful use in the synthesis of various semiconductor nanocrystals. The synthesized nanophosphors (<10 nm) are used for the size-dependent optical properties study.

2.2 Optical Properties of the Cerium doped YAG phosphors

Optical properties of cerium doped YAG phosphors are determined by the electronic structure of cerium ion in garnet, whose crystal structure is one of the most complex of all crystalline oxides [27] (the crystallography of garnet crystal

can be found in Appendix A). Thus, many spectroscopic studies of cerium-doped YAG are mainly focused on determining its energy levels. The next section, which serves as the fundamentals for the subsequent size-dependent optical studies, highlights the previous research findings and summarizes the electronic structure of YAG: Ce³⁺ bulk phosphors.

2.2.1 Electronic structure of YAG: Ce³⁺ in the bulk state

Ce³⁺ ion has the simplest electronic configuration ([Xe]4f¹) among the rare earth ions. Its electronic transition in YAG is a 4f-5d configuration type. The position of 4f state in this material was investigated by Pedrini *et al.* [84] through a photoconductivity experiment. They found that the photocurrent rise intensely at around 3.8 eV, which corresponds to the photoionisation threshold energy of Ce³⁺ from the ground state to lattice conduction band. Since the fundamental absorption edge of YAG measured by Slack *et al.* [85] is ~50,000 cm⁻¹ (~6.2 eV) (Figure 2-3), the 4f ground state is calculated as 2.4 eV above the valence band of YAG host material. This 4f orbital at the ground state is further split by spin-orbit interaction into a doublet (²F_{7/2} and ²F_{5/2} states) with a separation of ~2000 cm⁻¹ [31].

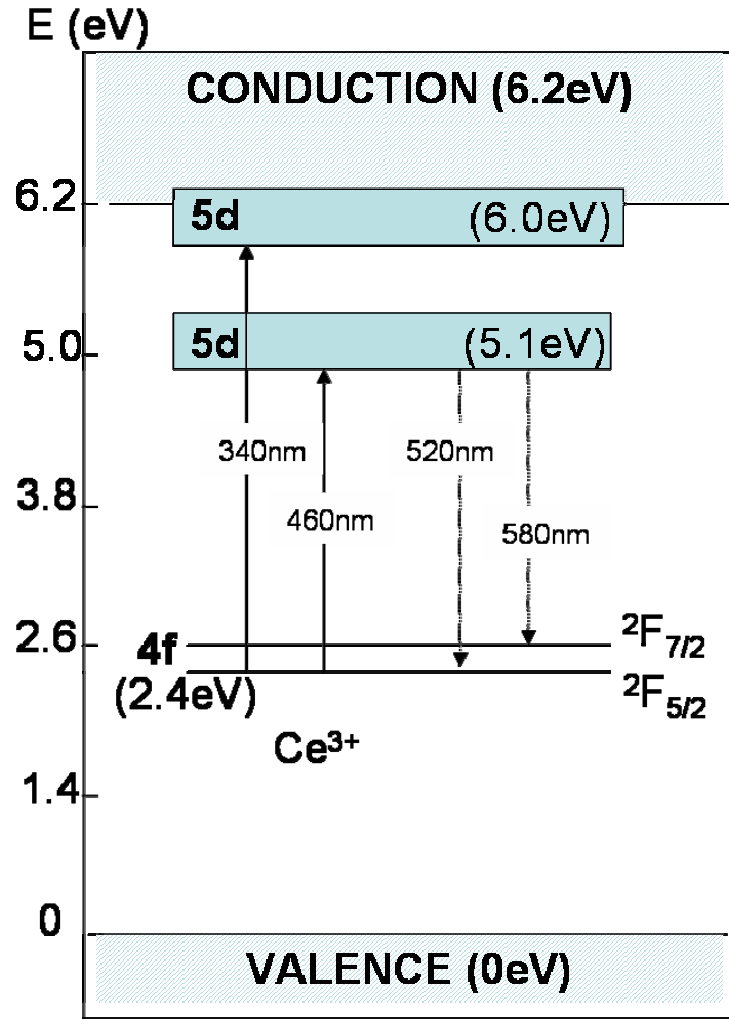


Figure 2-3: Energy level of Ce^{3+} in YAG

The position of 4f was further confirmed by Hamilton *et al.* [86] who used the excited state absorption (ESA) spectra to predict the photoionisation threshold as 30440 cm^{-1} , which is in good agreement with the previous ground state photoconductivity result of 30650 cm^{-1} (3.8 eV) [84]. Another notable feature found by Hamilton *et al.* [86] was that the lattice conduction band edge overlaps with the second 5d state, the optical pumping into this region could cause a direct excitation of the cerium ion whose electrons can populate the trapping sites through the conduction band.

In contrast to the well-shielded 4f states by the $5s^2$ and $5p^6$ filled shells, the 5d level is extremely host sensitive. It interacts strongly with the lattice, resulting in a strong electron-phonon coupling and large crystal field effects, which further split the 5d state into five different levels: A doublet (e_g) at lower cubic level (which is $(3/5)\Delta$ below the center), and a triplet (t_{2g}) at higher cubic level. This e_g level is further split by non-cubic components that pushes the lowest 5d state to an exceptionally low level at $22,000\text{ cm}^{-1}$ [87]. Hence, the two lowest 5d level are located at 5.1 eV and 6.0 eV (Figure 2-3).

Although the position of the 5d doublet is confirmed, the position of the triplet is controversial, because some reported that the bands present at 270 nm and 220 nm are the absorption bands associated with Ce^{3+} [31, 87-89], while others claimed that these absorption bands are found in undoped YAG and are presumed to be defects related [85, 90]. Fortunately, Tomiki and co-workers [91] were able to identify all the 5d-states (when previously only three lines were identified) and settle the dispute. Their results show that the positions are 2.7, 3.6, 4.7, 5.5, and 6.0 eV above the ground state $^2F_{5/2}$.

In summary, the excited optical transition of Ce^{3+} in YAG is a transition from 4f to the lowest 5d level. During the optical relaxation, the emission occurs from the lowest 5d component to the doublet of the ground state which gives the characteristic yellow emission observed in YAG: Ce^{3+} . The emission spectrum is broad and ranged from 470 nm to 700 nm. It was reported that the luminescence band composed of two overlapping bands centered at 520 nm and 580 nm (Figure 2-4) and each corresponds to the transition from the lowest 5d to the ground state

$^2F_{5/2}$ and $^2F_{7/2}$, respectively [91, 92]. The broad spectrum indicates a large Stokes shift between the 4f ground state and the phonon-broadened 5d excited state. The typical decay time is about 70 ns for YAG: Ce^{3+} because of the dipolar allowed transition [91]. Ce^{3+} in YAG shows parity and spin-allowed 4f-5d transitions in the visible part of the electromagnetic spectrum. Furthermore, its absorption and emission spectra show a mirror symmetry which indicates that the potential energy surfaces for ground (550 nm) and excited states (460 nm) are similar (Figure 2-4).

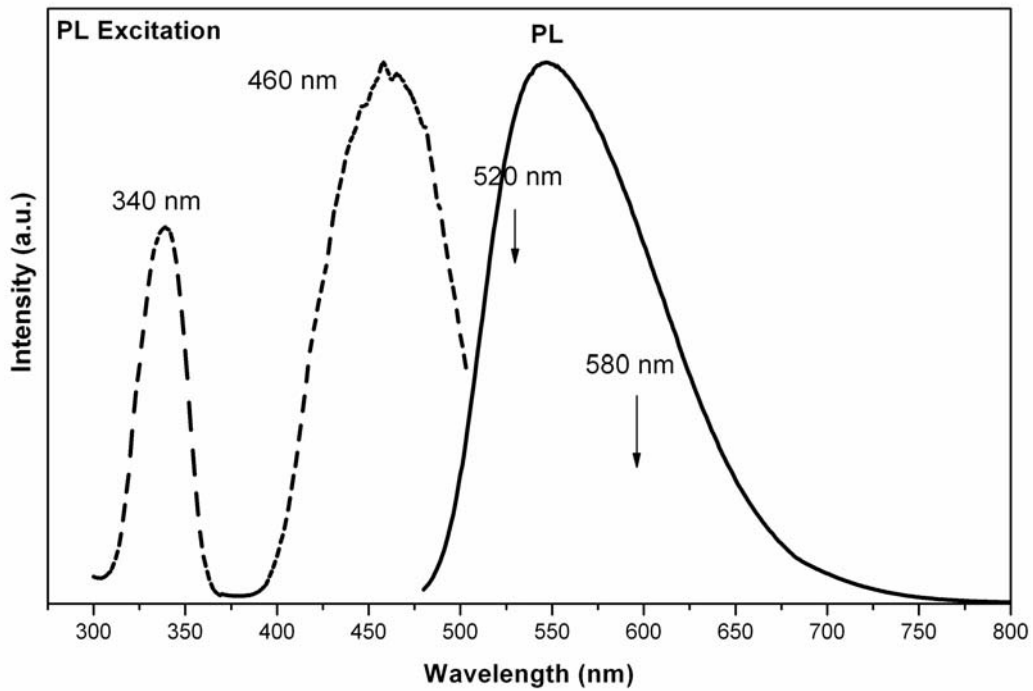


Figure 2-4: Luminescence spectra of YAG:Ce³⁺

2.2.2 A lack of the size-dependent optical studies for YAG: Ce³⁺

The electronic structure of cerium ion in YAG (as in the bulk state) has been reviewed in the last section. However, still not much is known on the optical properties of the same material in nanoscale. The main reason is the difficulty in synthesizing garnet nanophosphors.

There are a few studies on the YAG: Ce³⁺ nanophosphors (as described in Section 2.1), but they emphasized on aspects such as the synthesis chemistry or crystal phase transformation, and very few discussed the size effects on the optical properties. Furthermore, the investigations on productions for YAG: Ce³⁺ nanophosphors with sizes below 10 nm are sparse and thus the progress in size-dependent optical studies is impeded. Another aspect that is inadequately addressed for YAG: Ce³⁺ is the size-dependence of the electron-lattice relaxation process. In other words, not much is known on the influence of the YAG nanoenvironment on the electron-phonon interactions, an issue of both fundamental and technological importance.

2.2.3 Configurational Coordinate Diagram

Before discussing the factors such as the particle size that influences the optical properties of phosphors, it is useful to describe the photophysical processes through a configurational coordinate diagram [1]. This diagram is used to analyze the optical properties of rare earth ion or optical center doped phosphors.

The diagram in Figure 2-5 contains the potential energy curves that represent the total energy of an optical center at its ground state and the lowest excited electronic state in a host lattice. For simplicity, the diagram shown in Figure 2-5 represents an isolated optical center and neglects the effect of the distance ions. The ground state energies are separated into different energy levels and each of this level is called a Stark state. While the lowest ground state energy is the lowest occupying energy state, other ground state levels are occupied when the lattice is heated up above 0 K.

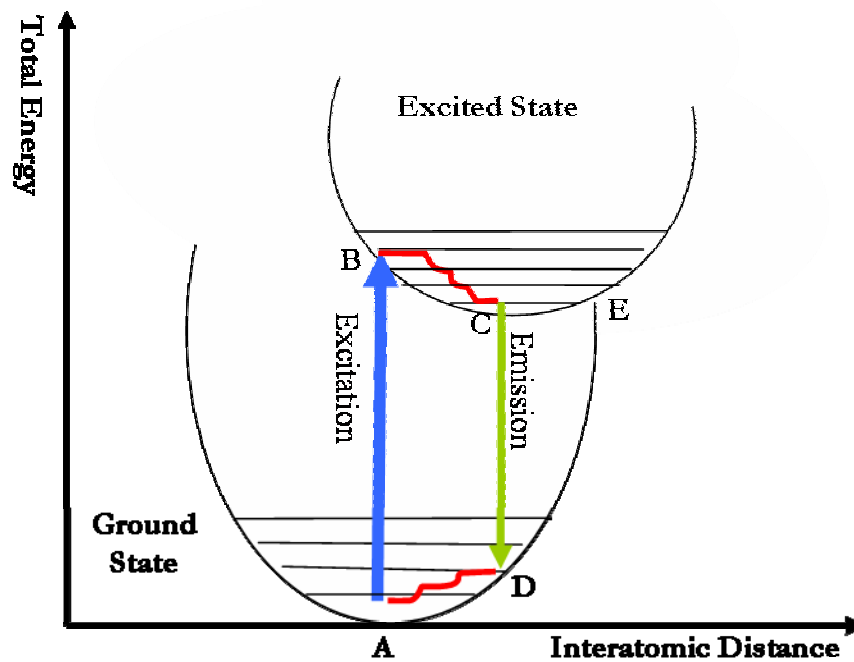


Figure 2-5: A configurational coordinate diagram [1]

Excitation process (absorption)

An optical centre absorbs a sufficient amount of energy from an irradiating source and becomes excited. According to the Franck-Condon principle [93], the

electronic transition can occur instantaneously from the equilibrium interatomic position A to B (Figure 2-5) while the nuclei being more massive than the electron is stationary during the transition (this is also known as the adiabatic approximation).

Emission process (photoluminescence)

After the optical center absorbs enough energy and transits from A to B (Figure 2-5), it goes through all the levels of Starks states and reaches the lowest excited energy state at position C, at which point the emission of photon starts to occur. The emission of photon causes the electronic transition to relax from position C to D, which is also known as the radiative decay. The transition is further relaxed by going through all the level of Starks states in the potential energy curves and finally, it reaches the thermodynamically equilibrium position A to complete the cycle. It is noted that when two configurational coordinate curves intersect each other at E), a nonradiative transition occurs by dissipating the excitation energy through the vibrational processes in the lattice. When the phonon vibration is dominating the overall electronic transition, the emission intensity reduces to zero.

Spectra line shapes

For a two energy level quantum system, one should expect an absorption (emission) spectrum to be a single line at a frequency $\nu_0 = (E_f - E_i) / h$, E_f and E_i are the excited and ground state energies, respectively. However, the observed

optical response is always consists of a band due to line-broadening mechanisms. By relating the line-shape function to the transition cross section, a spectrum line shape can be calculated as follows [94]:

$$\sigma(\nu) = S \times g(\nu) \quad (2.2)$$

where $\sigma(\nu)$ is the transition cross section, $S = \int_0^\infty \sigma(\nu) d\nu$ represents the transition strength for the radiation absorption (or emission), and $g(\nu)$ is the line-shape function with units of Hz^{-1} . The line-shape function determines the shape of the spectrum band and contains information about the optical center-system interactions. The minimum linewidth of an optical band is due to the life-time of the excited state, arising from the Heisenberg's uncertainty principle $\Delta\nu\Delta t \leq 1/2\pi$, where $\Delta\nu$ being the full frequency width at half maximum of the transition and Δt is the life-time of the excited state. This type of broadening is so-called the homogeneous broadening, assuming all optical centers are identical and contribute similar line-shape functions to the spectrum. The other type of homogeneous broadening is due to the dynamic distortions of the crystalline lattice coupled with harmonic oscillator vibration. Homogeneous broadening mechanism gives rise to a Lorentzian line shape with the line-shape function [95] as:

$$g(\nu) = \frac{\Delta\nu/2\pi}{(\nu - \nu_0)^2 + (\Delta\nu/2)^2} \quad (2.3)$$

In cases when different optical centers are present, the spectrum band shape is a convolution of the line shapes of various centers. Weighted by their respective

concentrations, the band broadened inhomogeneously, leading to a Gaussian line shape:

$$g(\nu) = \frac{2}{\Delta\nu} \left(\frac{\ln 2}{\pi} \right)^{1/2} e^{-\left(\frac{\nu - \nu_0}{\Delta\nu/2} \right)^2 \times \ln 2} \quad (2.4)$$

2.2.4 Factors to be considered in the size-dependent optical study

Based on the photophysical processes described through the aforementioned configurational coordinate diagram, the factors such as the Stokes shift, covalency, surface states, and electron-phonon interactions are important factors to be considered in the size-dependent optical study for YAG: Ce³⁺, because they cause an energy shift in the optical spectrum while reducing the particle size [96]. It is noted that other factors such as the site symmetry and selection rules are equally important, but they are more influential for study in the changes of optical responses of a given ion in different host materials, which is beyond the scope of this study.

The Stokes shift

When an optical centre absorbs a sufficient amount of energy, it becomes excited. According to the Franck-Cordon principle, the vertical electronic transition can occur instantaneously from the equilibrium interatomic position A at the ground state to position B in the excited state, while the nuclei being more massive than electron is stationary during the transition (Figure 2-5). Like the

ground state, Stark state can happen in the excited state but with different interatomic distance. For the activator in the excited state, the spatial distribution of its electron orbital spreads wider than that in the ground state, giving rise to a difference in the electron wave-function overlaps with neighbouring ions [1]. The expansion of the electron orbital further induces the readjustment of the interatomic equilibrium position and the bonding force of the molecules; this is the origin of the Stokes shift.

Cerium ion in cryptand ligand (Figure 2-6) is a good example to illustrate the effect of sizes on the Stokes shift [97]. Cryptands are a family of synthetic bi- and polycyclic multidentate ligands that can encapsulate a variety of cations [98]. The structures of these complex molecules are three dimensional analogues of crown ethers. One of the most common cryptand is [2.2.2] cryptand; its International Union of Pure and Applied Chemistry (IUPAC) name is 1,10-diaza-4,7,13,16,21,24-hexaoxabicyclo [8.8.8] hexacosane. The numbers inside the bracket [2.2.2] indicate the number of ether oxygen atoms that forms the binding sites in each of the three bridges between the capping amines.

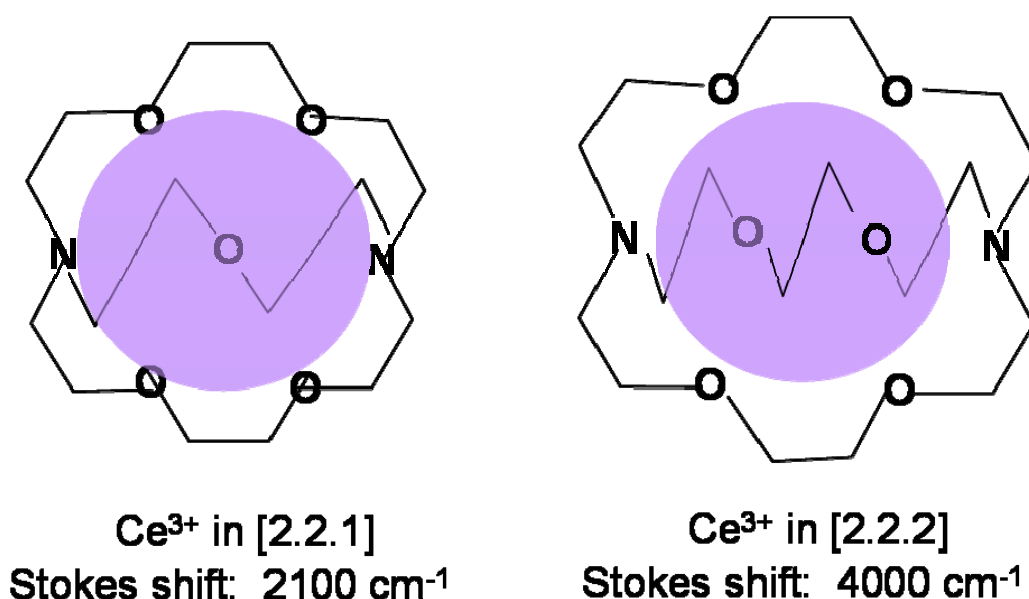


Figure 2-6: The structures and Stokes shifts of the [2.2.1] and [2.2.2] cryptand ligands encapsulating a cerium ion (purple)[2]

Figure 2-6 shows cerium ion being encapsulated in the cryptand ligands of two different cavity sizes. They emit differently due to different Stokes shifts. The 2.2.1 cryptand is smaller than 2.2.2 cryptand, and in fact, the 2.2.1 cryptand's cavity size is just large enough to encapsulate a single cerium ion. Hence, upon excitation, the 2.2.1 cryptand has less space for the cerium's expansion than that of the 2.2.2 cryptand, leading to the former emitting light with a smaller Stokes shift than that in the later.

The 2.2.1 cryptand acts as a stiff environment, suppresses the electron cloud expansion, and has constrained the amount of change in its equilibrium position. So the displacement of its configurational coordinate diagram (Figure 2-7) is little, resulting in small Stokes shifts. The emission band of the [Ce⊂2.2.1]³⁺ appears at higher energy, a blueshift in emission energy as compared to that observed in the [Ce⊂2.2.2]³⁺. A similar phenomenon can also be observed in

other materials: A blueshift in its photoluminescence emission when the size is reduced [99].

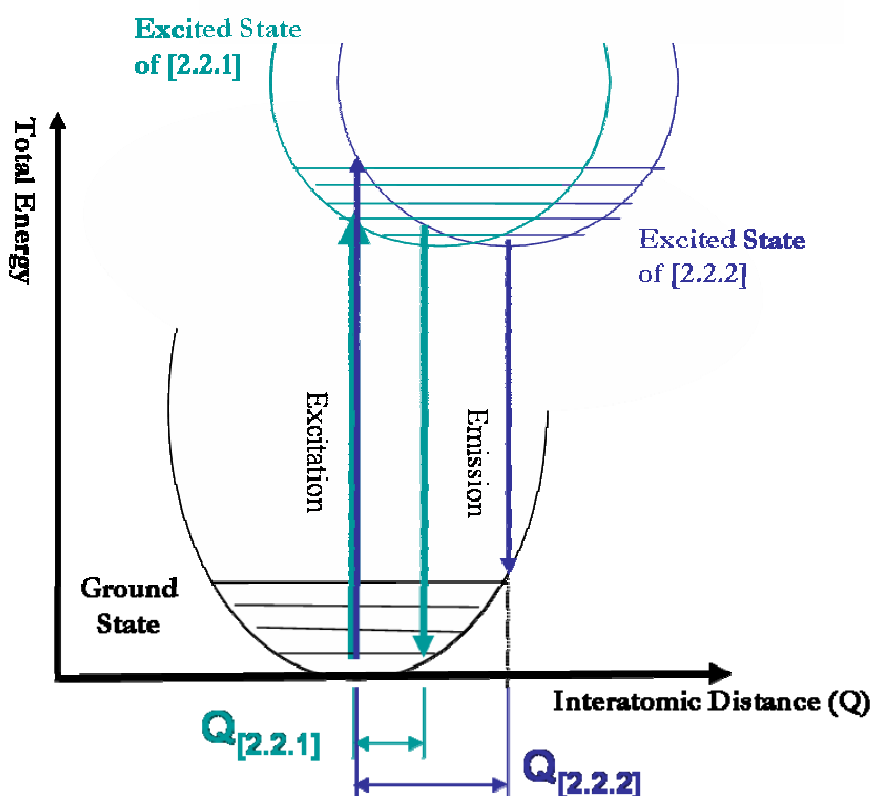


Figure 2-7: A comparison of the Stokes shifts of the $[\text{Ce} \subset 2.2.1]^{3+}$ and $[\text{Ce} \subset 2.2.2]^{3+}$ based on the displacement of the configurational coordinate diagram

Covalency

The covalency between the optical center and ligand is affected by electronic interactions between them and is closely related to changes in the phosphor size, which is usually revealed in the electronic transition energy shift. This phenomenon was reported by Igarashi and others whose works show that

reduction in the degree of covalency with decreasing particle size can cause a blueshift in the excitation peak [100].

It is also noted that covalency is related to the electron-phonon coupling strength (an important factor to be discussed later) as suggested by Jose and others. They showed that an increase in coupling strength with higher amounts of CdSe in the glass is an indication of high covalency [101]. Vink and Meijerink also suggested a similar result whereby a high degree of covalency in the chromium ion doped garnet material leads to a strong electron-phonon coupling [102].

Surface defective center

Surface defective centers are known to have detrimental effects on the optical responses of the nanophosphors because their presence are more significant than that in the bulk state and they act as trapping sites for the exciton [103-105]. Several mechanisms have been proposed to explain the effect of surface characteristics on the optical properties in nanomaterials [7, 106, 107].

While studies of surface effects have provided insight into the influence of surface characteristics on optical properties and the method in determining the residing location of the optical center, many research efforts have been devoted to enhance the fluorescence of nanocrystals through the removal of surface defects chemically [108, 109]. For example, surface can be passivated through a core-shell structure approach [69, 70, 81, 110].

Surface defects in the nanocrystal also may have a consequence on the electron-phonon coupling, a factor that is reviewed in the next section. Chen and others [111] suggested that the trapping of electrons or holes at the surface defects may impede the recombination of the exciton, which in turn may affect the phonon interaction strength.

Electron-phonon interactions

An interaction of a lattice of two-level molecules and a bath consisting of nuclear (intramolecular, intermolecular, and solvent) degrees of freedom can be described by a Frenkel-exciton model Hamiltonian, also known as the Holstein molecular crystal model [112]:

$$\hat{H} = \sum_n \Omega_n(q) B_n^\dagger B_n + \sum_{m,n}^{m \neq n} J_{mn}(q) B_m^\dagger B_n + \hat{H}^{\text{ph}} \quad (2.5)$$

Here $B_n^\dagger B_n$ represents exciton annihilation (creation) operators for the n^{th} molecules, q is the nuclear coordinates, and \hat{H}^{ph} is the bath (phonon) Hamiltonian. The excitonic operators fulfill the bosons relations $(B_n^\dagger)^2 = B_n^2 = 0$, $[B_m^\dagger, B_n] = \delta_{mn}$, with each site label n associating with a two-level system.

Electron-phonon interactions stem from the dependence of molecular frequencies Ω_n (diagonal coupling) and the intermolecular couplings J_{mn} (off-diagonal coupling) on nuclear coordinates q . The bath Hamiltonian in Equation 2.5 adopts the Einstein phonon Hamiltonian $\hat{H}^{\text{ph}} = \sum_n \hbar \omega_0 b_n^\dagger b_n$, where b_n^\dagger creates a

phonon of frequency ω_0 on site n , and thereby creating one Einstein oscillator per molecule, or a quantum harmonic oscillator per molecule.

Expanding $\Omega_n(q)$ of Equation 2.5 to the first order in phonon coordinate q , it reads $\sum_n \Omega_n(q) B_n^\dagger B_n = \sum_n \Omega_n(q=0) B_n^\dagger B_n + \hat{H}^{diag}$ with the diagonal coupling term as follows:

$$\hat{H}^{diag} = g\hbar\omega_0 \sum_n B_n^\dagger B_n (b_n^\dagger + b_n), \quad (2.6)$$

g is a dimensionless diagonal coupling constant. Expanding $J_{mn}(q)$ of Equation 2.5 to the first order in phonon coordinates q , it reads $\sum_{m \neq n} J_{mn}(q) B_m^\dagger B_n = \sum_{m \neq n} J_{mn}(q=0) B_m^\dagger B_n + \hat{H}^{od}$ with the transfer integral $J_{mn}(q=0) = -J\delta_{n,m \pm 1}$ and the off-diagonal term [113, 114] as follows:

$$\hat{H}^{od} = \frac{1}{2} \phi \hbar \omega_0 \sum_{nl} [B_n^\dagger B_{n+1} (b_l^\dagger + b_l) (\delta_{n+1,l} - \delta_{nl}) + B_n^\dagger B_{n-1} (b_l^\dagger + b_l) (\delta_{nl} - \delta_{n-1,l})]. \quad (2.7)$$

Equation 2.7 is assumed with a nearest-neighbour coupling of the antisymmetric type ϕ , a dimensionless parameter controlling the off-diagonal coupling strength, and the second term of Equation 2.7 is the Hermitian conjugate of the first.

\hat{H}^{ph} and the zeroth-order intermolecular term, together with Equation 2.6 and Equation 2.7, form the modified Holstein Hamiltonian (The original Holstein Hamiltonian contains only the diagonal coupling) [115]. There are two energy

scales, namely the lattice relaxation energy $g^2\omega_0$ and the bare exciton bandwidth $4J$, in the Holstein Hamiltonian whose ratio denotes the electron-phonon coupling strength $\kappa = g^2\omega_0 / 4J$. This coupling strength, also known as the Huang-Rhys factor, determines the size of the polaron and the electron-phonon interactions. For strong electron-phonon coupling ($\kappa \gg 1$), small polarons are resulted due to the exciton-induced lattice distortion, confining to essentially a single exciton site. By contrast, for a weak electron-phonon coupling ($\kappa \ll 1$), large polarons are resulted as the spatial extend of the lattice distortion is significantly increased.

In general, the host lattice is always experiencing vibrational waves due to the thermal motion of the atoms. While these waves are scattered by atoms and defects in the lattice, the energy and momentum of the waves can be carried by the phonons and are distributed throughout the lattice. The excited electron of the optical center dissipates its energy through the coupling with the vibrational waves of the lattice. Thus, the lattice size plays an important role in the optical properties of phosphors, especially when their host lattices are reduced to a nanoscale, which leads to the importance of studying the size-dependent electron-phonon coupling strength.

The size-dependent electron-phonon coupling strength in semiconductor nanocrystals was clarified by Takagahara through two coupling mechanisms [116]. He explained that when the crystal lattices experience a lattice displacement due to a thermal vibrational waves, their electronic energy structure changes in accord to a strain tensor and a proportionality constant, also known as the deformation potential coupling. In polar semiconductors, their lattice polarization is a result of

the lattice strain, which in turn interacts with an electron, an effect of piezoelectric coupling. The potential energy of the lattice polarization in the electric field induced by an electron gives rise to the electron-lattice interaction Hamiltonian. This deformation potential together with the piezoelectric coupling mechanism, render the electron-phonon interaction with acoustic phonon modes in semiconductor nanocrystals.

Effects of sizes on the electron-lattice coupling strength are shown by several research studies [99, 117]. They showed that the coupling strength decreases with reducing particle size. A similar result was obtained in quantum wells: Sun *et al.* [118] observed that the strength of exciton-phonon coupling was effectively reduced while decreasing the well width.

The electron-phonon coupling can be determined in a number of ways. For example, one method is to measure the line width increment and the spectral shift as a function of temperature [118, 119]. Alternatively, one can deduce the coupling strength from the ratio of the second to first order Raman scattering intensity using the resonant Raman scattering measurement [99].

While the coupling strength can be probed experimentally at low temperature, similar physical insight can be obtained through treating the observed Ce^{3+} optical response in YAG with the multimode Brownian oscillator model (BO), a theoretical framework that is commonly used to model optical responses during the excited-state relaxation in solutions and solids. In the BO model, a two-level electronic system is attached to a few primary oscillators, which in turn are

coupled linearly to a bath of secondary oscillators [120, 121]. Dissipation mechanisms, responsible for spectra broadenings, are thus introduced into this combined system of electronic and phononic degrees of freedom.

BO model has been successfully adopted in several studies. For example, Hu *et al.* [122] found that the calculated the excitonic coupling between adjacent transition dipole is in good agreement with the measured absorption spectrum of 20-base homogeneous adenine stacks. The same model has also been applied by Shi *et al.* [123] to determine the electron-phonon coupling strength and the coupling coefficient of the bath modes in ZnO. Similarly, Xu *et al.* [124] studied Si-doped InGaN quantum dots and used the BO model to characterise the coupling strength and the damping constant.

In this study, the influences of the YAG nanoenvironment on Ce^{3+} optical responses are studied through considering the factors such as the Stokes shift, covalency, and surface states. The size-dependent electron-phonon coupling is investigated through fitting the measured photoluminescence spectra within the framework of the Brownian oscillator (BO) model.

2.2.5 The Brownian oscillator (BO) model

The BO model is based on the work of Lax [125] and Kubo [126, 127] which have treated the spectrum line shape of linearly coupled electron-phonon systems through a second-order cumulant expansion. In this model, the dissipation mechanisms are introduced into the harmonic quantum oscillators by coupling the

primary oscillators linearly with secondary oscillators that are distributed continuously in a bath mode [120, 128-130].

The system is a two electronic-level system with primary nuclear coordinates coupled linearly to the electronic systems and the Hamiltonian is assumed as [120, 121]:

$$H = |g\rangle H_g \langle g| + |e\rangle H_e \langle e| + H' \quad (2.8)$$

where

$$H_g = \sum_j \left[\frac{p_j^2}{2m_j} + \frac{1}{2} m_j \omega_j^2 q_j^2 \right] \quad (2.9)$$

$$H_e = \hbar \omega_{eg}^0 + \sum_j \left[\frac{p_j^2}{2m_j} + \frac{1}{2} m_j \omega_j^2 (q_j + d_j)^2 \right] \quad (2.10)$$

and

$$H' = \sum_n \left[\frac{P_n^2}{2m_n} + \frac{1}{2} m_n \omega_n^2 \left(Q_n - \sum_j \frac{c_{nj} q_j}{m_n \omega_n^2} \right)^2 \right] \quad (2.11)$$

Here, the parameters p_j (P_n), q_j (Q_n), m_j (m_n), and ω_j (ω_n) represent the momentum, coordinate, mass, and the angular frequency of the j th (or n th) nuclear mode of the primary (or bath) oscillators, respectively. d_j is the phonon

displacement for the j th nuclear mode in the excited electronic state. $\hbar\omega_{eg}^0$ is the energy separation of the purely electronic levels. H' describes the bath oscillators and their coupling to the primary oscillators with a coupling strength c_{nj} .

The linear absorption and the photoluminescence spectra line shapes can be calculated from a spectral broadening function $g(t)$:

$$\sigma_{BO}(\omega) = \frac{1}{\pi} \text{Re} \int_0^\infty dt \exp \left[i(\omega - \omega_{eg}^0 - \lambda_j)t - g(t) \right] \quad (2.12)$$

$$I_{BO}(\omega) = \frac{1}{\pi} \text{Re} \int_0^\infty \exp \left[i(\omega - \omega_{eg}^0 + \lambda)t - g^*(t) \right] dt \quad (2.13)$$

where ω_{eg}^0 is the pure electronic transition frequency or is commonly known as the zero-phonon line, $\lambda = S\hbar\omega_{LO}$ is the Stokes shift, and $g^*(t)$ is the complex conjugate of the spectral broadening function $g(t)$. The details of the model can be found in Appendix B.

2.3 Summary

In conclusion, previous research works on the YAG: Ce^{3+} is limited to the tenths of nanometers, and little is known about synthesizing the garnet nanophosphors with a size of less than 10 nm. This has hindered the progress in understanding the influence of YAG nanoenvironment on Ce^{3+} electronic transition, especially in the absence of studies on the size-dependence of the electron-phonon coupling for YAG: Ce^{3+} . Therefore, in this study, highly

crystalline YAG:Ce³⁺ nanophosphors with particle sizes of less than 10 nm, 100 nm, and 300 nm are synthesized and size effects on the optical properties are examined. A theoretical model is employed to treat the observed Ce³⁺ optical responses in order to reveal the coupling strength of the electron-phonon interaction.

Chapter 3: Experimental Procedures

3.1 Introduction

To achieve the objectives of this study, the YAG: Ce³⁺ nanophosphors with sizes of less than 10 nm, 100 nm, and 300 nm were synthesized before their optical properties were characterized. The bulk phosphor was supplied by a phosphors manufacturer. The doping amount was 2 mole % of cerium in YAG (Y_{2.94}Ce_{0.06}Al₅O₁₂) as stated in the product specification sheet. This doping amount was clarified by the supplier [131] and further verified by the x-ray fluorescence (XRF) analysis (PANalytica PW2400 XRF System, The Netherlands). Since the nanophosphors were compared with the commercially-available YAG: Ce³⁺ bulk phosphors, their cerium doping levels were the same as that in the bulk materials.

The nanophosphors with a size of less than 100 nm were attempted using the chemical gelation method. The result showed that the nanophosphors with a 30 nm size were obtained after calcination at 900 °C. Another method based on the solvothermal reaction was sought to resolve the synthesis problem. Aided by the capping agents, the nanophosphors with a 5 nm size were produced. The solvothermal method was used to further grow the nanophosphors to a 250 nm size. After synthesizing all the targeted nanophosphors sizes, they were characterised according to their physical, chemical, and optical properties.

Modeling of the broad emission peaks of the bulk and nanophosphors was done using the multimode Brownian oscillator model.

3.2 Synthesis of the 30 nm nanophosphors via the chemical gelation

Materials: Yttrium oxide (Y_2O_3 , 99.9 %) and cerium (III) carbonate hydrate ($\text{Ce}_2(\text{CO}_3)_3 \cdot x\text{H}_2\text{O}$, 99.9 %) were supplied by Advanced Materials Resources (Europe) Ltd, UK, aluminum hydroxychloride solution ($\text{Al}_2(\text{OH})_5\text{Cl} \cdot 3\text{H}_2\text{O}$, 12 % metal basis) was purchased from Clariant Functional Chemicals, USA. The surfactant used was sorbitane monooleate (Span[®] 80) and was purchased from Sigma. Hydrochloric acid (HCl, 36 %) was purchased from Univar. The organic solvents (toluene, acetone, and ethanol) were all of analytical grade. Ammonia gas (99 %) was purchased from National Oxygen Ptd Ltd, Singapore. All reagents and chemicals were used as received.

Synthesis Procedures: Aqueous yttrium chloride solution ($\text{YCl}_3 \cdot x\text{H}_2\text{O}$) was prepared by dissolving the yttrium oxide (Y_2O_3) powders in an excess amount of hydrochloric acid (Equation 3.1).



Stoichiometric amounts of aluminum hydroxychloride ($\text{Al}_2(\text{OH})_5\text{Cl}$) and cerium carbonate ($\text{Ce}_2(\text{CO}_3)_3$) were added to the aqueous yttrium chloride solution to form a mixed chlorides solution. The as-prepared mixed chloride salt-solution

and 0.3 wt% sorbitane monooleate (Span[®] 80) were added slowly into the toluene to form water-in-oil (w/o) emulsion which was then stirred to homogeneity. Ammonia gas was introduced slowly into the emulsion to cause gelation of the particles. The precipitates were centrifuged and washed thoroughly with acetone, ethanol, and deionized water. The washed precipitates were then dried in an oven at 80 °C for 10 hours, and followed by heating the dried precipitates using a muffle furnace (HT10/18, Nabertherm, Germany) in air at a heating rate of 10 °C/min from ambient temperature to 800 °C, 900 °C, 1000 °C and 1300 °C for 2 hours and 1600 °C for 8 hours.

3.3 Synthesis of the 5 nm nanophosphors via the solvothermal method

Materials: Ammonium carbonates ((NH₄)₂CO₃), oleylamine (70 %, technical grade), and oleic acid (99%, reagent grade) were purchased from Aldrich. The organic solvents (toluene and methanol) were all of analytical grade. All reagents and chemicals were used without further purification.

Synthesis Procedures: Mixed yttrium, cerium, and aluminium carbonates were prepared by precipitating the mixed chloride solutions (the preparation of the mixed chloride solution was described in Section 3.2) using ammonium carbonates. The mixed metal carbonates precipitates (0.7 mmol) were then dissolved in oleic acid (10 g) in a sealed bottle with vigorous stirring to form a yellow transparent metal-oleate complex solution. One gram of the complex solution was extracted and mixed with oleylamine (4 g). This mixture was

transferred into a Teflon cup (45 mL), slid into steel autoclave, and carefully sealed. The autoclave was heated in an oven at 300 °C for 6 days. After cooling, methanol was added to cause the precipitation. The resultant precipitate was collected by centrifugation and redispersed in toluene to form a yellow transparent colloid.

3.4 Synthesis of the 250 nm nanophosphors via the solvothermal method

Materials: Yttrium(III) isopropoxide, Aluminum tri-*sec*-butoxide (99.99 %), cerium(III) nitrate hexahydrate (99.999 %), 2-propanol (anhydrous, 99.5 %), 2,4-pentanedione (99 %), benzyl alcohol (anhydrous, 99.8 %), trioctylphosphine oxide (TOPO, 99 %), and oleic acid (99%, reagent grade) were purchased from Aldrich. The chloroform (99.5 %) was purchased from Fluka. All reagents and chemicals were used as received.

Synthesis Procedures: The whole procedure was carried out in a glovebox to prevent any partial hydrolysis by atmospheric moisture. The precursor solution was prepared by dissolution of yttrium(III) isopropoxide (4.5 mmol), aluminium tri-*sec*-butoxide (7.6 mmol), and cerium(III) nitrate hexahydrate (0.09 mmol) in anhydrous 2-propanol (70 mL) with magnetic stirring. Next, the chelating agent 2,4-pentanedione (12 mmol) was added to cause the complexation of the precursor with vigorous stirring. The prepared precursor solution (2 mmol) was then mixed with anhydrous benzyl alcohol (14 mL) together with TOPO (13 mmol) and oleic acid (5 mmol) with stirring. The reaction mixture was stirred for

a few minutes and transferred to a Teflon cup (45 mL), slid into steel autoclave, and the flask was carefully sealed. The autoclave was taken out from the glovebox and heated in an oven at 250 °C for 9 days. After cooling, the resulted bright yellow precipitate was washed with chloroform and collected by centrifugation. Subsequently, the precipitate was dried in air at 60 °C overnight. The undoped YAG was prepared with the same method except the precursor solution contains no cerium ion content.

3.5 Characterisation of the chemical, physical and optical properties

Electron microscopy: Transmission electron microscopy (TEM) and high resolution TEM (HRTEM) images were collected digitally using a multiscan CCD camera connected to the JEOL microscope (JEOL-2010, Japan) operated at 200 kV and fitted with a low background Gatan double tilt holder. The point resolution and spherical aberration coefficient (C_s) of the TEM are 1.9 Å and 0.5 mm, respectively. Simulated images were calculated using the Multislice method [132]. Digital filtering and tests for local symmetry were processed using the fast Fourier filtering methods in the program *CRISP* [133, 134].

The TEM samples were prepared by depositing one or more drops of phosphors dispersions on 300-mesh copper-supported amorphous carbon films. It is noted that the multiple washings of the nanophosphors to remove the organic capping agents were an essential step for characterizing the garnet crystal structure

using HRTEM in phase contrast. However, an adverse effect was that the nanophosphors were aggregated as a result of the excessive washing.

Field emission scanning electron microscopy (FESEM) micrographs were obtained using JEOL (JSM-6340F, Japan) with a resolution of 3 nm. The FESEM samples were prepared by tapping the powders onto the carbon tape. The samples were sputtered with platinum for 60 seconds to prevent charging during the imaging.

In order to determine the mean phosphors particle sizes and the corresponding particle size distribution, 300 or more particles were measured from the micrographs for each sample and presented as a histogram. In case of non-spherical particles, a procedure of averaging the long and short axes of the particles was performed to determine the particle sizes.

X-ray diffraction (XRD): The crystal characteristics of the phosphor samples were investigated using powder x-ray diffraction in reflection mode on a Shimadzu diffractometer (LabX XRD-6000, Japan) fitted with Cu-tube (CuK α radiation) operated at 50 kV and 50 mA. Soller slits are present in the divergence and diffracted paths to limit the x-ray beam divergence and a monochromator in the secondary optics is used to reduce background. The scans were collected from samples rotating around the holder axis over the angles 10 ° to 145 ° with a 2 θ step size of 0.02 ° at a scan rate of 0.15 °/min. Divergence, anti-scatter, and receiving slits of 0.5 °, 0.5 °, and 0.3 mm, respectively were inserted.

The crystal structure of the garnets was refined by Rietveld analysis using a fundamental parameter approach in the program *TOPAS* [135, 136]. The starting model for refinement was based on the crystallographic data published for YAG [6]. The symmetry *Ia-3d* was used for all samples refinement calculations. For each set of data, a four-coefficient background polynomial, a zero error, and a sample displacement were refined sequentially. Then, the refinement was followed by unit-cell parameters, scale factor, and peak shape. Isotropic temperature factors were refined the same for all atomic positions. Special atomic positions were fixed, hence only the oxygen positions were refined. The quality of Rietveld refinement was evaluated according to the discrepancy factor and the goodness-of-fit indicator. The determination of the volume-weighted average crystallite sizes was achieved by the line-broadening analysis.

X-ray Photoelectron Spectroscopy (XPS): XPS measurements were performed on a PHI 5600 XPS system (Physical Electronics, USA) with a Mg $K\alpha_1$ x-ray radiation source (1253 eV) at a scan range of 0-1000 eV binding energy. The system is powered at 300 W/15 kV and is equipped with a multi-channel detector to investigate the chemical composition of the nanophosphors (in particular to the determination of the oxidation state of cerium). The nanophosphors powders were dusted onto a polymeric based adhesive tape on a sample holder. The vacuum level of the analysis chamber was at 8.0×10^{-9} torr. High resolution spectra for cerium were recorded in a selected range of 870 to 930 eV. Binding energies were calibrated by setting C 1s to 284.71 eV.

Binding energy of C 1s is normally calibrated at 285.00 or 284.80 eV. However, in order to accurately calibrate the binding energy, a measurement was performed on an empty sample holder. The binding energy obtained was 284.7 eV, with a difference of about 0.1 eV when compared to 284.8 eV, revealing that some hydrocarbon was adsorbed on the sample holder.

Peak deconvolution and fitting were performed with computer assisted surface analysis XPS (CASAXPS) software [137]. The Ce 3d_{3/2} and 3d_{5/2} lines were fitted using a Voigt function with 30% Lorentzian character and included a Shirley background. The components of the Ce peaks were constrained by setting the Ce 3d_{3/2}/Ce 3d_{5/2} ratio for the spin-orbit doublets to the theoretical ratio of 2:3 [138] and the full width half maximum (FWHM) ratio was assumed to be unity [137].

X-Ray Fluorescence (XRF): XRF measurements were performed on a PW2400 XRF System (PANalytica, The Netherlands) with an x-ray source at a power 3 kW and a multichannel analyser to determine the compositions of the commercial bulk phosphor.

Thermal behaviour: Simultaneous differential thermal analysis (DTA) / thermogravimetric analysis (TGA) were performed on a Netzsch (STA449C, Germany). The samples were investigated in air with a flowing rate of 10 °C/min and the temperature range was between room temperature to 1200 °C. TGA/ DTA were sought to determine the temperature of decomposition, phase transformation, as well as the weight loss of the dried precipitates.

Surface area: Surface area was measured using the Brunauer-Emmett-Teller (BET) method (N_2 chemisorption) on an automatic surface area analyzer (Quantachrome NOVA 2000, USA).

Photoluminescence (PL) and photoluminescence excitation (PLE): The optical properties of the samples were measured using a Fluorescence Photospectrometer (Varian Cary Eclipse, Australia) at room temperature. The sample was excited with a Xe pulse lamp, a single source with exceptionally long life, horizontal beam geometry. Following the lamp is a Czerny-Turner type of monochromator with a 0.125 m focal length. The emitted light was collected by a focusing lens and analysed through an emission monochromator before reaching the red-sensitive R928 photomultiplier tube detector. In emission spectra (PL), the excitation wavelength is fixed and the emitted light intensity is scanned in a certain wavelength range in between 200-900 nm. In excitation spectra (PLE), the emission monochromator is fixed at a desired emission wavelength while the excitation wavelength is measured by means of scanning in a certain wavelength range that is shorter than the fixed emission wavelength.

PLE, a useful technique to explore the optical properties of the nanophosphors, depends on the photon density of radiation, that is, the transition may not be observed in the PLE spectrum if the photon density is zero, even if the absorption transition between the two states occur [7]. So only the radiative transition could be observed in PLE.

The quantum efficiency was measured using the method described by Demas and Crosby [139]. The commercially-available bulk phosphors with efficiency of ~70% [54, 87] was used as the standard when the efficiency was acquired for the 30 nm and 250 nm nanophosphors. The organic dye (rhodamine 6G) with efficiency of ~95 % was used as the standard [140, 141] when the efficiency was acquired for the 5 nm nanophosphors (a transparent colloid). The dye was prepared with the same concentration as the nanophosphors.

Fourier Transform Infrared spectroscopy (FTIR): FTIR spectra were acquired on a Perkin Elmer Spectrum GX FT-IR spectrometer (USA) to characterise the bond stretching vibrational spectrum of the compositions in the nanophosphors. The transmission IR spectra were collected over the range of 400 to 4000 cm^{-1} .

Raman spectroscopy: Raman spectrum was measured in micro-Raman backscattering configuration (WITec alpha 300 Raman, Germany). The measurement was used as a reference for the determination of the optical phonon frequency of YAG: Ce^{3+} . The laser (wavelength 633 nm) was used as the excitation source so that the fluorescence spectrum did not interfere with the Raman signal. The laser light was focused onto the sample using a 100x objective lens and the backscattered Raman signal were recorded on a CCD camera. The spectrometer was operated in a confocal mode setting.

3.6 The multimode Brownian oscillator model

In this study, we adopted a simplified form of BO model to fit the measured photoluminescence spectra. Only one single primary oscillator, the optical LO phonon, was assumed with frequency $\omega_j = \omega_{LO}$. The dissipative bath was assumed to be Markovian with a coupling strength γ_j (i.e. its coupling strength γ with the bath mode is constant). The three control parameters for this model were the frequency of primary oscillator (ω_j), damping coefficient (γ_j) that characterize the coupling strength between the primary and bath oscillators, and Huang-Rhys factor (S_j) labeling the electron-LO-phonon coupling strength [142].

The photoluminescence (PL) spectra line shape for this simple case could be calculated from the spectral broadening function $g(t)$:

$$I_{PL}(\omega) = \frac{1}{\pi} \text{Re} \int_0^\infty \exp \left[i \left(\omega - \omega_{eg}^0 + \lambda \right) t - g^*(t) \right] dt \quad (3.2)$$

where $\lambda = S\hbar\omega_{LO}$, and $g^*(t)$ is the complex conjugate of the spectral broadening function $g(t)$,

$$g(t) = -\frac{1}{2\pi} \int_{-\infty}^{\infty} d\omega \frac{C''(\omega)}{\omega^2} \left[1 + \coth \left(\frac{\beta\hbar\omega}{2} \right) \right] \left[e^{-i\omega t} + i\omega t - 1 \right] \quad (3.3)$$

Here $\beta = 1/k_B T$ (k_B is the Boltzman constant), and $C''(\omega)$ is the spectral density function in frequency domain,

$$C''(\omega) = \frac{2\lambda_j \omega_j^2 \omega \gamma_j}{\omega^2 \gamma_j^2 + (\omega_j^2 - \omega^2)^2} \quad (3.4)$$

The green-yellow emission band of bulk YAG:Ce³⁺ and its nanophosphors at room temperature was modeled using Equation 3.2. The phonon frequency ω_j , damping coefficient γ_j , and the Huang Rhys factor S_j were determined from fitting the emission spectra within the framework of the BO model.

3.7 Summary

In this study, the nanophosphors with targeted sizes of less than 10 nm, 100 nm, and 300 nm were synthesized and characterised with respect to their physical, chemical, and optical properties. All results were gathered and analysed and compared to the bulk phosphor with the objective to elucidate the size-dependence of YAG: Ce³⁺ optical properties.

Chapter 4: Results & Discussion

YAG: Ce³⁺ nanophosphors with particle sizes targeted at less than 10 nm, 100 nm, and 300 nm were synthesized and their size-dependence of the optical properties were studied. The Brownian oscillator model was used to treat Ce³⁺ optical responses in YAG, revealing the size-dependence of the electron-phonon coupling.

This chapter reports and discusses the results first on the chemical gelation synthesis, a method based on the emulsion technique to produce nanophosphors with a size targeted at less than 100 nm. The crystallization process of this chemically gelated nanophosphor is discussed and linked to the thermal decomposition behavior, nature of the gel particles, and crystal growth with the preservation of the particle morphology. The complex crystal structure of YAG: Ce³⁺ is revealed by analyzing its atomic projection observed in high resolution transmission electron microscope (HRTEM).

The second part of this chapter reports on the solvothermal method to produce the nanophosphors with targeted sizes at less than 10 nm and 300 nm without the heat treatment process and then discusses the usage of various precursors and capping agents in facilitating the formation of nanophosphors with a controlled morphology. The significant role that Ce³⁺ plays in the formation of nanophosphor is discussed too.

Following the synthesis work, the third part of this chapter reports and discusses the size effects on the optical properties of the nanophosphors, relating to the Stokes shift, covalency, and surface defective center. The last part focuses on the size-dependence of the electron-phonon coupling to elucidate the coupling strength and phonon relaxation.

4.1 Synthesis of YAG: Ce³⁺ nanophosphors via a chemical gelation

Chemical syntheses such as homogeneous precipitation [143], co-precipitation [39, 144] and combustion synthesis [145], and physical methods such as spray pyrolysis [146] and solid-state reactions [147], are common methods used in synthesizing YAG particles. However, they have difficulties in crystallizing a pure garnet crystal phase at low temperatures (<1000 °C).

Several phases (perovskite YAlO₃ (YAP), hexagonal YAlO₃ (YAH) and monoclinic Y₄Al₂O₉ (YAM)) other than garnet are present after calcination, even when reacting a stoichiometric (Y:Al=3:5 for garnet) mixture of precursors. Therefore, it is necessary to control the precursors' compositions during the preparation. One of the methods is to use emulsions as reported by Hardy *et al.* [148]. They synthesized the undoped yttrium aluminium oxide by gelling the alkoxide sols in an organic solvent. However, the precursors (alkoxide sols) must be prepared at an elevated temperature.

The chemical gelation method described in this section is based on an emulsion technique but uses mixed salt-solutions as the precursors and no heat is required for the preparation. It was developed to synthesize the YAG: Ce³⁺ nanoparticles that crystallized with a pure garnet phase at a low temperature.

4.1.1 Crystallisation of YAG: Ce³⁺ nanophosphors

The crystallisation of chemical gelated YAG: Ce³⁺ particles has progressed via stages of dehydration characterised by thermoanalytical (TG) method. The TG and its derivative trace show 3 distinct stages of dehydration in Figure 4-1. The total amount of water loss was ~45 %. This observation shows that even though the precipitates had a dried-powder-like feel after washing with alcohol and being dried in air at 80 °C, the water was still present in the lattice in the form of OH⁻ and H₂O.

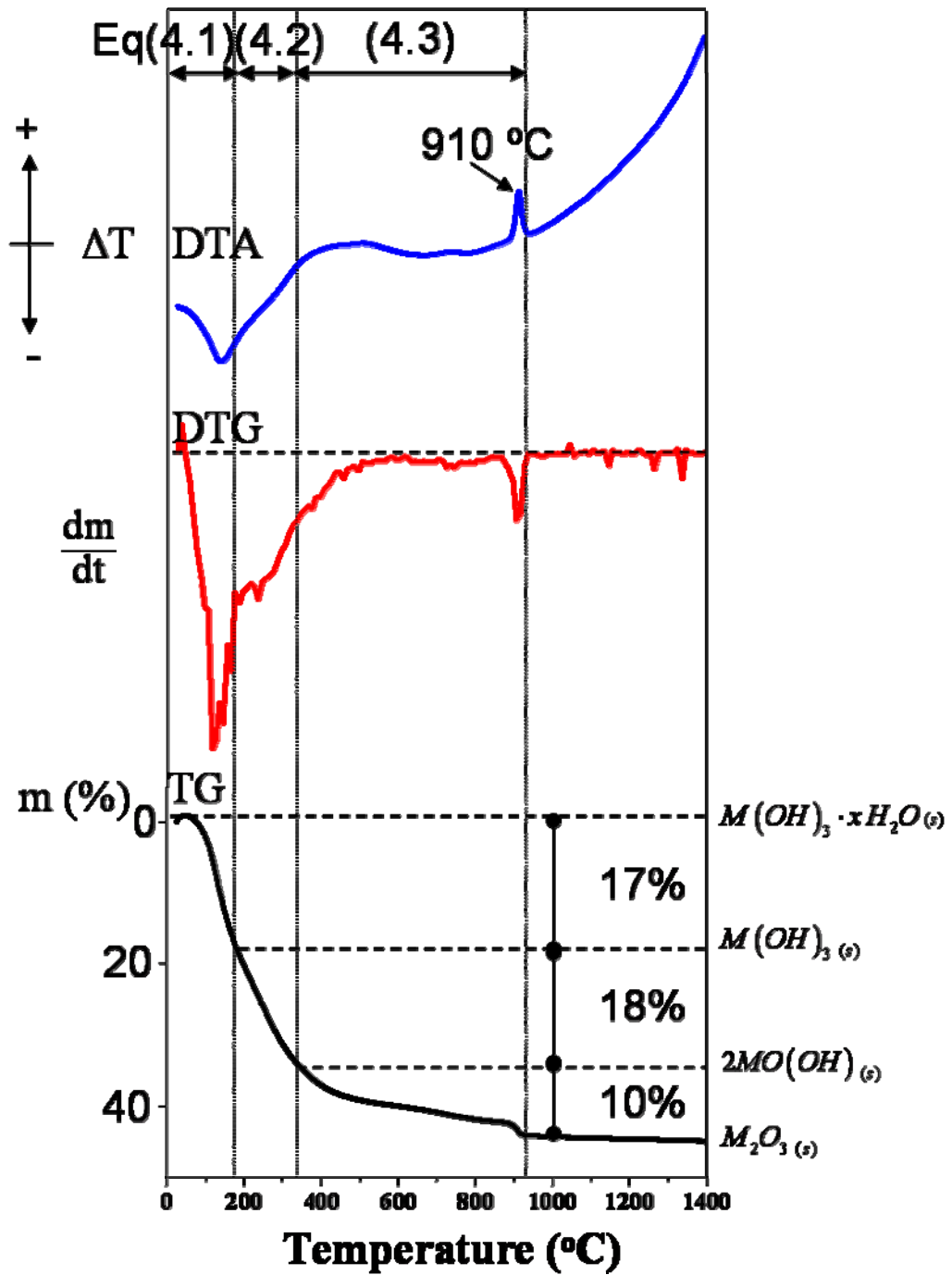
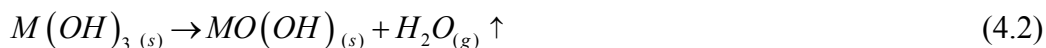


Figure 4-1: TG/DTA of the gel particles

The chemistry of the garnet's crystallisation closely resembles the formation of the hydrous aluminium oxide because garnet contains high amount of

aluminium oxide 62.5 wt%. Thus, the crystallisation of the garnet precipitates can be described using the following chemical equations (M is referred to metal ions):



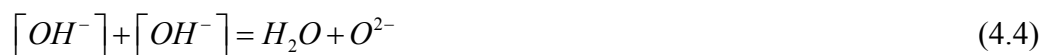
It was found that the theoretical weight losses for the chemical reactions in Equation 4.1~4.3 compared well with the observed weight losses in TGA (Table 4-1). The first and second stage of the dehydration was observed from room temperature to ~170 °C and 170 °C to 340 °C, respectively. These two stages can be distinguished from the derivative of the TG trace (DTG).

Table 4-1: Theoretical and observed weight loss

Equation	Temperature (°C)	Theoretical (%)	Observed (%)
(4.1)	<170	-	17
(4.2)	170-340	19	18
(4.3)	340-930	11	10
Total wt loss %	<1400	-	45

The first and second stages had a relatively sharp peak followed by a shoulder peak. The weight loss of the first stage was 17 % and this dehydration was rapid due to the evaporation of the adsorbed surface water and water of

crystallisation in the precipitates (Equation 4.1). The rapid weight loss continued to the second stage where the dehydration was occurred via OH^- condensation as shown in Equation 4.4:



The metal cations (M^{3+}) in the precipitates of the garnets were coordinated with OH^- in the form of $M(\text{OH})_6^{3+}$, which was connected linearly with a molecular spiral chain form [149]. The molecular water was trapped inside this tubular structure and hence, required higher temperature to promote proton migration H^+ to the neighbouring OH^- site for the OH^- condensation and transform into oxyhydroxide precipitates. Both the first and second stages of dehydration were indicated by DTA as a strong and broad endothermic peak at 120 °C.

The weight loss gradually continued into the third stage where OH^- condensation was more difficult to occur because they were separated by the oxo-bridges in the oxyhydroxide structure. Hence, a higher temperature was required for proton H^+ to gain more kinetic energy so as to break the bond and migrate to the polar site of the OH^- and caused the condensation.

As the temperature increased to 800 °C, the atomic diffusion occurred more rapidly, which in turn promoted the process of crystallization. As a result, some crystallinity was evident in the x-ray diffraction pattern (Figure 4-2) with some weak and broad intensity around Bragg diffraction (420). The rate of

crystallisation of garnet occurred most rapidly at 910 °C (onset-end: 897-930 °C), upon which the atomic diffusion and rearrangement were so fast that a significant amount of heat was released and that was accompanied by a weight loss of 1.7 %. This is most evident in the DTA curve as a single, strong and sharp exothermic peak (Figure 4-1). The weight loss after 930 °C was negligible.

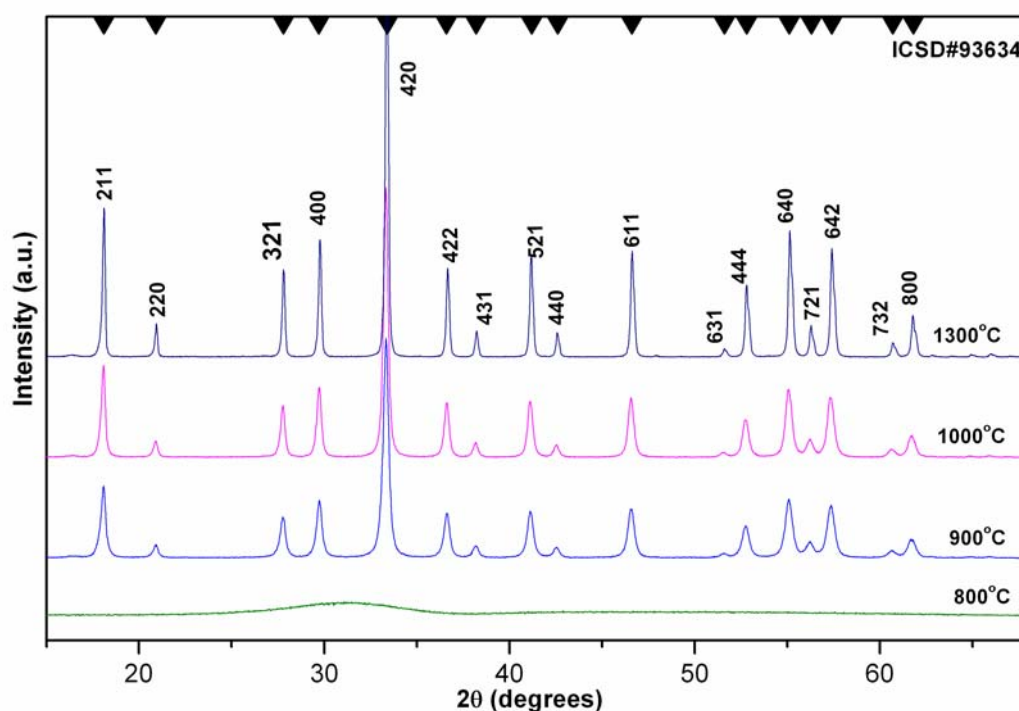


Figure 4-2: XRD pattern of Ce^{3+} doped YAG

While the crystallization temperature indicated in DTA is 910 °C, XRD pattern shows that the transformation temperature was 900 °C. This is because the sample was heat treated for prolonged hours before the XRD measurement, and this is in contrast to the measurement in the thermoanalytical method, which the heat exchange at every temperature increment was instantaneous and no dwelling time was allowed for further atomic diffusion and crystallisation. In Figure 4-2, all

Bragg diffraction peaks are indexed with the assumed garnet structure (*Ia-3d*) and no other phases are identified.

The single exothermic peak at 900 °C is novel for the garnet crystal produced via the chemical gelation method. The containment of the precursor solutions inside the emulsion droplets has enabled homogeneous mixing of the precursor with a stoichiometric amount. In addition, the controlled dissolution of ammonia gas into the water-in-oil emulsion has caused the emulsion droplets to gel homogeneously with no segregation. Thus, the chemical gelation process has prevented a sequential precipitation, an effect of different solubilities of Y^{3+} (pH 6 to 7) and Al^{3+} (pH 4 to 5).

If the sequential precipitation is allowed, aluminium ions would be segregated from the bulk, a deviation in the stoichiometric compositions is resulted. Therefore, the uniqueness of the chemical gelation method is that it produces only the pure garnet crystal phase and none to other phases, such as hexagonal $YAlO_3$ (Y:Al=1:1), orthorhombic $YAlO_3$ (perovskite, Y:Al=1:1) and monoclinic $Y_4Al_2O_9$ (Y:Al=4:2).

The chemical gelation method compares well against other chemical preparation methods, such as coprecipitation and alkoxide routes demonstrated by Sim *et al.* [150] which did not yield the desired garnet powders at 900 °C. They observed two exothermic peaks from samples derived by both the co-precipitation and alkoxide methods. The first peak was strong and sharp and the second peak was weak and broad. This observation has also been reported by other research

groups [151-153] who have failed to produce a pure garnet phase. Even if the heat treatment temperature was increased above 1000 °C, the amount of YAG phase could only increase to a limited extent. This is due to the same reason as mentioned earlier: The different solubilities of yttrium and aluminium ions in the precipitates cause the deviation in the bulk compositions.

In general, the co-precipitation exhibited mixed phases of YAG and YAH [39, 144], the combustion synthesis yielded YAH and YAG at 920 °C [145], the high energy ball milling process did not show any significant crystallization at 900 °C [147]. The sol gel-derived particles achieved crystallization of YAG at 900 °C [154], but its particle morphology was not as spherical as the chemical gelation-derived particles. In addition, the sol-gel particles were highly agglomerated.

4.1.2 Characterization of the YAG: Ce³⁺ spherical particles

Upon the addition of ammonia gas into the emulsion system, ammonia gas molecules dissolved and reacted with the water inside the droplets, and formed the aqueous ammonia solution as described in the following equation [155].



As the ammonia molecules dissolved readily in the water and the subsequent chemical reactions were confined by the emulsion droplets, thus the concentration of aqueous ammonia solution inside the droplets was high. This produced a high pH environment, and the precipitation and gelation were allowed

to occur homogeneously inside the droplets, flocculated the precipitate nuclei into three-dimensional networks.

Precipitate nuclei in the chemical gelated particles were gelatinous, porous and amorphous due to their three-dimensional flocculation networks. As the calcination temperature increased, the precipitate nuclei grew with improved crystallinity, as evident in the XRD Bragg diffraction intensity and the line broadening of the peaks (Figure 4-2).

The average nanoparticle sizes of the samples calcined at 900 °C, 1000 °C and 1300 °C were calculated by Rietveld refinement method [136] to be 27nm, 45nm and 114nm, respectively (Figure 4-3). These were consistent with the observations in the micrographs (Figure 4-4 to 4-6) that showed the flocks of nanoparticles aggregated to form large spherical particles with a wide particle size distribution. Those nanoparticles were more visible when the spherical particles were magnified under the microscope as shown in Figure 4-4(b), 4-5(b), and 4-6(b). The crystal growth of nanoparticles would be discussed in the next section.

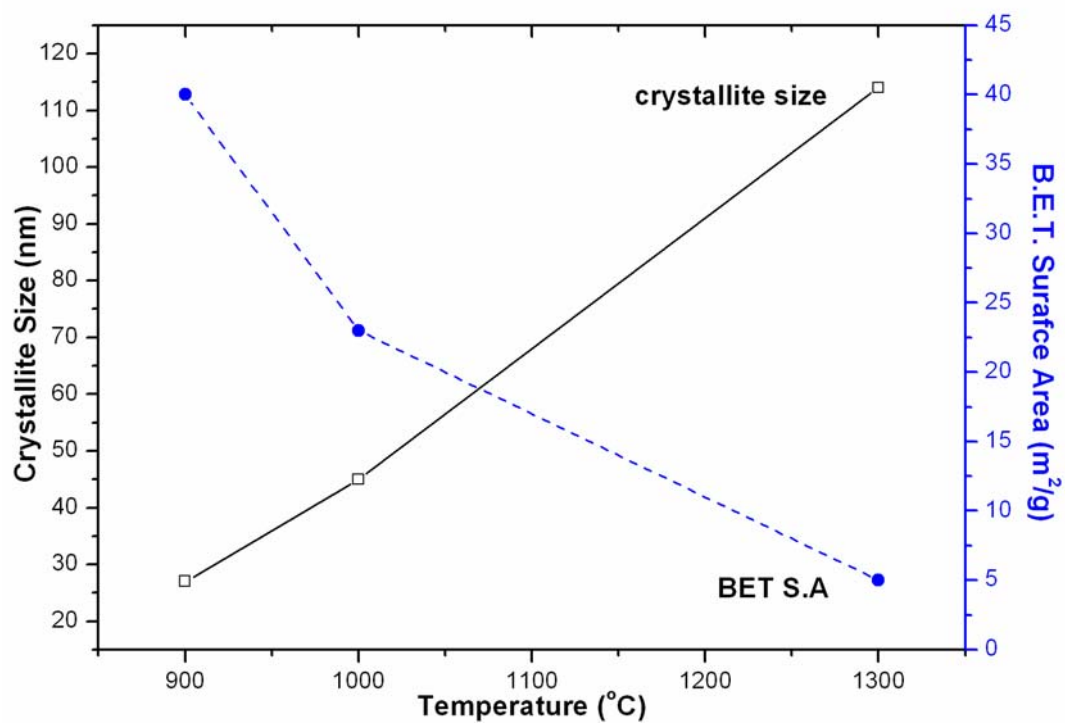


Figure 4-3: Crystallite sizes and surface areas as a function of temperatures

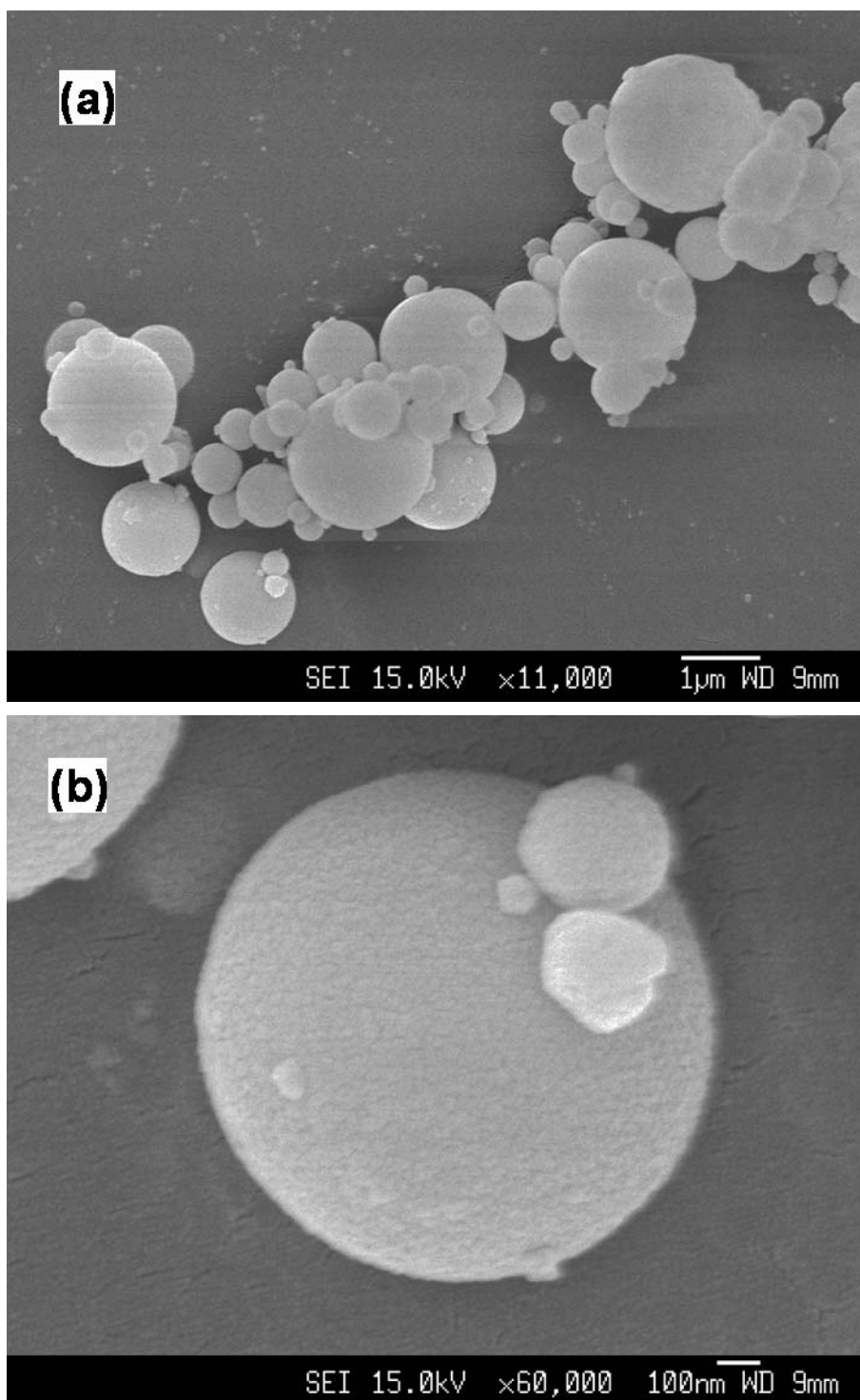


Figure 4-4: FESEM micrographs of YAG: Ce³⁺ calcined at 900°C

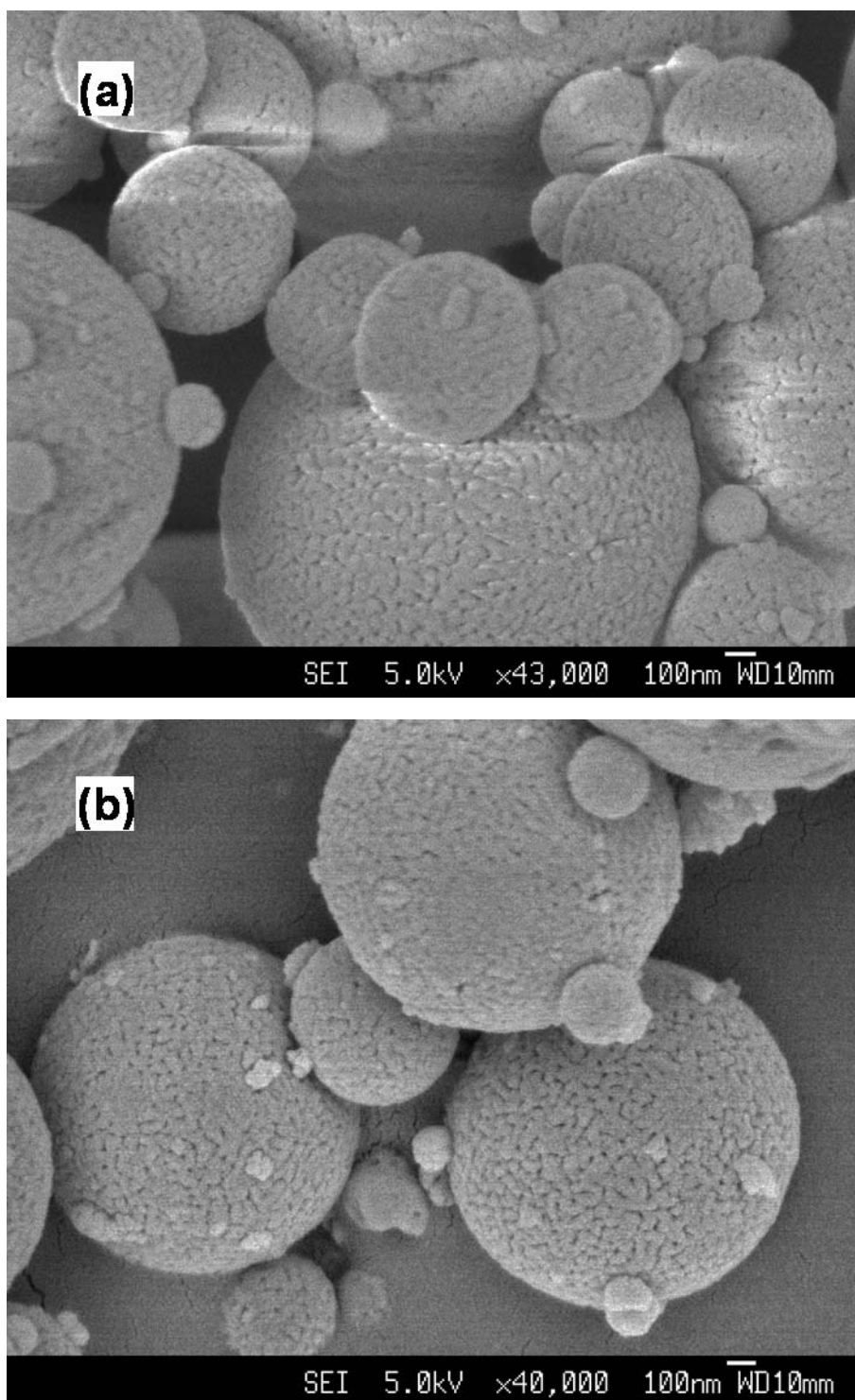


Figure 4-5: FESEM micrographs of YAG: Ce³⁺ calcined at 1000°C

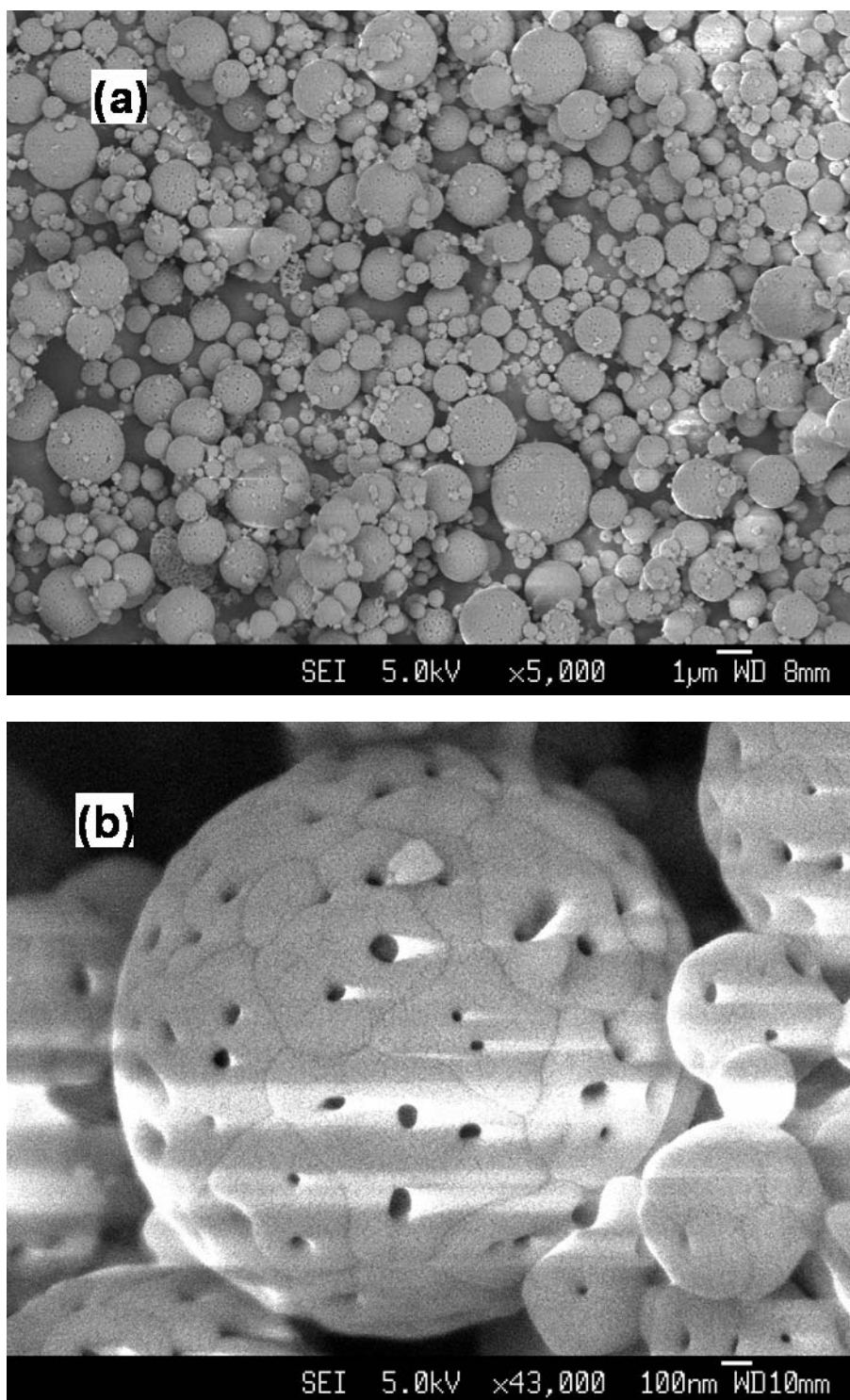


Figure 4-6: FESEM micrographs of YAG: Ce³⁺ calcined at 1300°C

Sample that calcined at 900 °C was chosen as one of the nanophosphors samples in the size-dependent optical properties studies. Its size distributions were measured from the TEM micrographs and were in agreement with the calculated

particle sizes (Figure 4-7). The reason that causes the flocculation of nanophosphors into large spherical particles is the nature of the surfactant used in the process. The chemical gelation method formed water-in-oil (w/o) emulsion droplets and encapsulated the electrolytes inside the droplets. Sorbitan Monooleate (a sorbitan ester derivative surfactant) used in this study is excellent for emulsification but poor for stabilisation [156]. As the emulsion droplets were thermodynamically unstable and the surfactant could not inhibit the coagulation, large particles were ripen during the emulsification process and resulted with wide particle size distributions [157] (Figure 4-8).

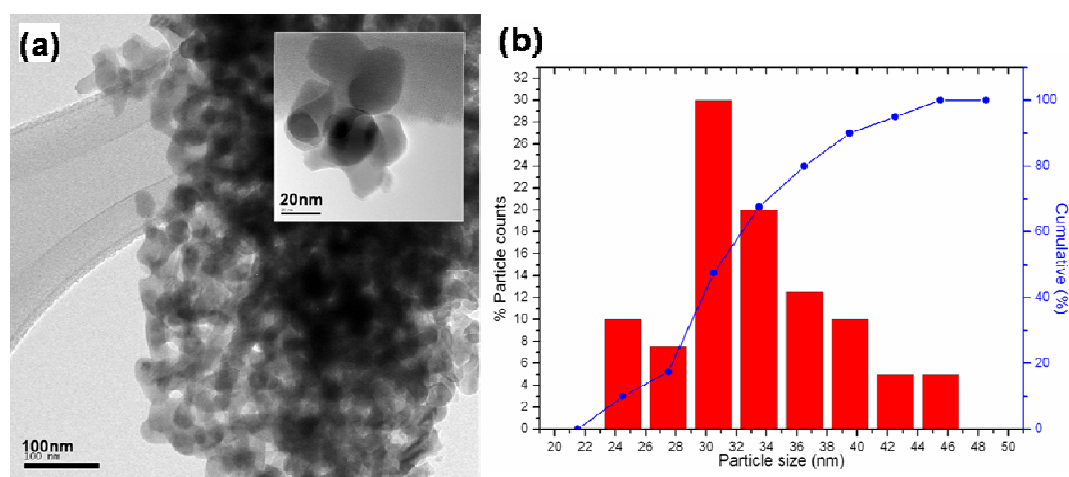


Figure 4-7: (a) TEM image of the nanophosphors and TEM image at higher magnification (insert) (b) Particle size distributions of the nanophosphors

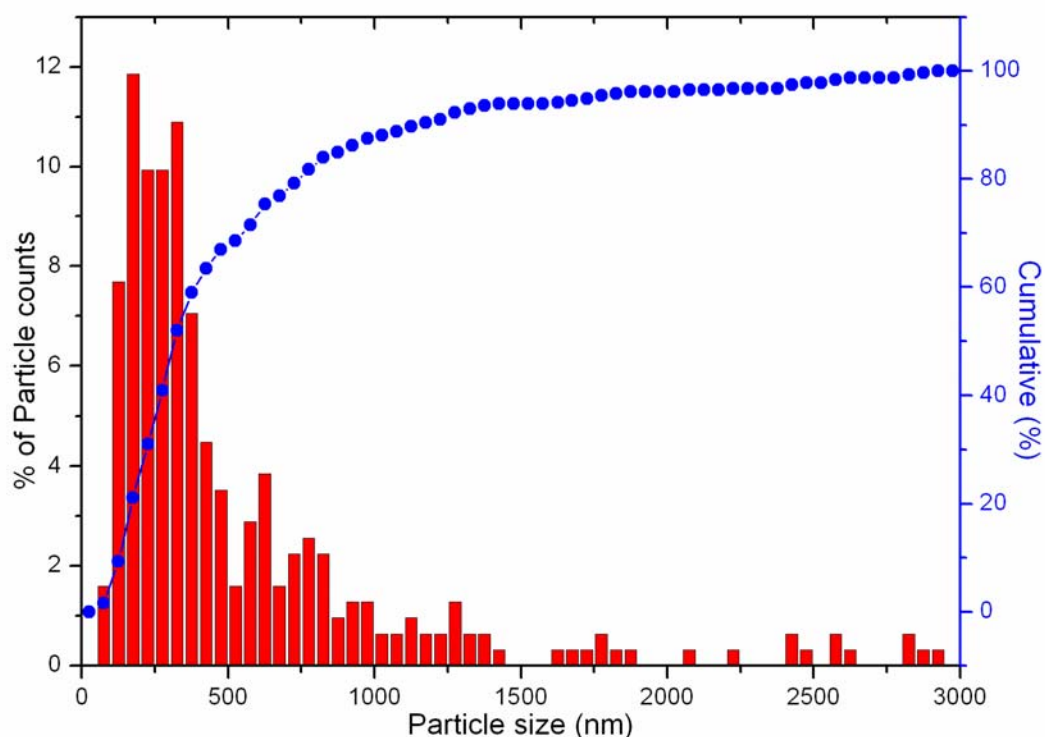


Figure 4-8: Particle size distributions of the chemical gelated YAG: Ce³⁺

4.1.3 Polycrystalline to single crystal

The chemical gelation method allows the formation of both polycrystalline and single crystal phosphors in spherical morphology, depending on the calcination temperature.

The gel particles are constructed by flocks of nanophosphors in three-dimensional networks. In unconnected regions, air voids or pores fill in the structure. As temperature increased to 900 °C, the precipitates were coalescenced into coarse crystallites while the pores were enlarged and fill in between the inter-

crystallite boundary [3]. These porosities are not apparent in the FESEM micrographs but in TEM micrographs due to the amplitude difference.

The nanoparticles, after heat treated at 1000 °C, continued to grow and coalescence into coarser crystallites due to the reduction of their total surface energies. During the growth, the pores at the boundary were either left behind by the moving boundary or migrated with the boundary [3]. Gradually, they agglomerated into bigger pores and were apparent in Figure 4-5b.

At 1300 °C, the particles were in the beginning stage of sintering. Each small crystallite was not distinguishable, big grains were formed instead due to the high boundary curvatures and high driving forces for the boundary migrations. Coarse crystallites had coalesced and grew into big grains. The clusters of small spherical pores with a size of less than 70 nm were left behind in the centre of the big grains (Figure 4-6b) as illustrated in Figure 4-9.

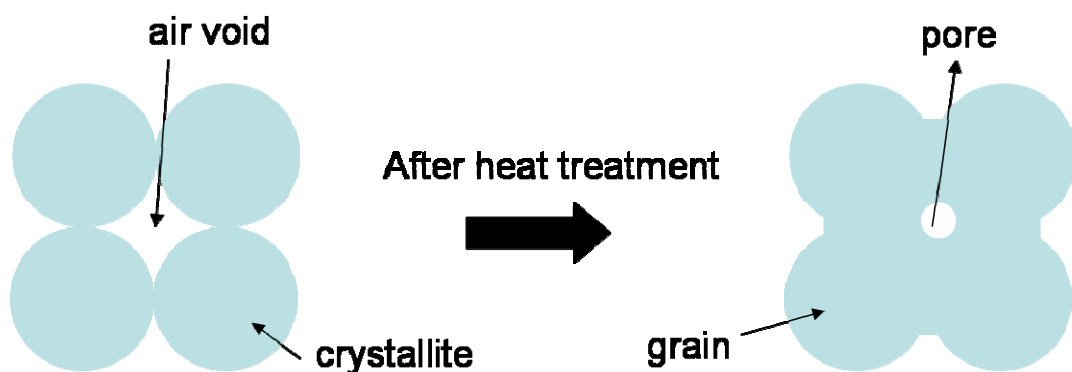


Figure 4-9: Formation of a pore within a grain [3]

For particles that are greater than 200 nm in sizes, those pores that left behind in the centre of the grains are apparent on the surfaces of the particles, as shown by the FESEM micrographs. However, for particles smaller than 200 nm, the pores could not be observed on the surfaces. TEM micrograph shows the pores had agglomerated and grew into larger pores inside the particles (Figure 4-10a). This phenomenon is due to the large ratio of pore to grain size, which in turn increased the stability of the pores for being inside the particles [3].

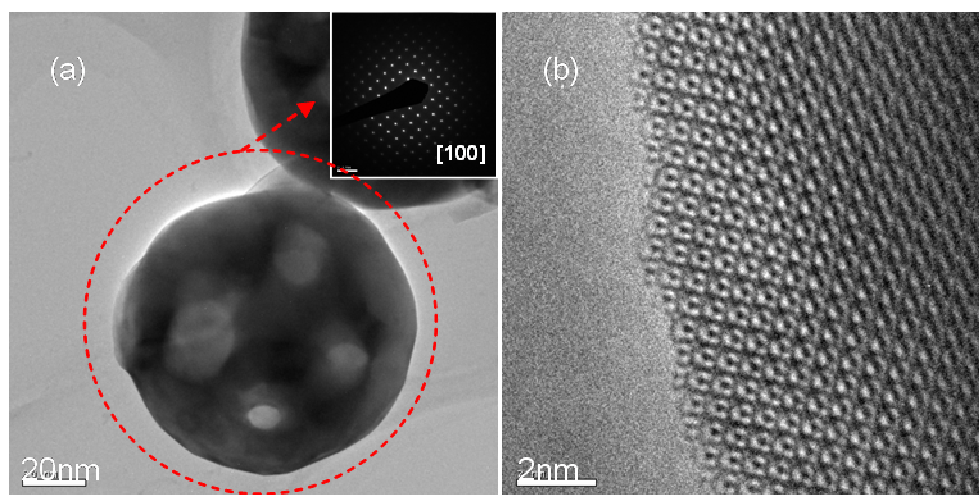


Figure 4-10: (a) TEM of a single crystal nanoparticle; insert is the SAED of the selected particle $\langle 100 \rangle$ (indicated by the red circle) (b) HRTEM micrograph of the particle

It is interesting to note that the particles had not collapsed from their spherical morphology, even at a temperature as high as 1300 °C. This characteristic is due to the presence of pores, acted as the fill-in structures so that the spherical morphology could be rigidly maintained.

If the pores were eliminated, the particles would condense into some faceted particles, as demonstrated for sample heat treated at 1600 °C for 8 hours

(Figure 4-11). These faceted particles are similar to the commercially-available YAG: Ce³⁺ phosphors (Figure 4-12) which are dense and hard. These crystal growth behaviors are manifested in the Brunauer-Emmett-Teller (BET) surface area results (Figure 4-3) which show that the crystallites had grown to larger sizes with reducing surface areas at high temperatures.

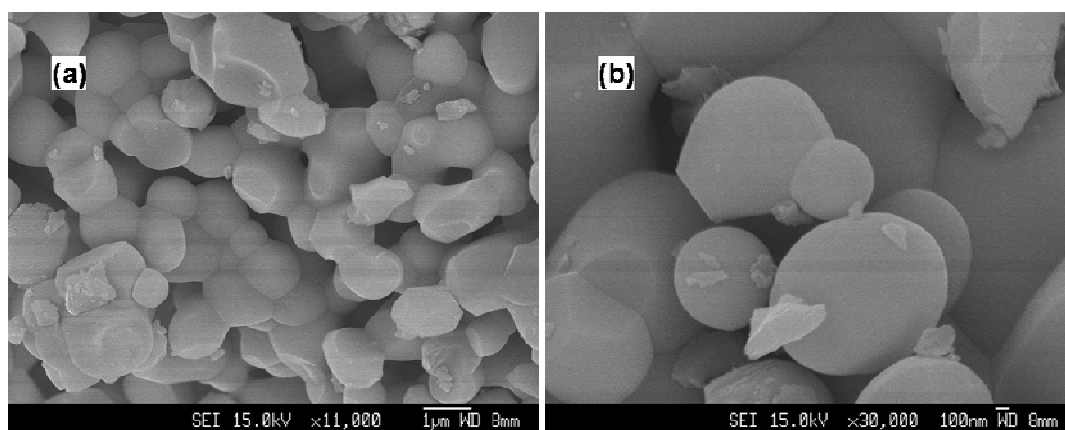


Figure 4-11: FESEM micrographs of YAG: Ce³⁺ calcined at 1600°C

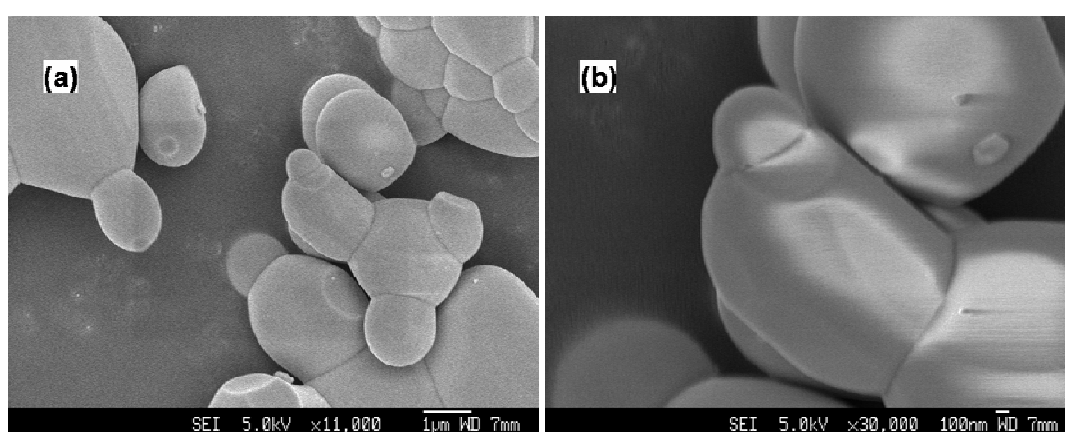


Figure 4-12: FESEM micrographs of the commercially-available YAG: Ce³⁺

It is interesting that the particles with their sizes at ~100 nm after calcination above 1300 °C were single crystals, as evident in the Rietveld refinement calculation and HRTEM (Figure 4-10). This shows that the nanoparticles were fine and uniformed in the size distributions. Because the driving force and growth rate are inversely proportional to the crystallite sizes [3], particles with large surface contacts were able to grow into single crystals without excessive deformation. This ability to form spherical morphology and single crystal YAG: Ce³⁺ at a size around 100 nm at high temperatures is a novelty of the chemical gelation process. By contrast, other chemical processes such as the homogeneous precipitation, a common method to produce spherical particles, has not been able to preserve the particle morphology at high temperatures [158].

4.1.4 HRTEM analysis of the single-crystal particle

The complex crystal structure of YAG: Ce³⁺ phosphors could be revealed by analyzing its atomic projection observed in the high resolution transmission electron microscopy (HRTEM). Figure 4-10b shows the HRTEM image of the single-crystal particle in [100] zone axis orientation. The as-collected experimental HRTEM images were not interpretable because the images were affected by the inhomogeneous thickness of the crystal and were taken under non-optimum defocus conditions. Therefore, it is imperative that the experimental images be reconstructed with the aid of crystallographic image processing technique [134].

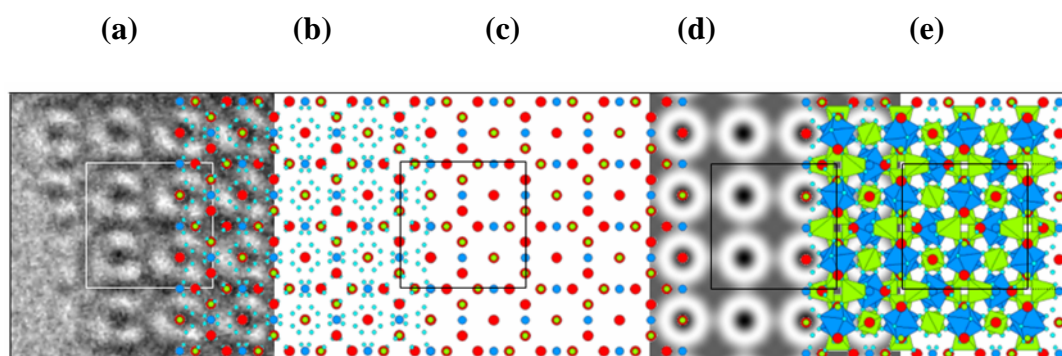


Figure 4-13: (a) HRTEM image and (b to e) simulated images (Key: Y^{3+} (red) ; Al(1)^{3+} octahedra (blue) ; Al(2)^{3+} tetrahedra (green) ; O^{2-} (light blue))

All of the possible 2D symmetries were tested through Fourier processing and lattice refinements. It was found that the symmetry $p4m$ had the highest calculated figure of merit for amplitude (RA%) and phases (ϕRes) [134]. This finding agrees with the one reported in International Tables for Crystallography for symmetry projected along $[100]$ [159]. Thus, the experimental HRTEM images were Fourier processed and imposed with the $p4m$ symmetry to yield a highly symmetrical image shown in Figure 4-13d (the unit cell is indicated by the squares in the figure).

The atomic structure of the garnet was simulated using a crystallographic drawing program (ATOMS) to illustrate the observed structural projection. They were superimposed on the HRTEM image so that the contrast in the HRTEM image could be represented by the overlaid atoms and polyhedra (Figure 4-13b, c, e). The white rings in the image are due to the absence of atoms. Inside each ring is a column of Y^{3+} and AlO_4 tetrahedra, being stacked alternatively along a fourfold (4_1 or 4_3) screw axis in $[100]$ direction. These screw axes are alternating throughout the cube faces of the unit cell [160].

Outside the rings are the AlO_4 tetrahedra arranged with counter-clockwise rotations around the screw axes, each 90° rotation is followed by a quarter of the lattice size (i.e. $a/4$) translation in the direction of the screw axes. The Y^{3+} ions are above and below the AlO_4 tetrahedra along these screw axes. Together, these atomic structures (both inside and outside the rings) appear as black dots in the image projection because the crystal is too thin. The observed crystal, calculated by the Multislice method, was about two unit cells (< 2.4 nm) thick. When the thickness is increased to three unit cells or above (> 3.6 nm), the columns of atoms appear as white dots in the calculated HRTEM image (Figure 4-14). One of the white dots is indicated by a green circle in Figure 4-14.

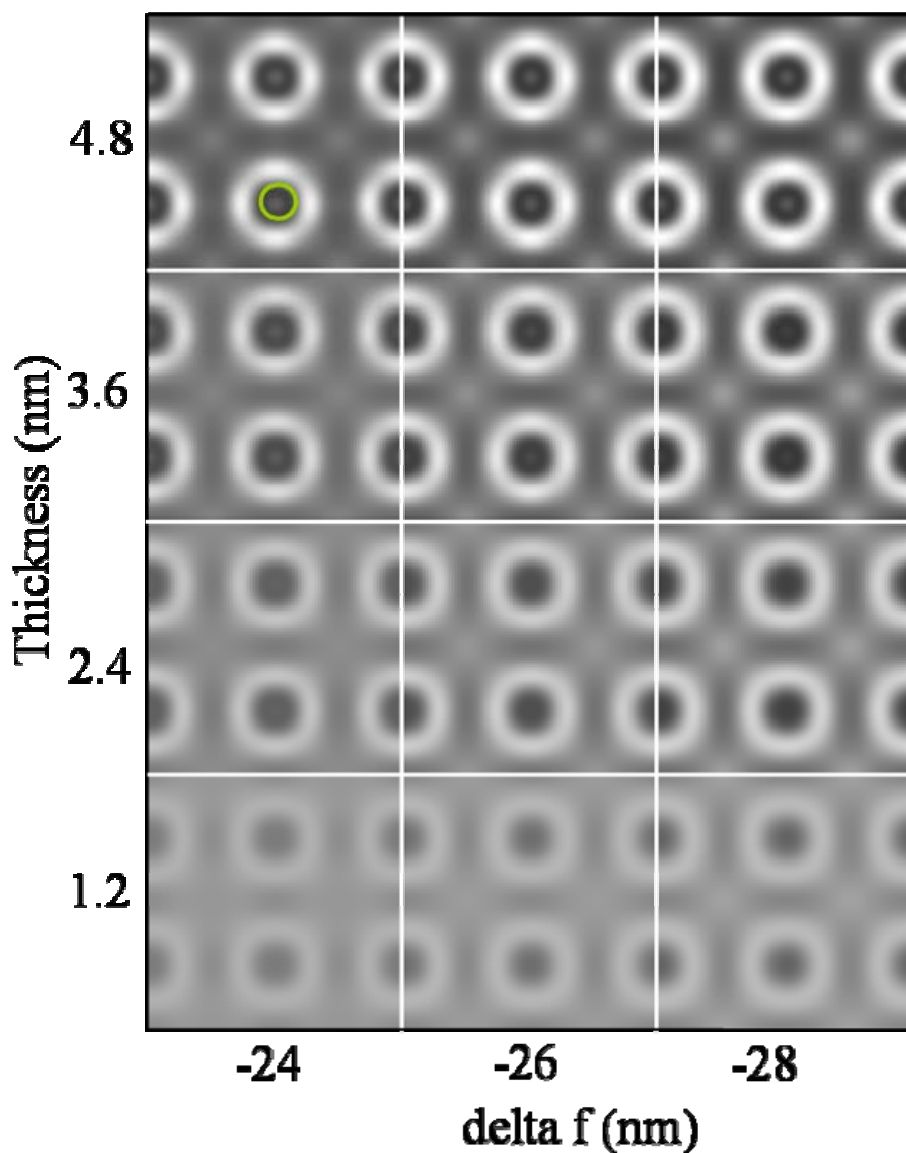


Figure 4-14: Calculated HRTEM image via the Multislice method

4.1.5 Summary

The chemical gelation method has been successfully used to synthesize YAG: Ce³⁺ nanophosphors with a size of about 30 nm. The crystallisation of the phosphors had progressed through three stages of dehydration and formed a pure cubic garnet structure at 900 °C, a much lower temperature than that required in a

solid state reaction method. Due to the nature of the gelling process, the nanophosphors were aggregated to form large spherical particles. This morphology was preserved even at high temperatures, a novelty of the chemical gelation method. The complexity of the garnet crystal structure was further unveiled through the study in the HRTEM images and simulations.

4.2 Synthesis of YAG: Ce³⁺ nanophosphors via a solvothermal method

As mentioned in Chapter 2, the synthesis of nanophosphors with a particle size less than 10 nm is a challenging task, because nanomaterials are thermodynamically unstable and it is much favorable for them to grow into bulk sizes [57]. Thus, the crystal growth must be inhibited by controlling their kinetic conditions, such as synthesizing at low temperatures. Another important consideration is the nanophosphors must be crystallized as formed so that it can exclude the post-process heat treatment, a step that is detrimental in controlling the nanoparticle sizes, especially for a size of less than 10 nm.

The successful synthesis method for the garnet nanophosphors is discussed in this section. The method used has switched from an aqueous route to a non-hydrolytic process or solvothermal, so that the reaction rate can be decreased and a controlled crystallization process can be achieved. The desired size and the spherical morphology of the nanophosphors can be obtained in this way. Hence the solvothermal process is an ideal process to be adopted in this synthesis.

4.2.1 Characterisation of the nanophosphor with a size of 5nm

The solvothermal process described in Chapter 2 requires the precursors to be soluble in the chosen solvent. In addition, a capping agent is required to constrain the particle growth and stabilize the nanophosphors. Based on this fundamental requirement, the 5nm nanophosphors had successfully been produced at a temperature 300 °C and solvothermally held for 6 days. This process involved a long chain alkylamine to act as an effective capping agent as well as a solvent in the solvothermal process, and had used mixed metal carbonates as the molecular precursors.

All the hydrated basic carbonates of the garnet components were dissolved in the oleic acid and oleylamine to form the transparent solution. This shows that the nanoparticles were very small in sizes (<10 nm) and did not cause light scattering. The structure of the nanoparticles comprises of two parts: The core and the organic capping shells (Figure 4-15 [4]). The core contains all the metal carbonate ions while their surfaces are coordinated with the amine groups in oleylamine and carbonyl groups in oleic acid. The long alkyl-chains of the organic shells are oriented away from the core.

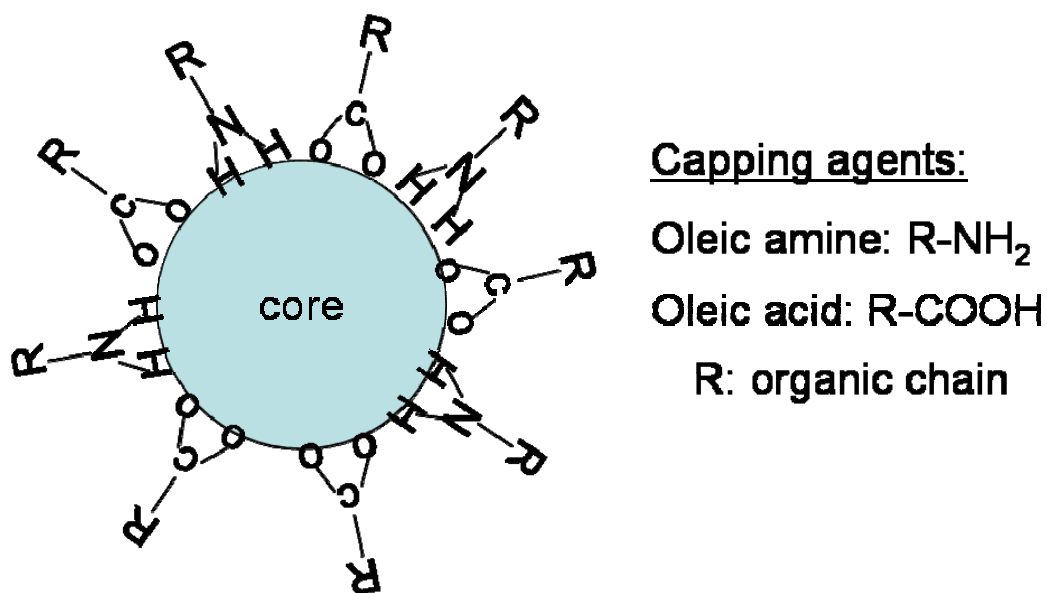


Figure 4-15: A core-shell structure [4]

In general, nanomaterials are known to have significant lower melting temperatures than their bulk counterparts [161]. Similarly, the decomposition temperature of the materials inside the nanoparticles is expected to be low too due to the increased ratio of surface-energy to volume-energy. During the solvothermal process, the decomposition of the metal carbonates-oleate complex inside the core was proposed to proceed as (M represents metal ions) [162-164]:



Equation 4.6 describes a simplified reaction. In general, the decomposition reaction produces an oxide and a volatile product (CO₂). The mechanistic process of the decomposition of the metal-(oleate)₃ complex is evident in the DTA/TG and

compared well with the mechanism proposed by Park *et al.* [63]. The nucleation that occurred at 220-240 °C was triggered by the dissociation of one oleate ligand from the complex precursor and was followed by CO₂ elimination. The subsequent growth mainly occurred at approximately 300 °C and was initiated by the dissociation of the remaining two oleate ligands from the complex precursor.

As soon as the decomposed materials formed a large number of crystalline nuclei from the supersaturated solution, the oleylamine (capping agent) with long-chain alkyl groups arrested the crystal growth by separating the particles from the slightly supersaturated solution so that further nucleation could be prevented. The oleic acid in this case, was used as a coordinating agent to mediate the nucleation process. Through this method, particles growth and shapes are controlled so that only spherical shapes and uniform sizes of 5nm are obtained. The components after the decomposition went through three stages of crystallization to form the garnet crystal phase.

First is the pre-crystallization stage. The strongly bonded AlO₄ groups form the short range order networks and are the first to appear in the solution. The weaker bonds (AlO₆) are still labile and they are free to move around in the solution. At the second stage, the AlO₆ groups are formed by corner-linking with the AlO₄ groups into a long range three-dimensional network. The structure now contains distorted cubic cavities that are fixed by AlO₆ and AlO₄ connections. This is the stage where the crystalline aluminate garnet of high-symmetry cubic structures is formed, determining the crystal's space group and lattice parameters.

The third stage is the post crystallization stage, whereupon the larger cations Y^{3+} and Ce^{3+} enter into the cavities of the crystallized structure. And this is the stage where the garnet requires long hours at low temperatures for the atomic diffusions (via solvothermal method). Another possible reason for the long synthesis time is that the cubic garnet structure is partially formed during the second stage and more time is required for Al^{3+} to diffuse into the networks, converting that into a garnet structure [165].

Eventually, the nanophosphors were crystallized with the garnet crystal phase after solvothermal at 300 °C for 6 days. Figure 4-16a is a transmission electron microscopy micrograph (TEM) showing the organic-capped spherical particles dispersed homogenously in toluene, and Figure 4-16b shows its particle size distributions with the average size at 5 nm.

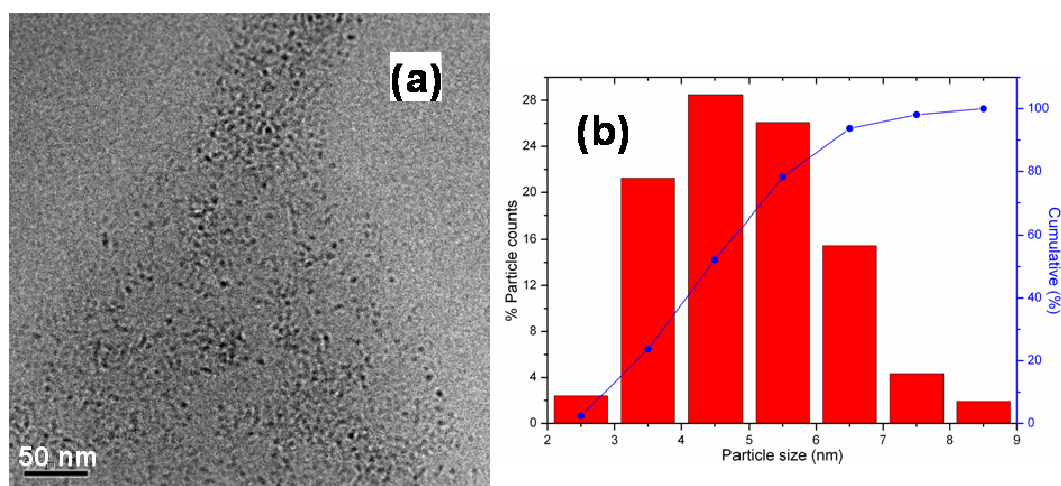


Figure 4-16: (a) TEM image of the nanophosphors and (b) its particle size distributions

The garnet crystal phase is evident in the HRTEM image and electron diffraction pattern (Figure 4-17a and b) with a good agreement between the observed and simulated one [132]. It is noted that the aggregation of the nanophosphors (Figure 4-17a) was due to the excessive washing of the nanophosphors which resulted in the removal of the capping agents. This washing is an essential step because the characterization of the garnet crystal structure under HRTEM mode requires no interference from the organic shell. The electron diffraction pattern was indexed with the crystal planes, and the intensity of the diffraction pattern intensity was simulated by broadening the line in accordance to the observed intensity (the yellow pattern in Figure 4-17b). The simulation results show an agreement in the calculated particle size with that observed in Figure 4-16a.

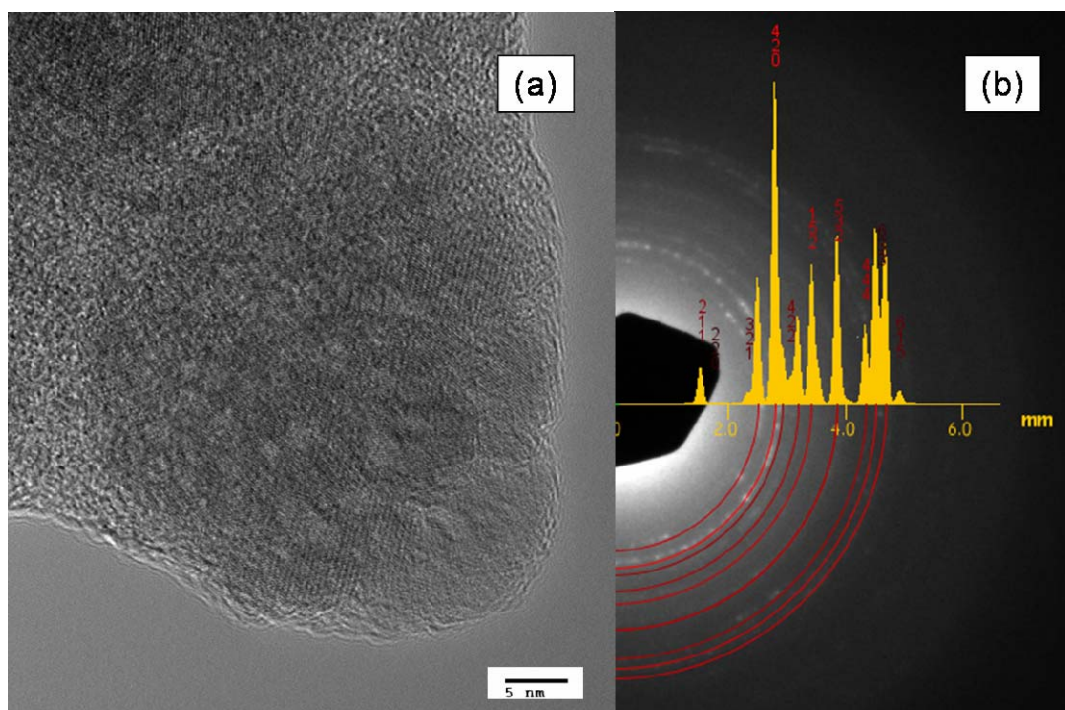


Figure 4-17: (a) HRTEM of the nanophosphors (b) Observed and simulated electron diffraction patterns of the nanophosphors

The structures of the molecular shells encapsulate on the surface of the nanophosphors were characterised using Fourier Transform Infrared (FTIR). Figure 4-18 shows a representative set of FTIR spectrum of the nanophosphors and Table 4-2 compares the organic capped nanophosphors with the oleylamine and oleic acid for their spectral characteristics.

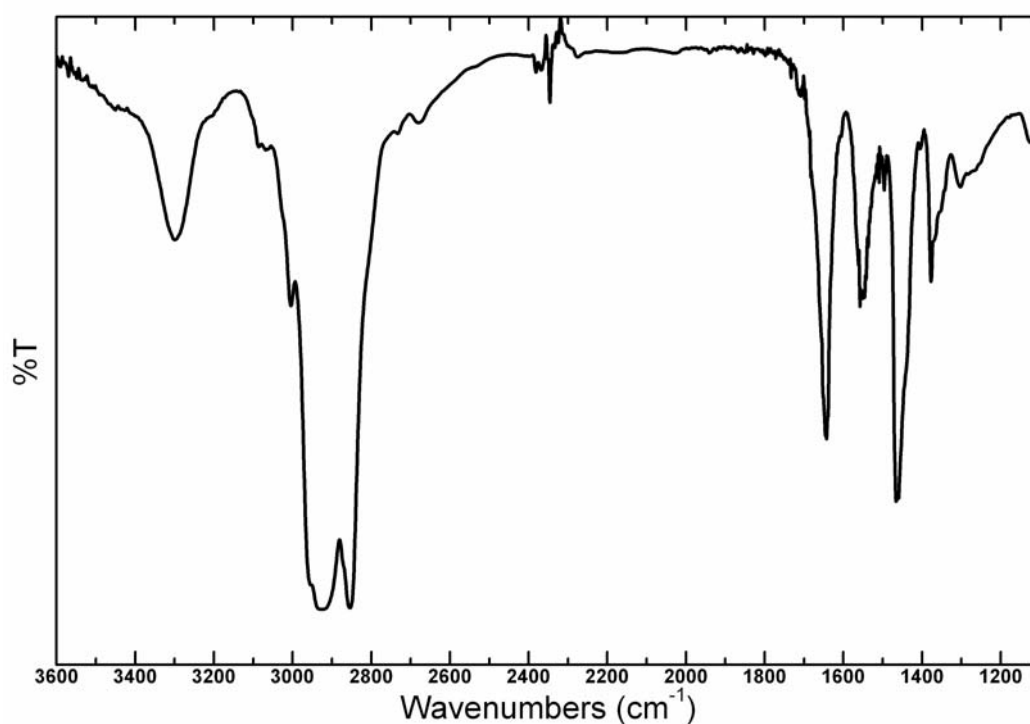


Figure 4-18: FTIR spectrum for the organic capped nanophosphors

Table 4-2: Comparison of the FTIR bands (cm^{-1}) for organic capped nanophosphors, oleylamine [4], and oleic acid [4]

Mode assignment	Organic capped nanophosphors	Oleylamine [4]	Oleic acid [4]
$\nu_a(\text{CH}_3)$	~2951	~2953	~2953
$\nu_s(\text{CH}_3)$	~2870	~2872	~2872
$\nu_a(\text{CH}_2)$	2925	2924	2925
$\nu_s(\text{CH}_2)$	2856	2853	2854
$\nu(\text{COOH})$	1712	-	1712
$\nu(\text{NH}_2 \text{ and } \text{NH}_3^+)$	1640	1580-1650	-
$\nu_a(\text{COO}^-)$	1558	-	-
$\nu_s(\text{COO}^-)$	1466	1465	1465

The spectrum was analysed in the low ($<2000 \text{ cm}^{-1}$) and high ($>2000 \text{ cm}^{-1}$) wavenumbers regions. Comparing the observed band assignments of the organic capped nanophosphors with the literature reported band assignment for oleylamine and oleic acid in the low frequency region, similarities were found in the carbonyl stretching mode of $-\text{COOH}$ in oleic acid, bending mode of $-\text{NH}_2$ and $-\text{NH}_3^+$ in oleylamine, and symmetry mode of $-\text{COO}^-$ [4]. These similarities infer that the surfaces of the nanophosphors are coordinated with both oleylamine and oleic acid. In addition, the similarities in the assignments for the bands in the high frequency region indicate that the hydrocarbon chain structures found in the organic shells of the nanophosphors were similar to oleylamine and oleic acid.

The stretching mode of the hydrocarbon (C-H) could provide the ordering properties of the chains [4]. The one in capped nanophosphors was about 8 cm^{-1}

higher than the reported bands for highly ordered and crystalline-like alkyl chains (2917 and 2848 cm^{-1}) on the nanoparticles, implying the presence of all-trans conformational sequences in the CH_2 chains [166]. This observation suggests a possibility of monolayer packing on the nanophosphors [166-170]. The small peak at 3004 cm^{-1} is an indication of stretching mode of the methylene group positioned next to $\text{C}=\text{C}$, a common unit which presence in both oleylamine and oleic acid. The $\sim 3300\text{ cm}^{-1}$ band is an indicative of the water from the hydrates of the carbonate precursors.

4.2.2 Characterisation of the near cubic shaped nanophosphors with a size of 250 nm

The precursor plays a vital role in the success of the solvothermal synthesis. In this synthesis, metal alkoxide which is a common molecular precursor in sol-gel was employed. This process involved benzyl alcohol as the solvent aid in the process, and TOPO and oleic acid to provide some degree of stabilisation. As introduced in Chapter 2, benzyl alcohol is a solvent aid which can control the crystallisation and stabilise the nanophosphors.

The formation of garnet nanophosphors via this method could react at a temperature ($250\text{ }^{\circ}\text{C}$) lower than the one ($300\text{ }^{\circ}\text{C}$) discussed in the last section. Both the reported particle sizes and crystallization temperature were significantly smaller and lower than other soft chemistry methods which also use metal alkoxides as their precursors [171-174]. This synthesis method is inevitably more superior than the solid-state reaction method in which the reaction temperature

required is $\sim 1600\text{ }^{\circ}\text{C}$ [175]. Therefore, it is important to describe its formation mechanism in this section.

It is noted that the alkoxide precursors used in this synthesis were chemically modified by acetylacetone (acac), a common chelating ligand used in the sol-gel process to form acetylacetonate alkoxides $\text{M}(\text{OR})_{n-x}(\text{acac})_x$ [176-182]. This modification increases the coordination number of the metal ion and reduces the nuclearity of the alkoxide precursor. As a result, the functionality of the precursor is decreased and in turn, it slowed down the hydrolysis rate [183]. This is particularly important when the rare-earth alkoxide precursors are used in the synthesis because of their high susceptible to hydrolysis. This modification is a key step towards a size-controllable process.

The free acid from the cerium acetate is an important component in the precursor because it acted as the acidic catalyst to accelerate the hydrolysis at a reasonable rate. The complexation ratio of acac to metal ions is another key parameter for obtaining small particle sizes because if the ratio is too low, a condensed and closed structure is unattainable and the chelating ligands orient the condensed species into weakly branched polymeric structures [182]. But, if the mole ratio is equal to one, the condensation growth is rapidly terminated outside the particles and hence, the spatial extension of the particle is prevented and the molecular clusters are formed.

The possible formation of the crystal nuclei is through a condensation mechanism that involves the modified metal alkoxides with benzyl alcohol. This

mechanism has been elucidated by Niederberger *et al.* [78]. They have done a thorough study by analyzing the supernatant (a reacted solution after removal of precipitate by centrifugation) using ^1H -, ^{13}C -NMR spectroscopy and coupled with gas chromatography-mass spectrometry (GC-MS) [5]. Hence, their proposed mechanism can be used to describe our material synthesis mechanisms.

The formation mechanism is likely to proceed mainly in a C-C bond formation route (Figure 4-19) [5]. It was first started by coordinating the benzyl alcohol with the metal atoms in the alkoxides. The resulted complexes weakened the C-O bond of the benzyl alcohol and activated the benzylic carbon atom for nucleophilic attack. One of the β -carbon atoms of the isopropoxy groups was deprotonated and led to a coordinatively saturated metal ion center. The benzyl group was sterically near the carbanion at the adjacent site of the intermediate metal center. Hence the complex was then formed through the rapid nucleophilic attack, coordinating with 4-phenyl-2-butoxide and an OH^- group. Further condensation of the metal monomer formed a network of M-O-M species via alcohol elimination. This complex network was eventually extended to oxide nanoparticles via the three stages of garnet crystallization described in Section 4.2.1 [165, 184].

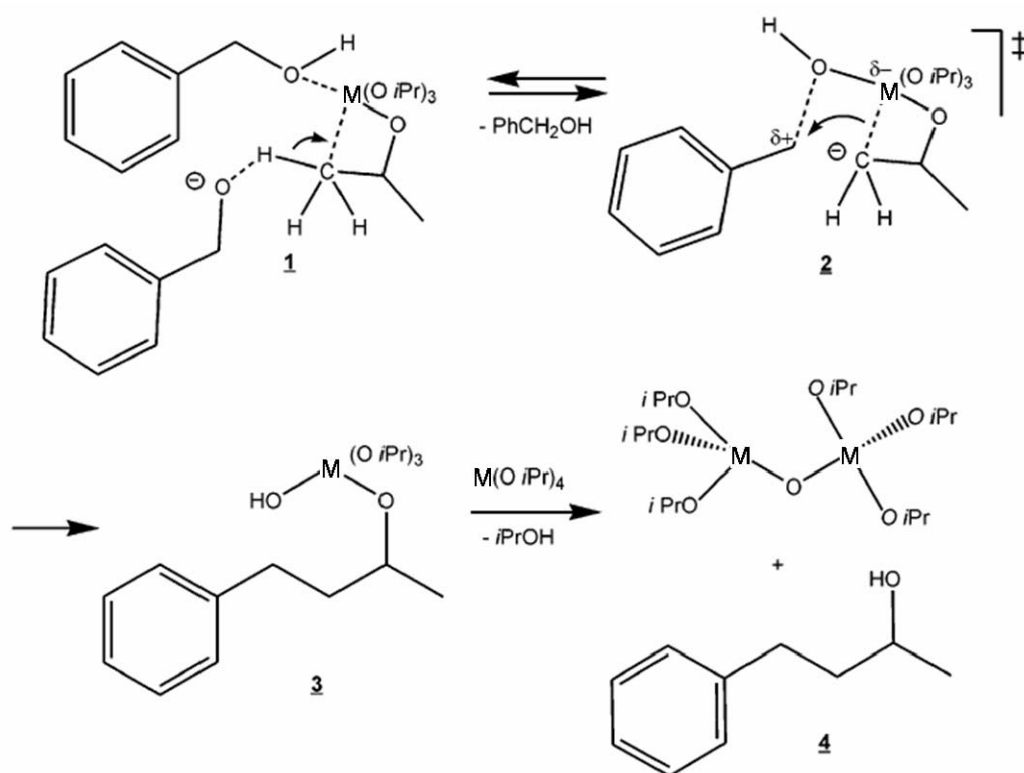


Figure 4-19: a C-C bond formation route [5]

In general, the synthesis of nanoparticles from solution requires that the nucleation and growth be separated [185]. The formation begins with a large number of crystal nuclei produced within a short timeframe from a supersaturated solution. Subsequently, the crystal growth is conditioned at a lower temperature and the capping agent arrests the crystal growth by separating the particles from the slightly supersaturated solution and so prevents further nucleation. Through this method, the shapes of the particles are controlled, the growth is uniform, and particle sizes of less than 10 nm can be obtained.

However, in the case of garnet crystal synthesis, it was difficult to reduce the growing temperature and at the same time, to achieve a complete crystallization. This challenge is presented by the results at different stages of the process: After solvothermal at 250 °C for 2 days, the molecular alkoxide precursors formed oligomeric clusters and there were connected with each other through their branches (Figure 4-20).

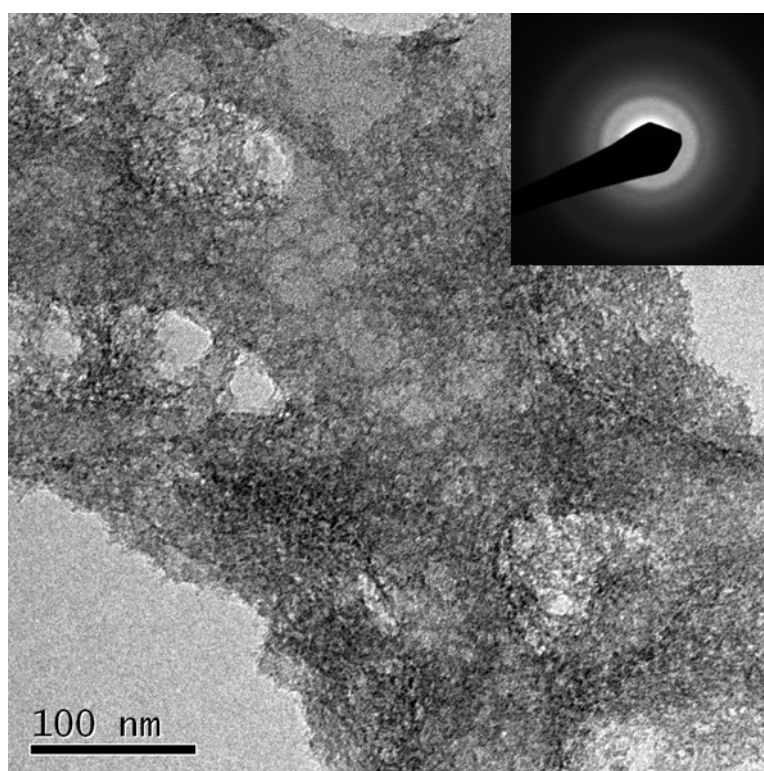


Figure 4-20: The branched oligomeric clusters and the electron diffraction pattern (insert)

Then after subsequent particle growth by continuing the solvothermal at a reduced temperature 220 °C for 7 days, the clusters had crystallised into particles and grown to approximately 10 nm in size. However, the prolonged growth durations had caused the nanophosphors to agglomerate into larger particles so as

to reduce surface energies (Figure 4-21). X-ray diffraction pattern shows that there was some amorphous phase (an amorphous hump at low diffraction angle) which further suggested that a much longer growth period was still required to complete the crystallisation (Figure 4-22a).

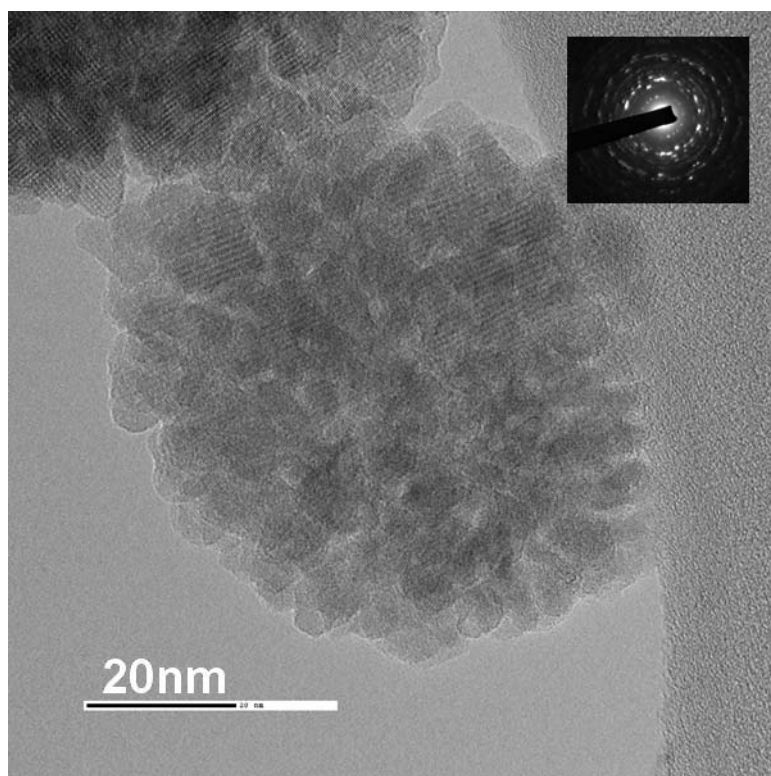


Figure 4-21: The aggregation of nanoparticles and the electron diffraction pattern (insert)

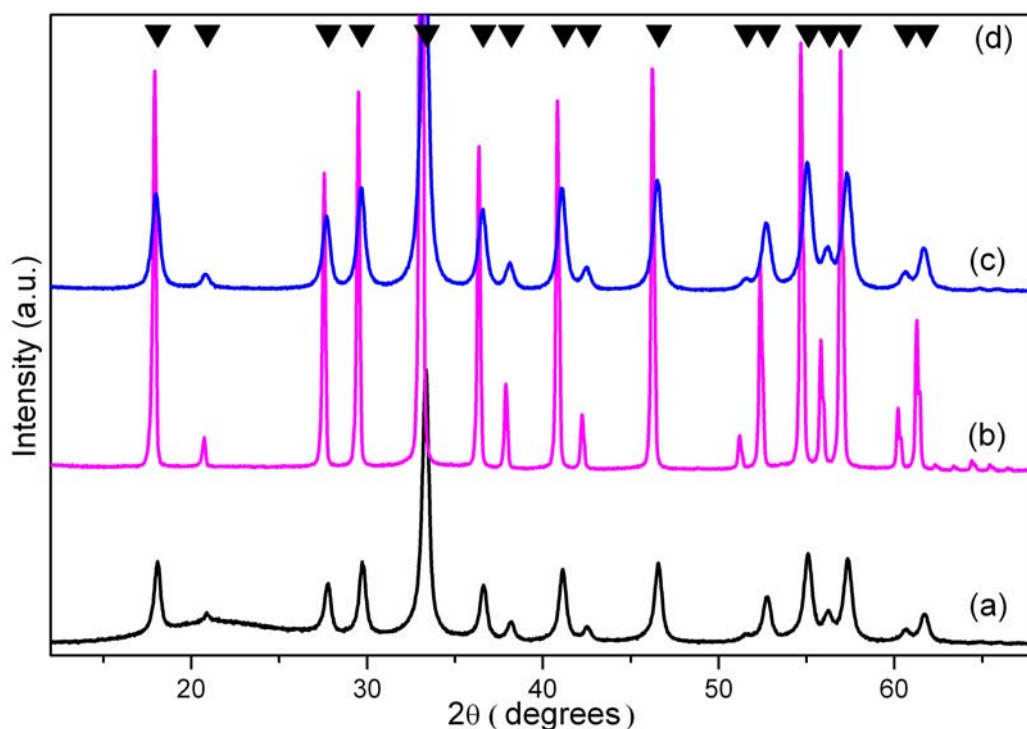


Figure 4-22: XRD patterns of (a) YAG: Ce³⁺ nanophosphor with incomplete crystallization (b) YAG: Ce³⁺ nanophosphor with a size 250 nm (c) undoped YAG nanoparticle (d) ICSD#93634 [6]

In order to complete the crystallisation of the nanophosphors, the solvothermal temperature was held constant at 250 °C for 9 days. By doing so, this process yielded highly crystalline and well-dispersed nanophosphors with the average particle size grown to approximately 250 nm (Figure 4-22b). The resulted particle morphology was a truncated cube shaped or multi-faceted polyhedron (e.g. tetradehedrons) (Figure 4-23a,b).

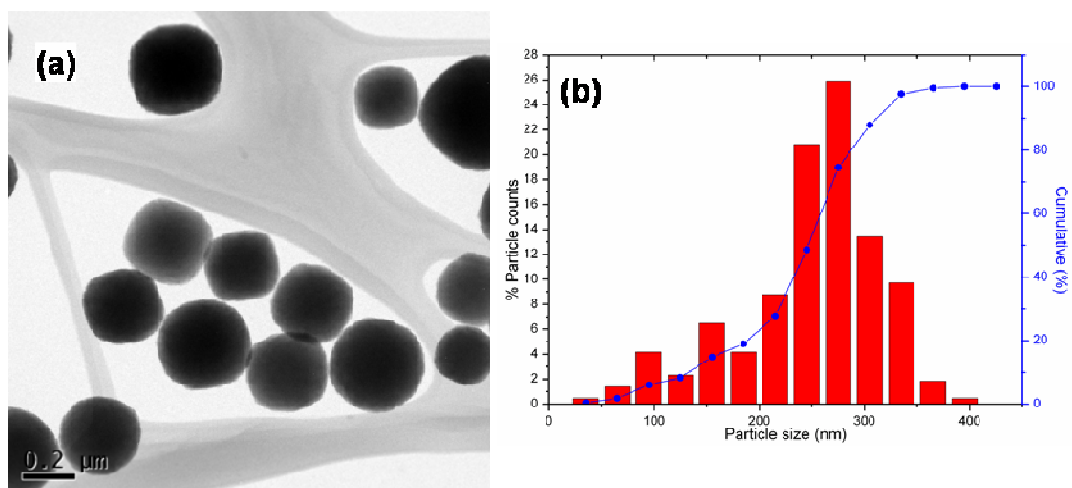


Figure 4-23: (a) Nanophosphors with near cubic shaped (b) The particle size distributions

Figure 4-24 shows the as-synthesised nanophosphors are a mixture of large and small sized nanophosphors, a consequence of the Ostwald ripening after the long growth times [186]. X-ray diffraction result shows an intense and sharp pattern which indicates the high crystalline nanophosphors had been produced (Figure 4-22b).

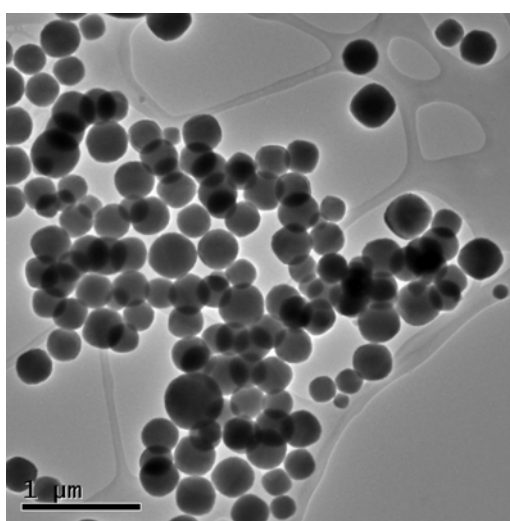


Figure 4-24: TEM images of the 250 nm nanophosphors

After the initial nucleation stage, the subsequent growth determined the final morphology of the nanophosphors via the balance between kinetic and thermodynamic growth regimes [187]. In general, the long growth durations produce the nanophosphors with thermodynamically stable shapes. Thermal energy in solvothermal process is sufficient (supplied by constant temperature for long solvothermal durations) to drive the crystal growth to the thermodynamically equilibrium phase, since the solvothermal temperature has kept constant at 250 °C and in this case, there is no reduction in temperature throughout the growth stage. It is noted that the cube is a thermodynamically stable shape as it has a lower energy than the sphere [187].

The structure of the garnet crystal is a body-centered cubic (BCC) whose surface $\{111\}$ has a higher energy than that of the $\{100\}$ surface [188]. Since the crystal growth was in the thermodynamic regime and the growth rates on different facets are in fact dominated by the surface energies, the growth rate on the $\{111\}$ surfaces was rapid. However, because the crystal growth was in the thermodynamic growth regime, only the low surface energy system is favored. Hence, the crystallisation front in $\{100\}$ grew favorably throughout the long solvothermal holding times, so as to increase the portion of low energetic surfaces. This explained why the nanophosphors have grown into large stable cube that bound by $\{100\}$ faces with marginal truncation on the corners (Figure 4-25a). This truncated crystal corner is magnified in the high resolution TEM micrograph, showing the surface with lattice projection in $\{100\}$ (Figure 4-25b). Lu *et al.* has studied similar formation mechanism for the semiconductor nanoparticles, and

they also concluded that surface energy is the driving force that drives the formation of nanocubes [185, 189].

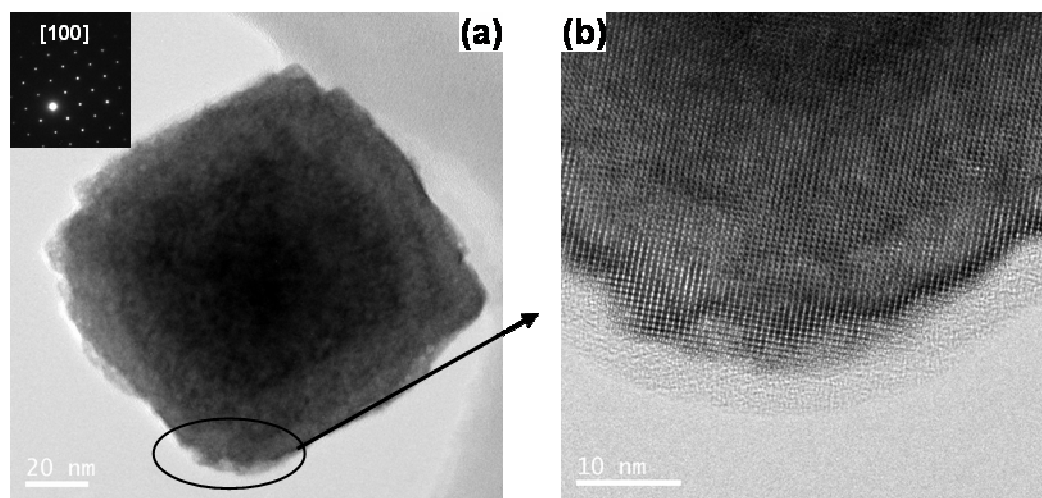


Figure 4-25: (a) A cubic single-phase nanophosphor and the electron diffraction pattern (insert) (b) HRTEM images of the particle's truncated corner

It is noted that surface energy can be modified by the surface adsorbed species. For instance, Jun and others have reported that for the rock-salt structure, the energy of the more energetic $\{111\}$ surface can be lowered than that of the $\{100\}$ surface through the capping agents due to the bridging of the thiol ligands on the $\{111\}$ surfaces [190]. A similar surface energy modification was found in our works: The carboxyl group of the oleic acid and the phosphine group of the TOPO may bind to the $\{100\}$ surfaces, and as a result, the $\{111\}$ surfaces became less energetic than $\{100\}$ surfaces. The growth could proceed on the $\{111\}$ surfaces to form the cube-like nanophosphors as they are much favorable for crystal growth on that surfaces in this case (Figure 4-26).

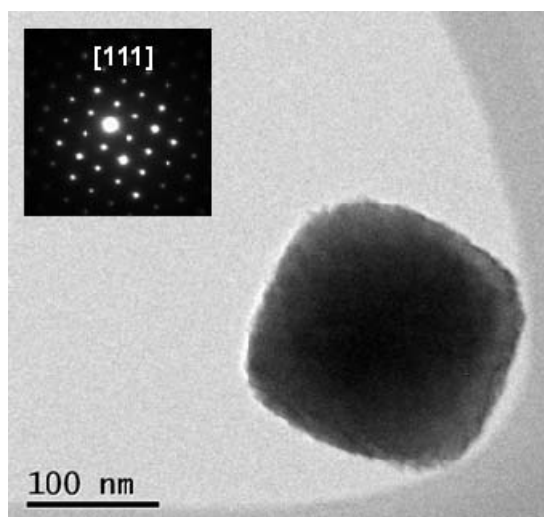


Figure 4-26: Nanophosphors with single crystal phase and the electron diffraction pattern (insert)

4.2.3 Structural comparison between the undoped & Ce³⁺-doped YAG nanophosphors

As mentioned in the beginning of this section, the precursor materials play a part in the solvothermal process, and it would be of particular interest to synthesis undoped YAG nanomaterials and compare the structure with the Ce³⁺ doped YAG nanophosphors. The process conditions (such as the capping agents and solvothermal temperature and time) were similar to the one used for the 250 nm nanophosphors. The result shows that the undoped YAG is different from the doped materials. The undoped YAG nanoparticles are found to be approximately 15 nm in size (Figure 4-27) and they are self-assembled into larger particles with an average size of 190 nm (Figure 4-28).

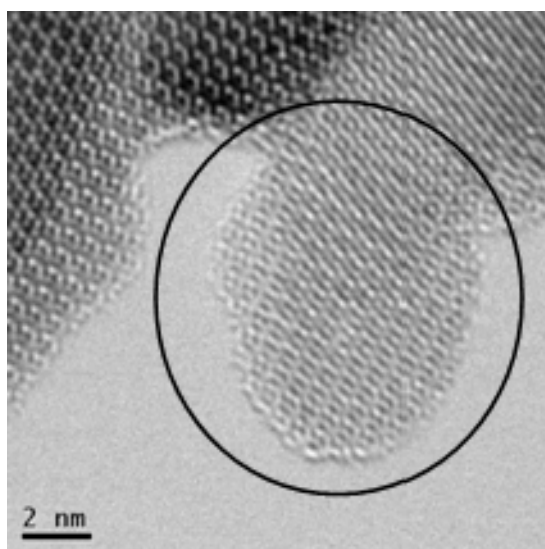


Figure 4-27: HRTEM images of the nanoparticle

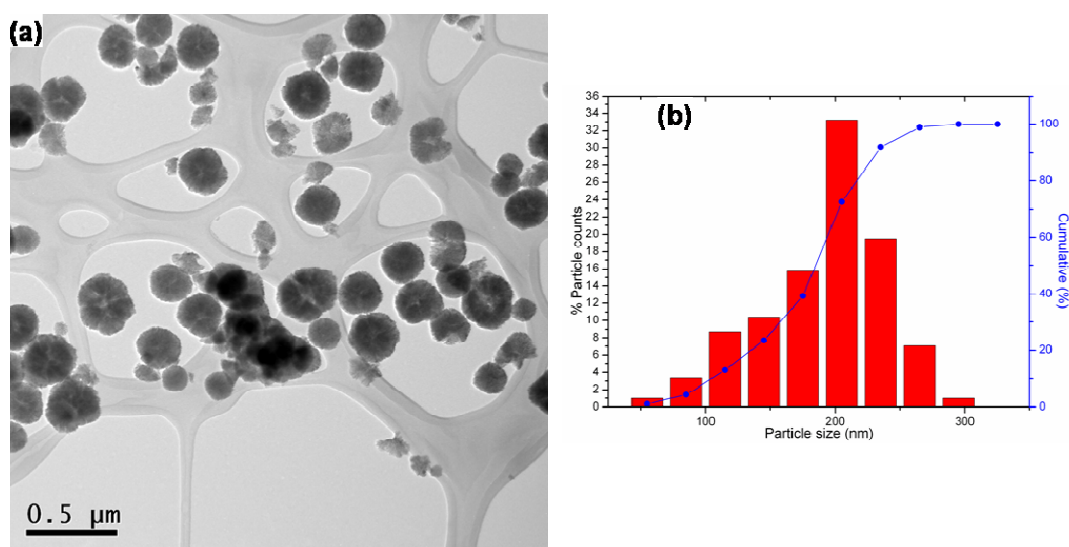


Figure 4-28: (a) TEM images of the undoped YAG nanoparticles (b) The particle size distributions

It is interesting to note that the undoped YAG nanoparticles were self-assembled into a cubic array, as evident in the small-angle electron diffraction pattern (Figure 4-29a). Generally, the surface of a nanoparticle contains high-

index crystallography planes which are most likely giving a high surface energy [189, 191]. Hence, it would be of much favorable for the nanoparticles to aggregate so that their surface energies can be minimized.

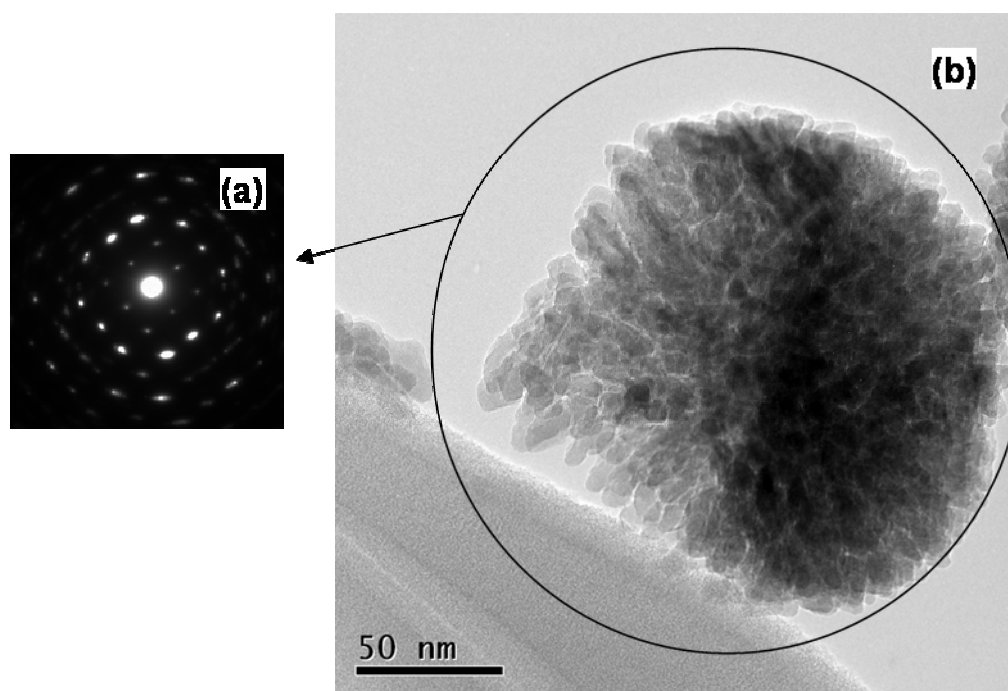


Figure 4-29: (a) The small-angle electron diffraction pattern of the cubic array (b) A self-assembly cubic array

While the doped nanophosphors, discussed in the previous section, are effectively cubic in shape, the undoped YAG is an assembly of nanoparticles in a large cubic array. Figure 4-29b has clearly shown the arrangement of each nanoparticle in a partially broken array. This structural difference could actually be explained through the crystallisation paths, since both structures are evolved from the amorphous alkoxide precursors.

In the undoped material system, the surrounding ions driven by the thermal energy continue to condense onto the nuclei surfaces. As the surface energy is the dominating factor in the growth rates of different crystal facets [187], the high energetic surfaces such as {111} and {100} would grow rapidly and propagate the crystallisation fronts to form the faceted nanoparticles. These high surface energies accelerate the aggregation of the nanoparticles into large particles, minimize the system's surface energy for a stable cubic formation. Since the seeds are cubes, the nanoparticles are grown into cubic in structure, and so their assembly is a cubic array. Feng and his coworkers have studied a similar crystallisation process through a molecular dynamics simulation to explain the formation of undoped faceted nanoparticles [192].

The cerium doped material system is also started as the crystalline cubic nuclei (seeds) and the surrounding ions continue to condense onto the seeds surfaces. The particles grow at a rate fixed by the solvothermal temperature and the degree of supersaturation. Subsequent crystallisation has evolved the energetically stable {100} surfaces and these crystallisation fronts have propagated to form the cubic nanophosphors. This process is in fact facilitated by the presence of cerium ions.

Section 4.2.1 highlighted that the crystalline aluminate garnet can form before they accommodate large Ce^{3+} ions in their distorted cubic cavities. Due to the large ionic sizes of cerium, the rate of diffusion into the cubic cavities is slow. This indicates that the seas of amorphous cerium ions, during the growth period, are concentrated on the surface (like a shell), encapsulating the growing particles

[3]. Such distribution of cerium ions allowed the system to minimise its surface energy so that the formation of more stable nanoparticles are facilitated, and hence the cerium ions enable the nanoparticles to retain the cubic structure throughout the growth periods. A similar crystallisation process was supported by the molecular dynamic simulation [192].

Figure 4-22 (b and c) shows the x-ray diffraction (XRD) patterns of the doped and undoped YAG nanoparticles, respectively. The line broadening of the cerium doped material is narrower than the undoped material which indeed shows that the particle size of the former is larger than the latter. And due to the dopant in the material, the reflections of the doped materials are shifted slightly to a lower angle.

4.2.4 Summary

The YAG: Ce³⁺ nanophosphors with a size of 5 nm were synthesized through the solvothermal method based on a nonhydrolytic approach. The success of this preparation has resolved the synthesis problem of obtaining a size of less than 10 nm without the need of heat treatment and it is the first to be reported here. An alternative precursor and capping agent was used to synthesize the nanophosphors with an average size of 250 nm. It is interesting that these nanophosphors are crystallized with a near cubic shaped and is a novelty of the solvothermal process. Another interesting study into the role of Ce³⁺ dopant in the formation of the nanophosphors has revealed that Ce³⁺ ions facilitate the crystallization process.

4.3 Structural characterisation of YAG: Ce³⁺ bulk phosphors

The bulk phosphors are generally synthesised by a solid-state reactions method (Section 2.1.1 has described the typical process). Due to the nature of the reaction where repeated grinding is required, the bulk phosphors are irregular in shape. The high processing temperature has caused the particles to grow beyond micron-sizes and they are heavily agglomerated.

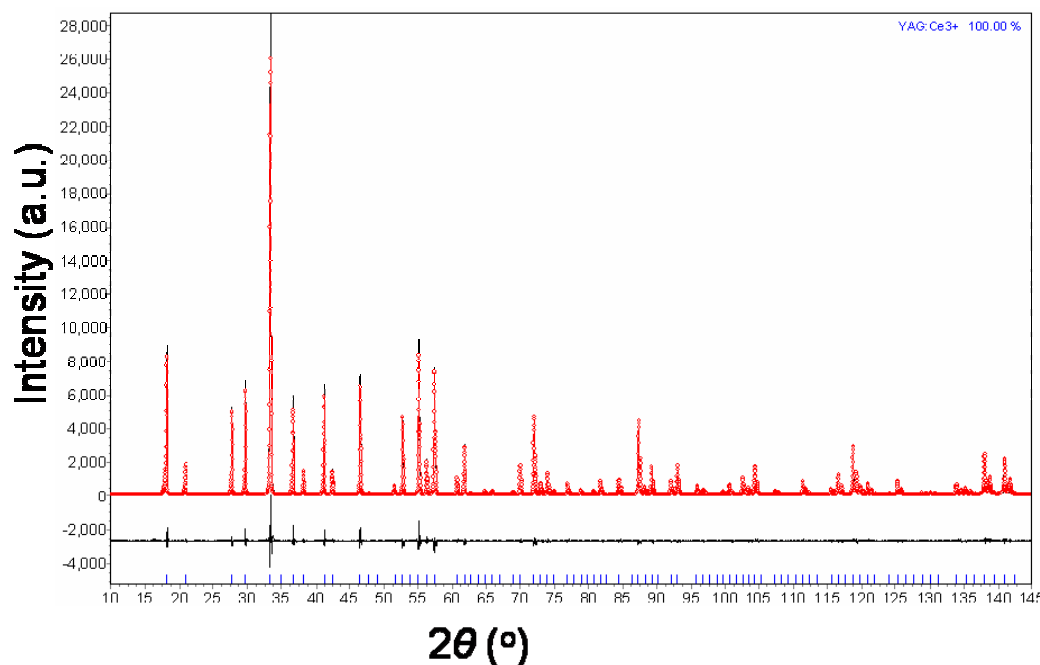


Figure 4-30: The Rietveld refined XRD pattern of the bulk phosphors

Figure 4-22 shows that XRD pattern of the bulk phosphors fitted with the calculated pattern by Rietveld refinement method. The measured and calculated XRD patterns were black line and red open circles, respectively. The solid lines at the bottom of the patterns represent the difference between the measured and

calculated patterns, showing a good agreement between the measured and calculated one. The vertical bars (blue) indicate the allowed Bragg peaks.

The XRD pattern of the bulk phosphors is typical of the highly crystalline and large crystal size where the line broadening is narrow (Figure 4-22). The Rietveld refinement analysis shows that the average crystallite size of the bulk phosphors used in this study was approximately 2.1 μm . It is in good agreement with the average sizes observed in the FESEM images ($\sim 1.9 \mu\text{m}$) (Figure 4-31a and b). Since the crystal sizes are large, fragments of the particles observed using the TEM are appeared as single crystals, as evident in the electron diffraction pattern (Figure 4-23d). The observed atomic projection of the phosphors (Figure 4-23c and g) was a p2 crystal symmetry as simulated (Figure 4-23e and f). The bulk phosphors were used to compare with the nanophosphors in this study.

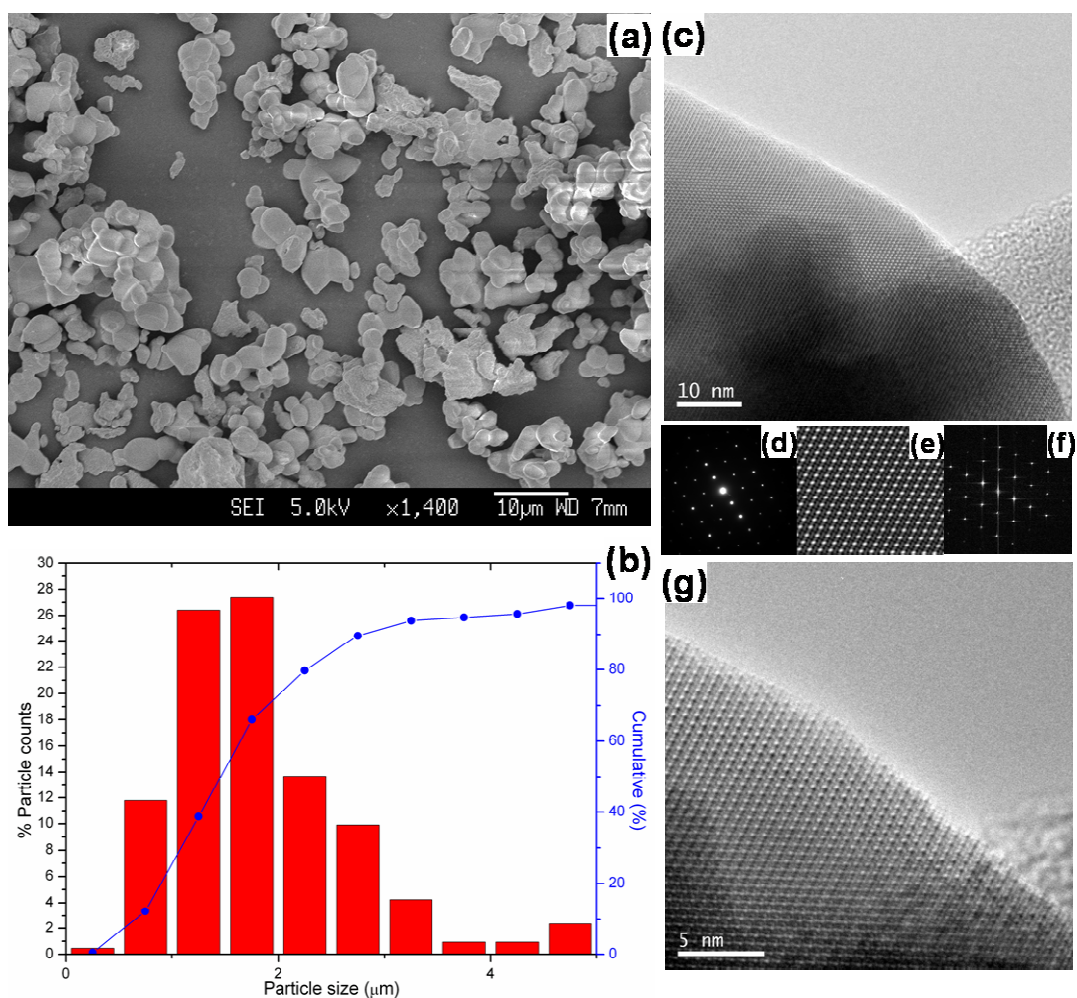


Figure 4-31: (a) FESEM image of the bulk phosphor (b) Its particle size distributions (c) TEM image of the phosphors (d) Electron diffraction pattern of (c) image (e) Simulated HRTEM image (f) Simulated electron diffraction pattern of (e) image (g) HRTEM image of (c)

4.4 Optical Properties of YAG: Ce³⁺

The syntheses and the structure analysis of the bulk phosphors and various nanophosphors with average sizes of 5 nm, 30 nm, and 250 nm were discussed in the previous sections. The influence of the YAG nano-environment on their optical properties is discussed in this section.

4.4.1 A comparison between the bulk and nanophosphors

One of the important applications that drives the development of the nanophosphors is the utilization of the nanophosphors as the emitting layer in the light emitting diode (LED) device [193-195]. Nanoparticles facilitate the coating process due to their well-dispersed nature. Furthermore, they can form a homogeneous thin layer on the substrates. However, the drawback for the usage of the nanophosphors is their quantum efficiencies. For example, the photoluminescence (PL) of Ce^{3+} in YAG (in the bulk state) is known to have high efficiency $\sim 70\%$ [54, 87]. However, when the particle size is reduced to nano-regime, its luminescence efficiency becomes poor. The highest reported efficiency of YAG: Ce^{3+} nanophosphors is about 54% [51, 54]. The reason for this poor emission efficiency in nanophosphors is still unclear. There are a few explanations given in literature [50, 51, 54, 87], and most of them attribute the poor efficiency to the presence of defective centres and the redox reaction of cerium ions.

Hence, the photoluminescence property of YAG: Ce^{3+} nanophosphors synthesized by the chemical gelation and solvothermal methods were investigated and compared with the commercially-available bulk phosphors. Since the nanomaterials have large ratio of surface-area-to-volume, the luminescence quenching sites were investigated by directly observing the surfaces of the nanophosphors using HRTEM. Through the analysis of the atomic projection of the HRTEM micrographs, the surface defective sites such as the non-bridging oxygen and incomplete garnet were identified [196]. This is an important evidence

that could lead us to the understanding of the luminescence quenching phenomena in the nanophosphors.

The photoluminescence of YAG: Ce³⁺ requires the cerium ions to be in the trivalent states. Therefore, the oxidation states of Ce³⁺ in YAG nanophosphors synthesized by the chemical gelation method were measured using X-ray Photoelectron Spectroscopy (XPS). Figure 4-32 shows the photoelectron peaks at 904 eV and 885 eV that corresponded to Ce³⁺ binding energies at 3d_{3/2} and 3d_{5/2}, respectively [197]. The satellite peak at 916 eV, a characteristic binding energy for Ce⁴⁺, was not detected in the XPS.

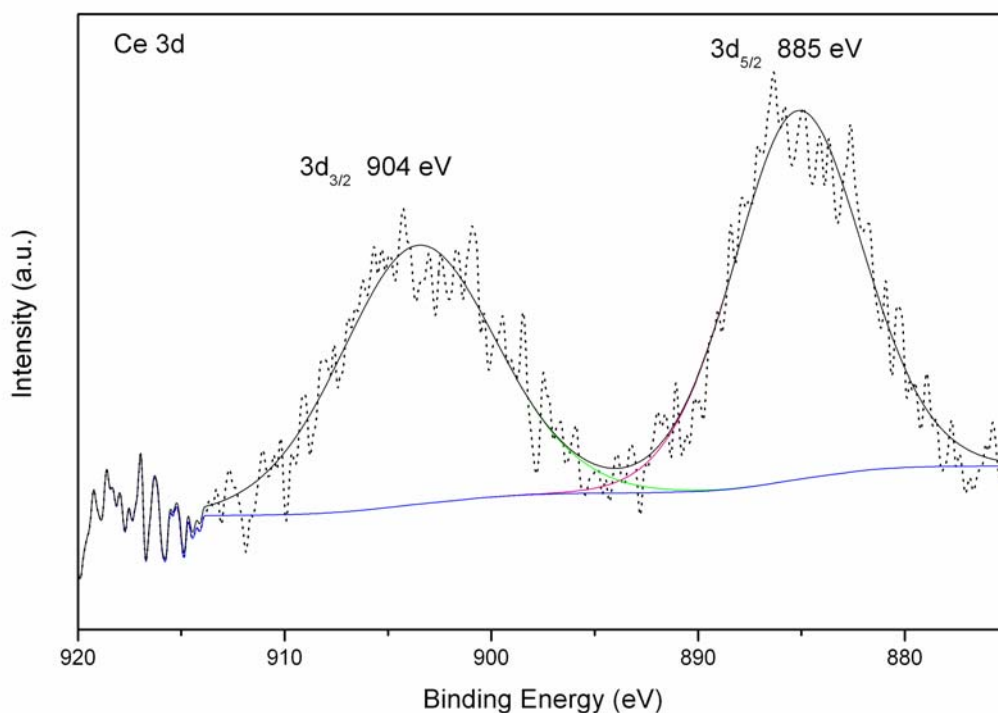


Figure 4-32: High resolution curve fitted (solid lines) XPS spectrum of Ce 3d showing spin-orbit splitting (3d_{5/2}, 3d_{3/2})

Another method which was used to determine the oxidation states of Ce^{3+} in the nanophosphors was XRD. The cerium (IV) oxide has diffraction (2θ) peaks at 28.5° and 47.5° and they were not detected in the XRD analysis (Figure 4-2, 4-22, and 4-30). Both XPS and XRD results show that Ce^{4+} was not present in the nanophosphors. This is a novelty of the chemical gelation method because other reported nanophosphors required post-annealing in a reduced atmosphere to reduce Ce^{4+} to Ce^{3+} [50]. The reduction process is detrimental to the phosphor's luminescence as it can increase the concentration of the oxygen vacancies that acted as the luminescence quenching centers [198]. The above-mentioned novelty has eliminated the hazardous annealing due to the usage of hydrogen gas at high temperatures, and has potentials in the process scalability.

The nanophosphors synthesised by the solvothermal method were unlikely to be oxidized from the trivalent to tetravalent states because the preparation of the precursors and the sealing of the reactor were done in an inert environment. In addition, the process reaction was at a low temperature and did not involve heat treatments in air. Hence, the oxidation state of the cerium ions in YAG was suggested to be in the trivalent state.

After the cerium's oxidation state in the nanophosphors was determined to be trivalent, the optical properties of the nanophosphors were characterised and compared with the commercial bulk phosphors. Both the photoluminescence (PL) and photoluminescence excitation (PLE) spectra were measured using fluorescence spectroscopy, a useful tool in monitoring the optical properties of the nanophosphors and in observing how they change with particle sizes. PLE was

used for the measurement because PLE spectroscopy is a useful technique that measures only the radiative transitions, facilitates the removal of the broadening effect due to size distributions on the absorption spectra of the nanophosphors, and helps in assigning the discrete optical transitions [7]. By using this technique, the optical transitions for the cerium ions in garnet crystals were obtained.

Figure 4-33 and Table 4-3 show the results of the photoluminescence excitation (PLE) and photoluminescence (PL) spectra for the bulk and nanophosphors. The kink occurring in the PLE spectrum at wavelength 457 nm of 250 nm nanophosphors is an artifact. In the PLE spectra of the nanophosphors of sizes 250 nm and 30 nm, the small peaks at wavelength 387 nm are likely due to the defects.

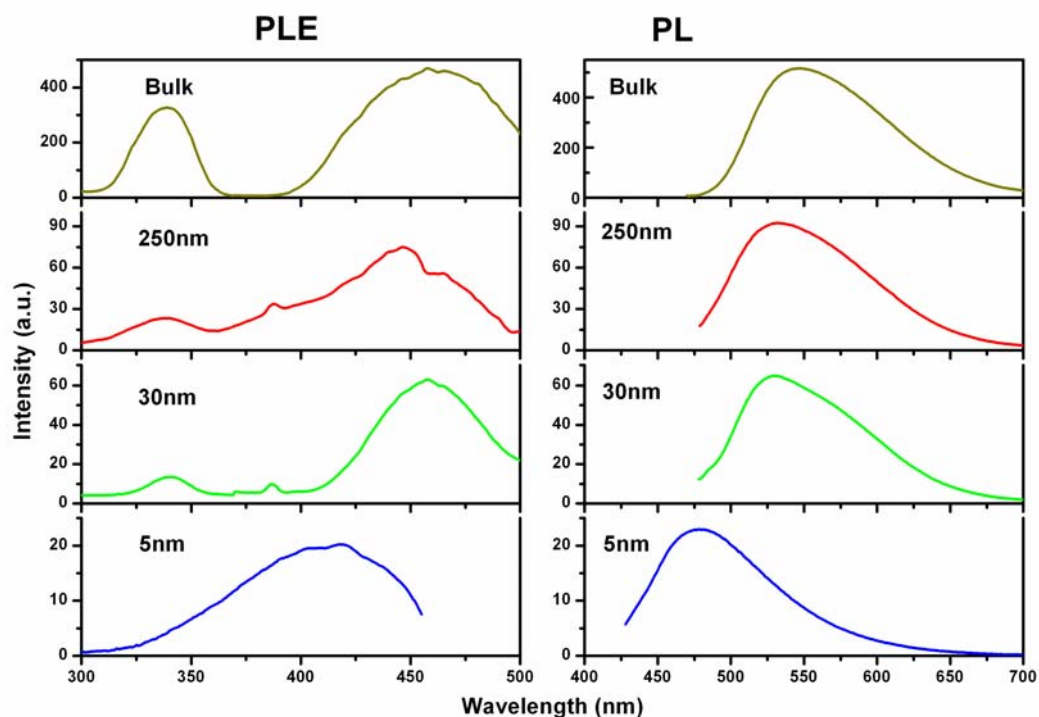


Figure 4-33: PL and PLE spectra of the bulk and nanophosphors

Table 4-3: Spectra comparison between the bulk and nanophosphors

Samples	PLE (nm)	PL (nm)	Stokes shift (nm)
Bulk	460	545	85
250 nm	459	533	74
30 nm	458	529	71
5 nm	420	480	60

The optical spectra of the nanophosphors were observed to have shifted to a lower wavelength (commonly known as a blue-shift in energy) as compared to the bulk phosphors whose emission peak is at 545 nm. The PLE spectra show the two prominent peaks at 460 nm and 340 nm which correspond to the lowest and second lowest 5d energy level of Ce^{3+} in YAG, respectively (as described in Section 2.2.1). It is interesting to note that the PLE spectrum of the smallest nanophosphors (5 nm) was comprised of a single peak at 420 nm only. The peak for the second lowest 5d level was not resolved in the measurement, and it might be lost in the tail of the spectrum. The peaks at wavelength lower than 210 nm correspond to the higher 5d levels of the cerium ion in YAG (which may overlap with the wavefunctions of the host conduction band). Since the optical properties of the garnet phosphors are mainly dependent on the lowest and second lowest 5d levels, the discussion on the comparison between the bulk and nanophosphors is focus on these two electronic energy levels.

The optical properties of the phosphors are determined by the electronic structure of the cerium ions in the materials, and in turn, they are affected by the

changes in the local crystal environment in the excited state. Hence, the nanostructures of the phosphors have strong influences on their optical properties.

Table 4-3 shows a decrease in the Stokes shift with a reduction in size. This size-dependent phenomenon could be understood using Ce^{3+} in cryptand ligands as an example. $[\text{Ce} \subset 2.2.1]^{3+}$ cryptate has a smaller Stokes shift than $[\text{Ce} \subset 2.2.2]^{3+}$ because the 2.2.1 cryptate has a small organic cage which does not allow the expansion of Ce^{3+} upon excitation [97]. So, this example infers that the degree of restriction for Ce^{3+} expansion in the YAG nanoenvironment becomes larger with the reduction in size. Thus, a reduced Stokes shift has been observed as the nanophosphor size is reduced.

The electronic structure of cerium in YAG is known to be affected by the local crystal environment. In order to find out the extent of changes, the internuclear distance between the cerium ion and ligands should be determined for both the ground and excited states. However, while the internuclear distance ($\text{Ce}^{3+}\text{-O}^{2-}$) for the bulk and nanophosphors in the ground state (approximately 2.37 Å) can be determined through the Rietveld refinement method [136], the changes in the internuclear distance upon excitation could not be possibly determined by a similar approach.

Fortunately, based on the results on the electron-phonon coupling showing that the nanophosphors have a weak coupling strength (a result of which is discussed in the later sections), and those suggesting a correlation between a strong electron-phonon coupling strength and high degree of covalency [101, 102], YAG:

Ce^{3+} nanophosphors are concluded to have a small degree of covalency upon excitation.

Since the smaller the size of nanophosphors, the less its degree of covalency, the electronic transitions shift to higher energy with a reduction in size. This is because the overlap between the electronic wavefunctions of Ce^{3+} and ligands is weak, resulting in a blueshift in energy. This is in agreement with the work of Igarashi *et al.* [100], which suggested an increase in ionicity (or a decrease in the degree of covalency) of the $\text{Eu}^{3+}\text{-O}^{2-}$ bond with a decreasing particle size and a blueshift in the electronic transition.

Another reason which causes the blueshift in spectroscopic spectra and the changes in the Stokes shift is the surface-tension effect: This effect increases with a reduced in the particle size [199]. Again, this effect can be understood from the confined nature of the nanoenvironment where the expansion of the cerium ions were being restricted [196].

Luminescence efficiency is an important feature to be characterized. The commercially-available YAG: Ce^{3+} bulk phosphors have $\sim 70\%$ luminescence efficiency [54, 87], while the relative efficiencies calculated for the 250 nm and 30 nm nanophosphors were found to be less than 20 %. This reduced efficiency found in the nanophosphors is due to the enlarged surface-area-to-volume ratio that increases the surface defects concentration and in turn, gives rise to a luminescence quenching. By contrast, the optical efficiency of the 5 nm nanophosphor,

measured to be closed to 60 %, becomes comparable to that reported by Haranath *et al.* [54], although still lower than that of the bulk phosphors.

An effective way to enhance the luminescence is through a core-shell approach as previously reported for semiconductor nanocrystals [69, 70]. The selection criteria of the shell material are such that it has an electronic band gap wider than the core, and is able to grow epitaxially onto the core to avoid the strain induced by lattice mismatches. Unfortunately, this method is not applicable to the garnet nanophosphors because of few choices of materials with a matching lattice size and a band gap wider than the YAG.

Nevertheless, the luminescence improvement observed in the 5 nm nanophosphors suggests that the organic shell that was passivated on the nanophosphors had partially eliminated the surface defects. It is interesting to note that all the nanophosphors in this study are more efficient than the commercially available sulfide-based yellow emitting phosphors (P-20) whose efficiency is only 12 % [54].

4.4.2 Investigation of the surface defective sites

Nanophosphors are known to have a higher ratio of surface-area-to-volume than the bulk phosphors. This implies that the concentration of the defects on the surfaces of the nanophosphor is higher than that in the bulk phosphors and the emission quenching due to these defects are significant [51, 193]. Hence the surface-defective sites such as incomplete garnet lattice and nonbridging oxygen

were investigated using the high resolution transmission electron microscopy (HRTEM). The HRTEM image for the 30 nm nanophosphors is used to elucidate the surface defective sites (Figure 4-34) (the unit cell is indicated by the squares in the figure).

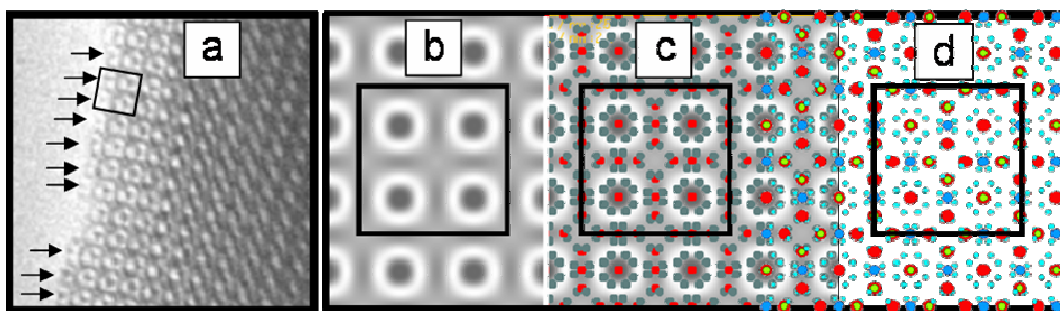


Figure 4-34: (a) HRTEM image of the nanophosphor surfaces (b) A simulated HRTEM image (c) Atomic projection by the Multislice method (d) Atomic projection by ATOMS

The garnet lattices observed in Figure 4-34a are in symmetry projection $p4mm$ [159]. This HRTEM image could be reconstructed using a crystallographic image processing technique [134]. The experimental HRTEM images were fast Fourier processed and imposed with the $p4m$ symmetry to produce a symmetrical image and a portion of which is shown in Figure 4-34b. The atomic structure of the garnet was simulated using the Multislice method [132] (Figure 4-34c) and a crystallographic drawing program (ATOMS) (Figure 4-34d) to illustrate the observed structural projection. All simulated images have been superimposed on the HRTEM image so that the detail contrast in the image could be illustrated by the overlaid atoms.

The white rings in the HRTEM image represent the absence of atoms. Inside each ring, YO_8 distorted cubes and AlO_4 tetrahedra are stacking alternatively in a column along a fourfold (4_1 or 4_3) screw axis. This column appeared as a black dot because the crystal is too thin. The AlO_4 tetrahedra (outside the rings) are arranged with counter-clockwise rotation and a translation with $\frac{1}{4}$ of the lattice size in the direction of the screw axes.

It is observed that the garnet lattices are incomplete on the surfaces of the nanophosphors (as indicated by the arrows in Figure 4-34a) because most of them appeared only as half-rings. This indicates that the AlO_4 tetrahedra outside the rings are not present and the columns inside the rings which consist of YO_8 and AlO_4 are missing too. Those incomplete garnet lattices behave as different crystal hosts and resulted in nonradiative electronic transitions. For example, the surface lattices became a nonstoichiometric compound or sesquioxide where Ce^{3+} in sesquioxide is characterised by its quenched cerium emission [200]. This observation was supported by Lehmann *et al.* [109] who used the site-selective spectroscopy to study the optical properties of the dopants and had differentiated their different emissions for the one on the surface and in the interior of the nanophosphors.

It is worth noting that the bulk phosphors have the same defective sites. Because they had a large volume of complete garnet lattices in the bulk body, those defective sites on the surface are not significant. On the contrary, nanophosphors have high surface-to-volume ratio and those defective sites have a profound effect on the nanophosphors' optical properties.

The moisture in the air can have an effect on the chemical properties of the nanophosphors. Water and carbon dioxide from the atmosphere react with large quantities of nonbridging oxygens in the incomplete garnet lattices. This surface reactions with the surrounding produce hydroxyl-carbonate ligands on the nanophosphors [55, 201-203] . This is evident in FT-IR measurements (Figure 4-35). The IR absorption spectrum of the strong carbonate band is near 1400 cm^{-1} , and it is clearly featured in the one measured for as-synthesized powders before the heat treatment. After calcination, this carbonate stretching vibration band is no longer present in the spectrum. This implies that the adsorbed carbonate ligands are eliminated and the calcined nanophosphors are inert to the carbon dioxide in the atmosphere. However, the hydroxyl ligands are still present on the surfaces of nanophosphors, as shown by the stretching vibration band $\sim 3600\text{ cm}^{-1}$.

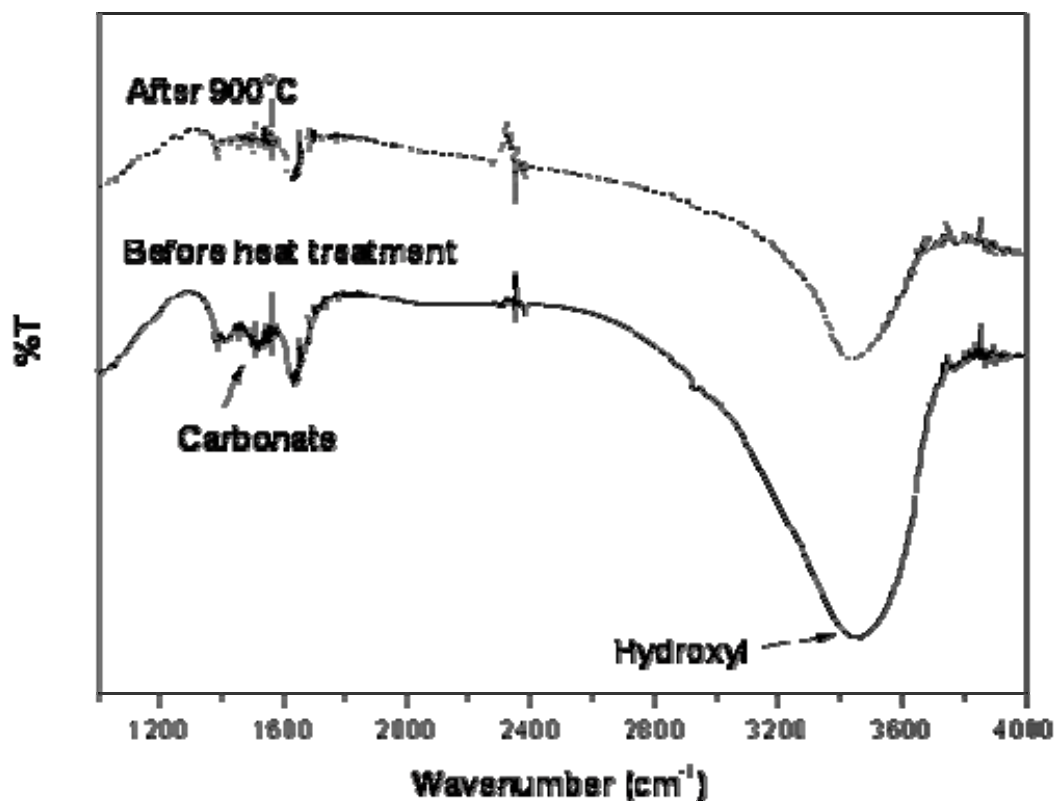


Figure 4-35: FTIR spectrum of the nanophosphors

The surface hydroxyl groups and the nonbridging oxygens can act as the electron-trapped centers [204]. After the Ce^{3+} electrons are excited from $4f$ to the second lowest $5d$ level, the electrons are then lost to the conduction band and are trapped at these defective sites. As a result, the nonradiative decay occurred as the recombination of the electrons and holes are impeded. The high concentration of these defects on the surfaces of nanophosphors explains the strong quenching of the luminescence measured in the nanophosphors. Therefore, it is important to eliminate those defective surface states. The capping (passivation) agent could play a role in enhancing the luminescence efficiency as reported by literature [70, 205, 206]. This has been shown by using the capping agent with long alkyl-chains

to encapsulate the 5 nm nanophosphor, resulting in improved luminescence efficiency.

4.4.3 Investigation of the size-dependent electron-phonon coupling

Despite the myriad of important applications of Ce^{3+} doped YAG nanophosphors, not much is known about the size-dependence of the electron-lattice relaxation process. Ce^{3+} has the simplest electron configuration ($4f^1$) among the rare earth ions, and its luminescence transition ($4f-5d$) in YAG is parity-allowed and appears as distinct bands in excitation spectra [2]. Thus, changes of the band positions and intensities can be readily observed. Furthermore, the $5d$ wave function has a large radial extension, which amplifies the influence of the lattice environment over the electronic states. To sum up, Ce^{3+} doped in an insulating YAG host lattice provides an ideal system for studying fundamental interactions between phonons and electronic transitions, an issue of both fundamental and technological importance. The objective of this section is to understand the influence of YAG nanoenvironment on the electron-phonon interactions and quantum dissipation through the combination of experimental and theoretical efforts.

The observed Ce^{3+} optical response in YAG was treated with the multimode Brownian oscillator model (BO), a theoretical framework to model optical responses during excited-state relaxation in solutions and solids. The parameters used in the calculations for all samples are shown in Table 4-4. The value of the dissipation coefficient γ_j is chosen to be the same for all samples,

except the 5 nm size nanophosphors. The larger dissipation coefficient γ_j in the 5 nm nanophosphors suggests that its electronic transition is accompanied by a large lattice relaxation due to the enlarged ratio of surface-area-to-volume ratio. The calculated spectra were compared with the measured spectra in Figure 4-36. A good agreement between theory and experiment was obtained indicating a successful application of the BO model to explain the observed emission broad band of YAG: Ce³⁺.

Table 4-4: Parameters used in the BO model

Samples	Bulk	250nm	30nm	5nm
S_j	1.90	1.88	1.72	1.57
ω_j (cm ⁻¹)	1277	1277	1277	1277
$r = \gamma_j/\omega_j$	1	1	1	2
ω_{eg}^0 (eV)	2.47	2.54	2.51	2.72

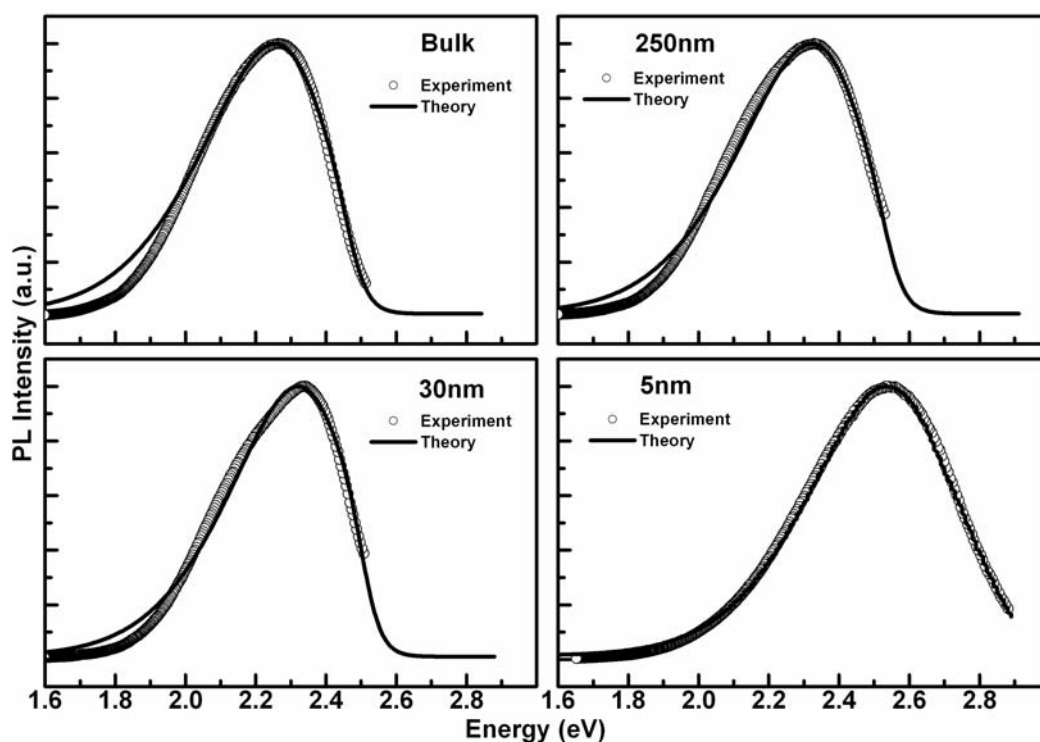


Figure 4-36: Measured and calculated spectra

The pure electronic transition energy $\hbar\omega_{eg}^0$ of Ce^{3+} in YAG is of 4f-5d configuration type and is about 2.7 eV [91]. The results show that $\hbar\omega_{eg}^0$ in both the bulk and nanophosphors is less than the theoretical value by ~ 0.2 eV (cf. Table 4-4), implying that the excited electrons in 5d could have been transferred to a defective center lying at a lower energy level. As such, the observed Ce^{3+} emission could be due to the radiative decaying of the electron from the defective center to 4f accompanied by a lattice relaxation. This interpretation is consistent with the study by Shi *et al.*, which showed that electrons responsible for the ZnO green emission were localized around deep centers resulting in transition energies below the fundamental band gap [123].

In bulk samples, a defective center is likely to be one of the high-concentration surface defective states and oxygen vacancies. These defects are generated due to repeated grinding, milling, and heat treatment in reduced atmosphere, which are the typical solid-state reaction steps in the synthesis of bulk phosphors. In nanophosphors, the defective centers are attributed to the surface defects such as the incomplete garnet lattices and nonbridging oxygens as described in an earlier section. It is important to note that the increased surface-area-to-volume ratio in the nanophosphors amplifies the influence of the surface defective centers on the optical properties [104, 105, 207]. To further elaborate this influence, Chen *et al.* concluded that the coupling strength in nanoparticles is determined by the surface states [111]. They explained the recombination of the exciton was impeded due to the trapping of electrons or holes at the surface states, which in turn led to an enhancement in the coupling strength [103]. They further discussed that reducing the particle size decreased the density of states for the electrons and phonons, which however, led to a weaker coupling strength [106].

In our study, the results for our calculations in Huang-Rhys factor, a dimensionless constant that characterized the strength of electron-lattice coupling [142, 208], are consistent with the findings of the aforementioned studies (described in Section 2.2.4) for the rare earth doped materials, showing a decrease in the coupling strength with reducing particle sizes [106, 111]. A similar trend is also observed in other nanoparticles of different material systems. For example, studies in the Raman scattering spectra of various particle sizes had shown a decrease in the coupling strength with the reducing size [99, 117]. Even a 2D quantum structure exhibited similar results. In quantum wells, for example, Sun *et*

al. found that reducing the well width could decrease the coupling strength due to the increased exciton binding energy in the quantum structure [118, 209].

4.4.4 Summary

In conclusion, the success in synthesizing nanophosphors with the targeted sizes has made possible the study of the optical properties of nanoscale YAG: Ce³⁺. The findings in this study show that the optical responses of the phosphors are size-dependent and are related to the Stokes shift, covalency, surface defective centers, and electron-phonon interactions. Calculations of the Huang-Rhys factor using the BO model show that the electron-phonon coupling strength decreases with the reducing phosphor size.

Chapter 5: Conclusions & Recommendations

5.1 Synthesis of the YAG: Ce³⁺ nanophosphors via the chemical gelation

A novel approach to produce spherical and nonagglomerated YAG: Ce³⁺ particles was successfully demonstrated via the chemical gelation method at a low temperature (900 °C).

XPS and XRD studies revealed the oxidation state of cerium ions in the nanophosphors to be Ce³⁺. Hence, the result shows that no postannealing in reducing atmosphere is required. The water-in-oil emulsion (during the gelation) had enabled the formation of the spherical gel particles when the ammonia gas was introduced. A pure YAG cubic structure was crystallized from the amorphous phase after heat treatment at 900 °C for 2 h in air, showing improved homogeneous mixing and increased reactivity of the precursors. This crystallisation had progressed via three stages of dehydration in the duration of the thermal process. A flock of nanophosphors (average 30 nm in size) was aggregated to form large spherical particles with a wide particle size distribution (~ 70 nm to ~ 30 µm). The nanophosphors, calculated by the Rietveld refinement method, grew linearly from 27 nm at 900 °C to 114 nm at 1300 °C. These calculated sizes are in good agreement with that measured in the electron micrograph images. The surface area of the particles decreased from 40 m²/g at 900 °C to 5 m²/g at 1300 °C due to the coagulation and growth of the nanophosphors. This process is a promising method

for forming large nanophosphors (~ 100 nm in size) in single crystal with a controlled spherical shape even after calcination at a very high temperature (1300 °C).

5.2 Synthesis of YAG: Ce³⁺ nanophosphors via solvothermal method

A novel nonhydrolytic solvothermal synthesis method has successfully resolved the problem associated with the crystallization of the nanophosphors with a pure garnet phase as synthesized.

Nanophosphors with a 5 nm size were synthesized via the thermal decomposition of the metal carbonates-oleate complex solution in the autoclave at a relatively low temperature of 300 °C for 6 days. The nucleation of the nanophosphors was mediated by oleic acid and their formation was facilitated by oleylamine (capping agent) which inhibited the crystal growth. The nanophosphors were capped by organic shells containing a mixture of oleylamine and oleic acid as revealed by the FT-IR analysis. As a result, the nanophosphors were uniformed and well-dispersed in organic solvent media to form a transparent colloid. They showed little tendency toward aggregation, and were therefore, suitable for the study of size-dependent optical phenomena.

Nanophosphors with a 250 nm in size were synthesized via the solvothermal method and were crystallized with a pure garnet phase at a low temperature 250 °C for 9 days. The success of the process was due to the

utilization of the molecular alkoxides precursors. The formation of the nanophosphors was aided by the benzyl alcohol and further stabilized by TOPO and oleic acid. The results showed that the morphology of the nanophosphors was near cubic shape. This could be attributed to sufficient thermal energy and long solvothermal durations that drive the crystal growth to its thermodynamic equilibrium phase and stable shape. A study into the role of dopants play in the formation of the nanophosphors revealed that cerium ions facilitated the crystallization process by minimizing the surface energy so that the nanophosphors with cubic shape were formed.

5.3 The size-dependent optical properties of YAG: Ce³⁺

The findings on the size-dependence of the optical property showed that the the Stokes shift was decreased and the optical spectra energy was blueshifted with decreasing particle sizes. This phenomenon could be explained through the nature of the nanostructure that restricts the expansion of Ce³⁺ upon excitation. A small degree of covalency upon excitation and a weak electron-phonon interaction cause the optical response shifts to higher energy, since the overlap between the electronic wavefunctions of Ce³⁺ and ligands is weak.

The poor luminescence efficiency observed in the nanophosphors (with 250 nm and 30 nm in sizes) was ascribed to the surface defects. These defective centers were determined by HRTEM to be incomplete garnet lattices and nonbridging oxygens, which acted as different host materials and in turn, trapped the electrons and quenched the cerium emission. The 5 nm nanophosphors, on the

other hand, showed an increased in the luminescence efficiency relative to other larger nanophosphors, implying that the organic shell has eliminated the surface defects and enhanced the efficiency.

A good agreement between the multimode Brownian oscillator model and measurements indicates a successful application of the theory based upon linear coupling of electron-phonon interactions and the Markovian dissipation of the thermal bath to explain the observed emission broad band of YAG: Ce³⁺. The coupling strength characterized by the Huang-Rhys factor (S) decreases with the reduction in the particle sizes.

5.4 Recommendations for future work

Future work could be to study the temperature-dependence of the optical properties of YAG: Ce³⁺ nanophosphors through the time-resolved spectroscopy (using femtosecond lasers). The study would include investigations of the luminescence decay dynamics at low temperatures. The femtosecond pulse durations and down-to-one-hertz bandwidth resolutions would be applied to probe on the vibrational dynamics and excitation relaxation. For example, it would be possible to observe a coherent phonon wave packet oscillating along an adiabatic potential surface associated with a self-trapped exciton in a crystal with strong exciton-phonon interactions. In parallel, theoretical modeling could be developed to better understand the underlying photophysics that governs those processes. For instance, polaronic wave functions could be used to model ultrafast electron-phonon dynamics.

Another future work could be to study the size effects on the energy transfer between the sensitizer and activator in the nanophosphors. This would address the problem of insufficient understanding of the characteristics of the sensitizer in a nanoscale phosphor. One possible direction is through studying the cerium and europium ion codoped in terbium aluminium garnet. Here, the cerium ion is a sensitizer that responsible for transferring the energy via the terbium sublattice to the europium ion [210]. The study would include the investigation of the energy transfer efficiency through the time-resolved spectroscopy. In addition, the luminescence efficiency of this nanophosphor (that depends on the sensitization of the cerium ion) would be compared with the one by direct activation of the cerium ion.

The study of the nanoscale's optical phenomenon could be further extended to couple the nanophosphors with the inverse photonic crystals. This is important because it would provide a basis for all solid-state dynamic control of optical quantum systems, and it would demonstrate the quantum coherency of the coupled material that has a potential for applications as efficient light sources and photon harvesting in condensed matter. For example, this coupled material system is significant for use in white LEDs lamps as the nanophosphors would experience a change in the emission decay rates and the photonic crystal would inhibit the undesirable scattered radiation, confine and guide the radiation from both the nanophosphors and LED, so that the photons are extracted and radiated omnidirectionally.

References

1. Shionoya, S. & Yen, W. M. (1999). *Phosphor handbook*. Boca Raton: CRC Press.
2. Blasse, G. & Grabmaier, B. C. (1994). *Luminescent materials*. Berlin: Springer-Verlag.
3. Kingery, W. D., Bowen, H. K., & Uhlmann, D. R. (1976). *Introduction to ceramics*. New York: John Wiley & Sons.
4. Luo, J., Han, L., Kariuki, N. N., Wang, L., Mott, D., Zhong, C.-J., & He, T. (2005). Synthesis and characterization of monolayer-capped PtVFe nanoparticles with controllable sizes and composition. *Chemistry of Materials*, 17, 5282-5290.
5. Niederberger, M., Garnweitner, G., Pinna, N., & Antonietti, M. (2004). Nonaqueous and Halide-Free Route to Crystalline BaTiO₃, SrTiO₃, and (Ba,Sr)TiO₃ Nanoparticles via a Mechanism Involving C-C Bond Formation. *J. Am. Chem. Soc.*, 126, 9120-9126.
6. Rodic, D., Mitric, M., Tellgren, R., & Rundlof, H. (2001). The cation distribution and magnetic structure of Y₃Fe_{5-x}Al_xO₁₂. *Journal of Magnetism and Magnetic Materials*, 232, 1-8.
7. Burda, C., Chen, X., Narayanan, R., & El-Sayed, M. A. (2005). Chemistry and properties of nanocrystals of different shapes. *Chemical Reviews*, 105, 1025-1102.
8. Hebbink, G. A., Stouwdam, J. W., Reinhoudt, D. N., & van Veggel, F. C. J. M. (2002). Lanthanide(III)-Doped Nanoparticles That Emit in the Near-Infrared. *Advanced Materials*, 14, 1147-1150.
9. Schuetz, P. & Caruso, F. (2002). Electrostatically Assembled Fluorescent Thin Films of Rare-Earth-Doped Lanthanum Phosphate Nanoparticles. *Chemistry of Materials*, 14, 4509-4516.
10. Riwozki, K., Meyssamy, H., Schnablegger, H., Kornowski, A., & Haase, M. (2001). Liquid-phase synthesis of colloids and redispersible powders of strongly luminescing LaPO₄:Ce,Tb nanocrystals. *Angewandte Chemie International Edition*, 40, 573-576.
11. Schmidt, T., Muller, G., Spanhel, L., Kerkel, K., & Forchel, A. (1998). Activation of 1.54μm Er³⁺ Fluorescence in Concentrated II-VI Semiconductor Cluster Environments. *Chemistry of Materials*, 10, 65-71.

12. Lim, J., Jun, S., Jang, E., Baik, H., Kim, H., & Cho, J. (2007). Preparation of highly luminescent nanocrystals and their application to light-emitting diodes. *Advanced Materials*, 19, 1927-1932.
13. Tsao, J. Y., *Light emitting diodes (LEDs) for general illumination: An OIDA Technology Roadmap update 2002*. 2002, Optoelectronic Industry Development Association.
14. Bergh, A., Craford, G., Duggal, A., & Haitz, R. 2001. *Physics Today*, 54.
15. Mueller, G. O. & Mueller-Mach, R. *Set the pace in white space-white LEDs for illumination and backlighting*. in *Global Phosphor Summit*. 2005. San Diego, USA.
16. Li, Z. & Zhang, Y. (2006). Monodisperse silica-coated polyvinylpyrrolidone/NaYF₄ Nanocrystals with multicolor upconversion fluorescence emission. *Angewandte Chemie International Edition*, 45, 7732-7735.
17. Nichkova, M., Dosev, D., Gee, S. J., Hammock, B. D., & Kennedy, I. M. (2005). Microarray Immunoassay for Phenoxybenzoic Acid Using Polymer Encapsulated Eu:Gd₂O₃ Nanoparticles as Fluorescent Labels. *Anal. Chem.*, 77, 6864-6873.
18. Vaisanen, V., Harma, H., Lilja, H., & Bjartell, A. (2000). Time-resolved fluorescence imaging for quantitative histochemistry using lanthanide chelates in nanoparticles and conjugated to monoclonal antibodies. *Luminescence*, 15, 389-397.
19. Beaurepaire, E., Buissette, V., Sauviat, M.-P., Giaume, D., Lahlil, K., Mercuri, A., Casanova, D., Huignard, A., Martin, J.-L., Gacoin, T., Boilot, J.-P., & Alexandrou, A. (2004). Functionalized Fluorescent Oxide Nanoparticles: Artificial Toxins for Sodium Channel Targeting and Imaging at the Single-Molecule Level. *Nano Lett.*, 4, 2079-2083.
20. Chen, Y., Chi, Y., Wen, H., & Lu, Z. (2007). Sensitized Luminescent Terbium Nanoparticles: Preparation and Time-Resolved Fluorescence Assay for DNA. *Anal. Chem.*, 79, 960-965.
21. Shalav, A., Richards, B. S., & Green, M. A. (2007). Luminescent layers for enhanced silicon solar cell performance: Up-conversion. *Solar Energy Materials and Solar Cells*, 91, 829-842.
22. Boyer, J.-C., Cuccia, L. A., & Capobianco, J. A. (2007). Synthesis of Colloidal Upconverting NaYF₄: Er³⁺/Yb³⁺ and Tm³⁺/Yb³⁺ Monodisperse Nanocrystals. *Nano Letters*, 7, 847-852.
23. Boyer, J.-C., Vetrone, F., Cuccia, L. A., & Capobianco, J. A. (2006). Synthesis of colloidal upconverting NaYF₄ nanocrystals doped with Er³⁺, Yb³⁺ and Tm³⁺, Yb³⁺ via Thermal Decomposition of lanthanide

- Trifluoroacetate precursors. *Journal of the American Chemical Society*, 128, 7444-7445.
24. Suyver, J. F., Aebischer, A., Biner, D., Gerner, P., Grimm, J., Heer, S., Kramer, K. W., Reinhard, C., & Gudel, H. U. (2005). Novel materials doped with trivalent lanthanides and transition metal ions showing near-infrared to visible photon upconversion. *Optical Materials*, 27, 1111-1130.
 25. Heer, S., Kompe, K., Gudel, H.-U., & Haase, M. (2004). Highly efficient multicolour upconversion emission in transparent colloids of lanthanide-doped NaYF₄ nanocrystals. *Advanced Materials*, 16, 2102-2105.
 26. Shalav, A., Richards, B. S., Trupke, T., Kramer, K. W., & Gudel, H. U. (2005). Application of NaYF₄:Er³⁺ up-converting phosphors for enhanced near-infrared silicon solar cell response. *Applied Physics Letters*, 86, 013505.
 27. Xu, Y.-N. & Ching, W. Y. (1999). Electronic structure of yttrium aluminum garnet (Y₃Al₅O₁₂). *Physical Review B*, 59, 10530 -10535.
 28. Powell, R. C. (1998). *Physics of solid state laser materials*. New York: AIP.
 29. French, J. D., Zhao, J., Harmer, M. P., Chan, H. M., & Miller, G. A. (1994). *Journal of the American Ceramic Society*, 77, 2857.
 30. Wuister, S. F., Mello Donega, C. d., & Meijerink, A. (2004). Efficient energy transfer between nanocrystalline YAG:Ce and TRITC. *Physical Chemistry Chemical Physics*, 6, 1633-1636.
 31. Blasse, G. & Bril, A. (1967). A new phosphor for flying-spot cathode-ray tubes for color television: yellow-emitting Y₃Al₅O₁₂-Ce³⁺. *Applied Physics Letter*, 11, 53-54.
 32. Bril, A. & Klasens, H. A. (1952). *Philips Res. Rept.*, 7, 421.
 33. Gilliland, J. W. & Hall, M. S. (1966). *Electrochem. Tech.*, 4, 378.
 34. Ropp, R. C. (1993). *The chemistry of artificial lighting devices-lamps, phosphors and cathode ray tubes*. Studies in Inorganic Chemistry. Vol. 17. Amsterdam: Elsevier Science Publishers B.V.
 35. Narita, K. (1998). Methods of phosphor synthesis and related technology. In S. Shionoya & W.M. Yen (Eds.), *Phosphor handbook*. Boca Raton: CRC Press.
 36. Wang, H., Gao, L., & Niihara, K. (2000). Synthesis of nanoscaled yttrium aluminum garnet powder by the co-precipitation method. *Materials Science and Engineering A*, 288, 1-4.

37. Chen, T.-M., Chen, S. C., & Yu, C.-J. (1999). Preparation and characterization of garnet phosphor nanoparticles derived from oxalate coprecipitation. *Journal of Solid State Chemistry*, 144, 437-441.
38. Iida, Y., Towata, A., Tsugoshi, T., & Furukawa, M. (1999). In situ Raman monitoring of low-temperature synthesis of YAG from different starting materials. *Vibrational Spectroscopy*, 19, 399-405.
39. Palmero, P., Esnouf, C., Montanaro, L., & Fantozzi, G. (2005). Influence of the co-precipitation temperature on phase evolution in yttrium-aluminium oxide materials. *Journal of the European Ceramic Society*, 25, 1565-1578.
40. Vaqueiro, P., Lopez-Quintela, M. A., & Rivas, J. (1997). Synthesis of yttrium iron garnet nanoparticles via coprecipitation in microemulsion. *Journal of Materials Chemistry*, 7, 501-504.
41. Taketomi, S., Dai, Z. R., & Ohuchi, F. S. (2000). Electron diffraction of yttrium iron oxide nanocrystals prepared by the alkoxide method. *Journal of Magnetism and Magnetic Materials*, 217, 5-13.
42. Veith, M., Mathur, S., Kareiva, A., Jilavi, M., Zimmer, M., & Huch, V. (1999). Low temperature synthesis of noncrystalline $\text{Y}_3\text{Al}_5\text{O}_{12}$ (YAG) and Ce-doped $\text{Y}_3\text{Al}_5\text{O}_{12}$ via different sol-gel methods. *Journal of Materials Chemistry*, 9, 3069-3079.
43. Li, X., Liu, H., Wang, J., Cui, H., & Han, F. (2004). Production of nanosized YAG powders with spherical morphology and nonaggregation via a solvothermal method. *Journal of the American Ceramic Society*, 87, 2288-2290.
44. Kasuya, R., Isobe, T., Kuma, H., & Katano, J. (2005). Photoluminescence enhancement of PEG-modified $\text{YAG}:\text{Ce}^{3+}$ nanocrystal phosphor prepared by glycothermal method. *Journal of physical chemistry B*, 109, 22126-22130.
45. Takamori, T. & David, L. D. (1986). Controlled nucleation for hydrothermal growth of yttrium aluminium garnet powders. *Americical Ceramic Society Bulletin*, 65, 1282-1286.
46. Hakuta, Y., Seino, K., Haruo, U., Adschiri, T., Takizawa, H., & Arai, K. (1999). Production of phosphor (YAG:Tb) fine particles by hydrothermal synthesis in supercritical water. *Journal of Materials Chemistry*, 9, 2671-2674.
47. Inoue, M., Otsu, H., Kominami, H., & Inui, T. (1991). Synthesis of yttrium aluminium garnet by the glycothermal method. *Journal of the American Ceramic Society*, 74, 1452-1454.
48. Inoue, M., Nishikawa, T., & Inui, T. (1998). Reactions of rare earth acetates with aluminium isopropoxide in ethylene glycol: Synthesis of the

- garnet and monoclinic phases of rare earth aluminates. *Journal of Materials Science*, 33, 5835-5841.
49. Feldmann, C. (2003). Polyol-mediated synthesis of nanoscale functional materials. *Advanced Functional Materials*, 13, 101-107.
 50. Lu, C. H., Hong, H. C., & Jagannathan, R. (2002). Luminescent $\text{Y}_3\text{Al}_5\text{O}_{12}:\text{Ce}^{3+}$ nanoparticles-low temperature sol-gel synthesis and critical preparative parameters. *Journal of Materials Science Letters*, 21, 1489-1492.
 51. Lu, C. H. & Jagannathan, R. (2002). Cerium-ion-doped yttrium aluminium garnet nanophosphors prepared through sol-gel pyrolysis for luminescent lighting. *Applied Physics Letters*, 80, 3608-3610.
 52. Lu, C. H., Hsu, W. T., Dhanaraj, J., & Jagannathan, R. (2004). Sol-gel pyrolysis and photoluminescent characteristics of europium-ion doped yttrium aluminum garnet nanophosphors. *Journal of the European Ceramic Society*, 24, 3723-3729.
 53. Liu, X. J., Li, H. L., Xie, R. J., Hirosaki, N., Xu, X., & Huang, L. P. (2006). Cerium-doped lutetium aluminum garnet optically transparent ceramics fabricated by a sol-gel combustion process. *Journal of Materials Research*, 21, 1519-1525.
 54. Haranath, D., Chander, H., Sharma, P., & Singh, S. (2006). Enhanced luminescence of $\text{Y}_3\text{Al}_5\text{O}_{12}:\text{Ce}^{3+}$ nanophosphor for white light-emitting diodes. *Applied Physics Letters*, 89, 173118.
 55. Adair, J. H., Li, T., Kido, T., Havey, K., Moon, J., Mecholsky, J., Morrone, A., Talham, D. R., Ludwig, M. H., & Wang, L. (1998). Recent developments in the preparation and properties of nanometer-size spherical and platelet-shaped particles and composite particles. *Materials Science and Engineering: R: Reports*, 23, 139-242.
 56. Chander, H. (2005). Development of nanophosphors--A review. *Materials Science and Engineering: R: Reports*, 49, 113-155.
 57. Roduner, E. (2006). *Nanoscale materials: size-dependent phenomena*. Cambridge: RSC Publishing.
 58. Wikander, K., Petit, C., Holmberg, K., & Pileni, M.-P. (2006). Size control and growth process of alkylamine-stabilised platinum nanocrystals: A comparison between the phase transfer and reverse micelles methods. *Langmuir*, 22, 4863-4868.
 59. Chimentao, R. J., Cota, I., Dafinov, A., Medina, F., & Sueiras, J. E. (2006). Synthesis of silver-gold nanoparticles by a phase-transfer system. *Journal of Materials Research*, 21, 105-111.

60. Rajamathi, M., Ghosh, M., & Seshadri, R. (2002). Hydrolysis and amine-capping in a glycol solvent as a route to soluble maghemite $\gamma\text{-Fe}_2\text{O}_3$ nanoparticles. *Chemical Communications*, 1152-1153.
61. Yu, J. H., Joo, J., Park, H. M., Baik, S.-I., Kim, Y. W., Kim, S. C., & Hyeon, T. (2005). Synthesis of Quantum-Sized Cubic ZnS Nanorods by the Oriented Attachment Mechanism. *J. Am. Chem. Soc.*, 127, 5662-5670.
62. Sun, S. & Zeng, H. (2002). Size-controlled synthesis of magnetite nanoparticles. *Journal of the American Chemical Society*, 124, 8204-8205.
63. Park, J., An, K., Hwang, Y., Park, J.-g., Noh, H.-j., Kim, J.-y., Park, J.-h., Hwang, N.-m., & Hyeon, T. (2004). Ultra-large-scale syntheses of monodisperse nanocrystals. *Nature Materials*, 3, 891-895.
64. Shi, W., Zeng, H., Sahoo, Y., Ohulchanskyy, T. Y., Yong, D., Wang, Z. L., Swihart, M., & Prasad, P. N. (2006). A general approach to binary and ternary hybrid nanocrystals. *Nano Letters*, 6, 875-881.
65. O'Brien, S., Brus, L., & Murray, C. B. (2001). Synthesis of monodisperse nanoparticles of barium titanate: toward a generalized strategy of oxide nanoparticle synthesis. *Journal of the American Chemical Society*, 123, 12085-12086.
66. Wang, H., Uehara, M., Nakamura, H., Miyazaki, M., & Maeda, H. (2005). Synthesis of well-dispersed $\text{Y}_2\text{O}_3\text{:Eu}$ nanocrystals and self-assembled nanodisks using a simple non-hydrolytic route. *Advanced Materials*, 17, 2506-2509.
67. Wang, L. & Li, Y. (2006). $\text{Na}(\text{Y}_{1.5}\text{Na}_{0.5})\text{F}_6$ single-crystal nanorods as multicolor luminescent materials. *Nano Letters*, 6, 1645-1649.
68. Trentler, T. J., Denler, T. E., Bertone, J. F., Agrawal, A., & Colvin, V. L. (1999). Synthesis of TiO_2 nanocrystals by nonhydrolytic solution-based reactions. *Journal of the American Chemical Society*, 121, 1613-1614.
69. Mekis, I., Talapin, D. V., Kornowski, A., Haase, M., & Weller, H. (2003). One-Pot Synthesis of Highly Luminescent CdSe/CdS Core-Shell Nanocrystals via Organometallic and "Greener" Chemical Approaches. *J. Phys. Chem. B*, 107, 7454-7462.
70. Talapin, D. V., Rogach, A. L., Kornowski, A., Haase, M., & Weller, H. (2001). Highly luminescent monodisperse CdSe and CdSe/ZnS nanocrystals synthesized in a hexadecylamine-trioctylphosphine oxide-trioctylphosphine mixture. *Nano Letters*, 1, 207-211.
71. Pang, Q., Zhao, L., Cai, Y., Nguyen, D. P., Regnault, N., Wang, N., Yang, S., Ge, W., Ferreira, R., Bastard, G., & Wang, J. (2005). CdSe nanotetrapods: controllable synthesis, structure analysis, and electronic and optical properties. *Chemistry of Materials*, 17, 5263-5267.

72. Chaubey, G. S., Barcena, C., Poudyal, N., Rong, C., Gao, J., Sun, S., & Liu, J. P. (2007). Synthesis and Stabilization of FeCo Nanoparticles. *J. Am. Chem. Soc.*, 129, 7214-7215.
73. Niederberger, M., Bartl, M. H., & Stucky, G. D. (2002). Benzyl alcohol and titanium tetrachloride-a versatile reaction system for the nonaqueous and low temperature preparation of crystalline and luminescent titania nanoparticles. *Chemistry of Materials*, 14, 4364-4370.
74. Niederberger, M., Bartl, M. H., & Stucky, G. D. (2002). Benzyl alcohol and transition metal chlorides as a versatile reaction system for the nonaqueous and low-temperature synthesis of crystalline nano-objects with controlled dimensionality. *Journal of the American Chemical Society*, 124, 13642-13643.
75. Niederberger, M., Pinna, N., Polleux, J., & Antonietti, M. (2004). A general soft-chemistry route to perovskites and related materials: synthesis of BaTiO₃, BaZrO₃, and LiNbO₃ nanoparticles. *Angewandte Chemie International Edition*, 43, 2270-2273.
76. Pinna, N., Garnweitner, G., Antonietti, M., & Niederberger, M. (2004). Non-aqueous synthesis of high-purity metal oxide nanopowders using an ether elimination process. *Advanced Materials*, 16, 2196-2200.
77. Pinna, N., Neri, G., Antonietti, M., & Niederberger, M. (2004). Nonaqueous synthesis of nanocrystalline semiconducting metal oxides for gas sensing. *Angewandte Chemie International Edition*, 43, 4345-4349.
78. Niederberger, M., Garnweitner, G., Pinna, N., & Neri, G. (2005). Non-aqueous routes to crystalline metal oxide nanoparticles: Formation mechanisms and applications. *Progress in Solid State Chemistry*, 33, 59-70.
79. Ba, J., Rohlfing, D. F., Feldhoff, A., Brezesinski, T., Djerdj, I., Wark, M., & Niederberger, M. (2006). Nonaqueous Synthesis of Uniform Indium Tin Oxide Nanocrystals and Their Electrical Conductivity in Dependence of the Tin Oxide Concentration. *Chemistry of Materials*, 18, 2848-2854.
80. Chen, S. & Kimura, K. (1999). Synthesis and Characterization of Carboxylate-Modified Gold Nanoparticle Powders Dispersible in Water. *Langmuir*, 15, 1075-1082.
81. Alivisatos, A. P. (1996). Semiconductor clusters, nanocrystals, and quantum dots. *Science*, 271, 933-937.
82. Nirmal, M. & Brus, L. (1999). Luminescence Photophysics in Semiconductor Nanocrystals. *Acc. Chem. Res.*, 32, 407-414.
83. Masumoto, Y. & Takagahara, T. (2002). *Semiconductor quantum dots: physics, spectroscopy and applications*. Berlin: Springer-Verlag.

84. Pedrini, C., Rogemond, F., & McClure, D. S. (1986). Photoionization thresholds of rare-earth impurity ions. $\text{Eu}^{2+}:\text{CaF}_2$, $\text{Ce}^{3+}:\text{YAG}$, and $\text{Sm}^{2+}:\text{CaF}_2$. *Journal of Applied Physics*, 59, 1196.
85. Slack, G. A., Oliver, D. W., Chrenko, R. M., & Roberts, S. (1969). Optical Absorption of $\text{Y}_3\text{Al}_5\text{O}_{12}$ from 10- to 55 000 cm^{-1} Wave Numbers. *Physical Review*, 177, 1308 -1314.
86. Hamilton, D. S., Gayen, S. K., Pogatshnik, G. J., Ghen, R. D., & Miniscalco, W. J. (1989). Optical-absorption and photoionization measurements from the excited states of $\text{Ce}^{3+}:\text{Y}_3\text{Al}_5\text{O}_{12}$. *Physical Review B*, 39, 8807 LP - 8815.
87. Blasse, G. & Bril, A. (1967). Investigation of some Ce^{3+} -Activated Phosphors. *The Journal of chemical physics*, 47, 5139-5145.
88. Miniscalco, W. J., Pellegrino, J. M., & Yen, W. M. (1978). Measurements of excited-state absorption in $\text{Ce}^{3+}:\text{YAG}$. *Journal of Applied Physics*, 49, 6109-6111.
89. Jacobs, R. R., Krupke, W. F., & Weber, M. J. (1978). Measurement of excited-state-absorption loss for Ce^{3+} in $\text{Y}_3\text{Al}_5\text{O}_{12}$ and implications for tunable 5d->4f rare-earth lasers. *Applied Physics Letters*, 33, 410-412.
90. Wong, C. M., Rotman, S. R., & Warde, C. (1984). Optical studies of cerium doped yttrium aluminium garnet single crystals. *Applied Physics Letters*, 44, 1038-1040.
91. Tomiki, T., Akamine, H., Gushiken, M., Kinjoh, Y., Miyazato, M., Miyazato, T., Toyokawa, N., Hiraoka, M., Hirata, N., Ganaha, Y., & Futemma, T. (1991). Ce^{3+} centres in $\text{Y}_3\text{Al}_5\text{O}_{12}$ (YAG) single crystals. *Journal of the physical society of japan*, 60, 2437-2445.
92. Tanner, P. A., Fu, L., Ning, L., Cheng, B.-M., & Brik, M. G. (2007). Soft synthesis and vacuum ultraviolet spectra of $\text{YAG}:\text{Ce}^{3+}$ nanocrystals:reassignment of Ce^{3+} energy levels. *Journal of Physics: Condensed Matter*, 19, 216213.
93. Franck, J. (1926). Elementary processes of photochemical reactions. *Transactions of the Faraday Society*, 21, 536.
94. Garsia, S. J., Bausa, L. E., & Jaque, D. (2005). *An introduction to the optical spectroscopy of inorganic solids*. West Sussex: John Wiley & Sons, Ltd.
95. Svelto, O. (1986). *Principles of Lasers*. New York: Plenum Press.
96. Yamamoto, H. *The basics of phosphor technology*. in *Phosphor Global Summit*. 2005. San Diego, California, US.
97. Sabbatini, N. & Blasse, G. (1988). Luminescence of lanthanide cryptates. *Journal of Luminescence*, 40-41, 288-289.

98. von Zelewsky, A. (1995). *Stereochemistry of Coordination Compounds*. Chichester: John Wiley.
99. Cheng, H. M., Lin, K. F., Hsu, H. C., & Hsieh, W. F. (2006). Size dependence of photoluminescence and resonant Raman scattering from ZnO quantum dots. *Applied Physics Letters*, 88, 261909.
100. Igarashi, T., Ihara, M., Kusunoki, T., Ohno, K., Isobe, T., & Senna, M. (2000). Relationship between optical properties and crystallinity of nanometer Y₂O₃:Eu phosphor. *Applied Physics Letters*, 76, 1549-1551.
101. Jose, G., Amrutha, K. A., Toney, T. F., Thomas, V., Joseph, C., Ittyachen, M. A., & Unnikrishnan, N. V. (2006). Structural and optical characterization of Eu³⁺/CdSe nanocrystal containing silica glass. *Materials Chemistry and Physics*, 96, 381-387.
102. Vink, A. P. & Meijerink, A. (2000). Electron-phonon coupling of Cr³⁺ in YAG and YGG. *Journal of Luminescence*, 87-89, 601-604.
103. Ernsting, N. P., Kaschke, M., Weller, H., & Katsikas, L. (1990). Colloidal Zn_{1-x}Cd_xS: optical saturation of the exciton band and primary photochemistry studied by subpicosecond laser flash photolysis. *Journal of the Optical Society of America B*, 7, 1630.
104. Chowdhury, P. S., Saha, S., & Patra, A. (2004). Influence of nanoenvironment on luminescence of Eu³⁺ activated SnO₂ nanocrystals. *Solid State Communications*, 131, 785-788.
105. Xiong, G., Pal, U., & Garcia Serrano, J. (2007). Correlations among size, defects, and photoluminescence in ZnO nanoparticles. *Journal of Applied Physics*, 101, 024317.
106. Zhang, J. Z. (1997). Ultrafast Studies of Electron Dynamics in Semiconductor and Metal Colloidal Nanoparticles: Effects of Size and Surface. *Acc. Chem. Res.*, 30, 423-429.
107. Pan, L. K. & Sun, C. Q. (2004). Coordination imperfection enhanced electron-phonon interaction. *Journal of Applied Physics*, 95, 3819-3821.
108. Sadhu, S., Chowdhury, P. S., & Patra, A. (2007). Understanding the role of particle size on photophysical properties of CdS:Eu³⁺ nanocrystals. *Journal of Luminescence*, 126, 387-392.
109. Lehmann, O., Kompe, K., & Haase, M. (2004). Synthesis of Eu³⁺-Doped Core and core/shell nanoparticles and direct spectroscopic identification of dopant sites at the surface and in the interior of the particles. *Journal of the American Chemical Society*, 126, 14935-14942.
110. Karar, N. & Chander, H. (2005). Luminescence properties of cerium doped nanocrystalline yttrium silicate. *Journal of Physics D: Applied Physics*, 38, 3580-3583.

111. Chen, W., Malm, J. O., Zwiller, V., Wallenberg, R., & Bovin, J. O. (2001). Size dependence of Eu^{2+} fluorescence in $\text{ZnS}:\text{Eu}^{2+}$ nanoparticles. *Journal of Applied Physics*, 89, 2671-2675.
112. Zhao, Y., Zanardi, P., & Chen, G. (2004). Quantum entanglement and the self-trapping transition in polaronic systems. *Phys. Rev. B*, 70, 195113.
113. Munn, R. W. & Silbey, R. (1985). *J. Chem. Phys.*, 83, 1843.
114. Zhao, Y., Brown, D. W., & Lindenberg, K. (1994). *J. Chem. Phys.*, 100, 2335.
115. Holstein, T. (1959). *Ann. Phys. (N.Y.)*, 8, 325.
116. Takagahara, T. (1996). Electron-phonon interactions in semiconductor nanocrystals. *Journal of Luminescence*, 70, 129-143.
117. Sivasubramanian, V., Arora, A. K., Premila, M., Sundar, C. S., & Sastry, V. S. (2006). Optical properties of CdS nanoparticles upon annealing. *Physica E: Low-dimensional Systems and Nanostructures*, 31, 93-98.
118. Sun, H. D., Makino, T., Tuan, N. T., Segawa, Y., Kawasaki, M., Ohtomo, A., Tamura, K., & Koinuma, H. (2001). Temperature dependence of excitonic absorption spectra in $\text{ZnO}/\text{Zn}_{0.88}\text{Mg}_{0.12}\text{O}$ multiquantum wells grown on lattice-matched substrates. *Applied Physics Letters*, 78, 2464-2466.
119. McCumber, D. E. & Sturge, M. D. (1963). Linewidth and Temperature Shift of the R Lines in Ruby. *Journal of Applied Physics*, 34, 1682-1684.
120. Mukamel, S. (1995). *Principles of nonlinear optical spectroscopy*. Rochester, New York: Oxford University Press, Inc.
121. Zhao, Y. & Knox, R. S. (2000). A Brownian Oscillator Approach to the Kennard-Stepanov relation. *Journal of physical chemistry A*, 104, 7751-7761.
122. Hu, L., Zhao, Y., Wang, F., Chen, G., Ma, C., Kwok, W.-M., & Phillips, D. L. (2007). Are adenine strands helical H-aggregates? *Journal of physical chemistry B*, 111, 11812-11816.
123. Shi, S. L., Li, G. Q., Xu, S. J., Zhao, Y., & Chen, G. H. (2006). Green luminescence band in ZnO: Fine Structures, electron-phonon coupling, and temperature effect. *Journal of physical chemistry B*, 110, 10475-10478.
124. Xu, S. J., Li, G. Q., Wang, Y. J., Zhao, Y., Chen, G. H., Zhao, D. G., Zhu, J. J., Yang, H., Yu, D. P., & Wang, J. N. (2006). Quantum dissipation and broadening mechanisms due to electron-phonon interactions in self-formed InGaN quantum dots. *Applied Physics Letters*, 88, 083123.
125. Lax, M. (1952). The Franck-Condon Principle and Its Application to Crystals. *The Journal of Chemical Physics*, 20, 1752.

126. Kubo, R. (1954). Note on the Stochastic Theory of Resonance Absorption. *Journal of the Physical Society of Japan*, 9, 935.
127. Kubo, R. (1962). In D. TerHaar (Eds.), *Fluctuation, relaxation and resonance in magnetic systems* (pp. 23). Edinburg and London: Oliver & Boyd.
128. Weiss, U. (1993). *Quantum dissipative systems*. Singapore: World scientific.
129. Grabert, H., Schramm, P., & Ingold, G. L. (1988). *Phys. Rep.*, 168, 115.
130. Chernyak, V. & Mukamel, S. (1996). *J. Chem. Phys.*, 105, 4565.
131. Voort, D. v. d. (2005, Jan). "Ce₂O₃ content in U728 powder." E-mail to the author.
132. Stadelmann, P. A. (1987). EMS - a software package for electron diffraction analysis and HREM image simulation in materials science. *Ultramicroscopy*, 21, 131-145.
133. Hovmoller, S. (1992). CRISP: crystallographic image processing on a personal computer. *Ultramicroscopy*, 41, 121-135.
134. Zou, X., Sundberg, M., Larine, M., & Hovmoller, S. (1996). Structure projection retrieval by image processing of HREM images taken under non-optimum defocus conditions. *Ultramicroscopy*, 62, 103-121.
135. Cheary, R. W. & Coelho, A. (1992). A fundamental parameters approach to x-ray line-profile fitting. *Journal of Applied Crystallography*, 25, 109-121.
136. TOPAS (2003). *User's Manual, Bruker Advanced X-ray Solutions*. Karlsruhe: Bruker AXS GmbH, Germany.
137. Fairley, N. & Carrick, A., *The Casa Cookbook, Part I*. 2005, Acolyte science.
138. Wagner, C. D., Riggs, W. M., Davis, L. E., Moulder, J. F., & Muilenberg, G. E. (1979). *Handbook of X-ray photoelectron spectroscopy*: Perkin-Elmer Corporation, Physical Electronics Division.
139. Demas, J. N. & Crosby, G. A. (1971). The measurement of photoluminescence quantum yields. A review. *The Journal of physical chemistry*, 75, 991-1024.
140. Fischer, M. & Georges, J. (1996). Fluorescence quantum yield of rhodamine 6G in ethanol as a function of concentration using thermal lens spectrometry. *Chemical Physics Letters*, 260, 115-118.
141. Kubin, R. F. & Fletcher, A. N. (1983). Fluorescence quantum yields of some rhodamine dyes. *Journal of Luminescence*, 27, 455-462.

142. Huang, K. & Rhys, A. (1950). Theory of Light Absorption and Non-Radiative Transitions in F-Centres. *Proceedings of the Royal Society of London. Series A, Mathematical and Physical Sciences*, 204, 406-423.
143. Matsushita, N., Tsuchiya, N., & Nakatsuka, K. (1999). Precipitation and calcinations processes for yttrium aluminium garnet precursors synthesized by the urea method. *Journal of the American Ceramic Society*, 82, 1977-1984.
144. Li, X., Liu, H., Wang, J., Cui, H., Zhang, X., & Han, F. (2004). Preparation of YAG:Nd nano-sized powder by co-precipitation method. *Material Science and Engineering*, A379, 347-350.
145. Ramanathan, S., Kakade, M. B., Roy, S. K., & Kutty, K. K. (2003). Processing and characterization of combustion synthesized YAG powders. *Ceramics International*, 29, 477-484.
146. Nyman, M., Caruso, J., & Hampden-Smith, M. J. (1997). Comparison of solid-state and spray-pyrolysis synthesis of yttrium aluminate powders. *Journal of The American Ceramic Society*, 80, 1231-1238.
147. Kong, L. B., Ma, J., & Huang, H. (2002). Low temperature formation of yttrium aluminium garnet from oxides via a high energy ball milling process. *Materials Letters*, 56, 344-348.
148. Hardy, A. B., Gowda, G., McMahon, T. J., Riman, R. E., Rhine, W. E., & Bowen, H. K. (1988). Preparation of Oxide Powders. In J.D. MacKenzie & D.R. Ulrich (Eds.), *Ultrastructure Processing of Advanced Ceramics* (pp. 407-428). John Wiley & Sons, Inc.
149. Paulik, F. (1995). *Special trends in thermal analysis*. Chicester: John Wiley & Sons Ltd.
150. Sim, S. M., Keller, K. A., & Mah, T. I. (2000). Phase formation in yttrium aluminium garnet powders synthesized by chemical methods. *Journal of Materials Science*, 35, 713-717.
151. Kinsman, K. M., Mckittrick, J., Sluzky, E., & Hesse, K. (1994). *Journal of the American Ceramic Society*, 77, 2866.
152. Apte, P., Burke, H., & Pickup, H. (1992). *Journal of Materials Research*, 7, 706.
153. Yamaguchi, O., Takeoka, K., & Hayashida, A. *Journal of Materials Science Letter*, 10, 101.
154. Hsu, W. T., Wu, W. H., & Lu, C. H. (2003). Synthesis and luminescent properties of nano-sized $\text{Y}_3\text{Al}_5\text{O}_{12}:\text{Eu}^{3+}$ phosphors. *Materials Science and Engineering*, B104, 40-44.
155. Chang, R. (2002). *Chemistry*. 7th ed. New York: McGraw-Hill.

156. Porter, M. R. (1991). *Handbook of surfactants*. London: Chapman & Hall.
157. Birdi, K. S. (2002). *Handbook of surface and colloid chemistry*. Boca Raton: CRC Press.
158. Su, L. T., Tok, A. I. Y., Boey, F. Y. C., Happy, Ng, S. H., & Psaras, D. *Synthesis and properties of spherical nanocrystalline $Y_2O_3:Eu^{3+}$* . in *Global Phosphors Summit 2005*. 2005. San Diego, USA.
159. Hahn, T. (1996). *International Crystallography Table*. Dordrecht: Kluwer Academic Publishers.
160. Jaffe, H. W. (1988). *Crystal chemistry and refractivity*. Cambridge: Cambridge University Press.
161. Cao, G. (2004). *Nanostructures and nanomaterials-synthesis, properties, and applications*. London: Imperial College Press.
162. de La Croix, A., English, R. B., Brown, M. E., & Glasser, L. (1998). Modeling the Thermal Decomposition of Solids on the Basis of Lattice Energy Changes: Part 1: Alkaline-Earth Carbonates. *Journal of Solid State Chemistry*, 137, 332-345.
163. Hussein, G. A. M. (1996). Rare earth metal oxides: formation, characterization and catalytic activity Thermoanalytical and applied pyrolysis review. *Journal of Analytical and Applied Pyrolysis*, 37, 111-149.
164. Croix, A. d. l., English, R. B., Brown, M. E., & Glasser, L. (1998). Modeling the Thermal Decomposition of Solids on the Basis of Lattice Energy Changes: Part 1: Alkaline-Earth Carbonates. *Journal of Solid State Chemistry*, 137, 332-345.
165. MacKenzie, K. J. D. & Kemmitt, T. (1999). Evolution of crystalline aluminates from hybrid gel-derived precursors studied by XRD and multinuclear solid-state MAS NMR: II. Yttrium-aluminium garnet, $Y_3Al_5O_{12}$. *Thermochimica Acta*, 325, 13-18.
166. Maye, M. M., Zheng, W., Leibowitz, F. L., Ly, N. K., & Zhong, C. J. (2000). Heating-Induced Evolution of Thiolate-Encapsulated Gold Nanoparticles: A Strategy for Size and Shape Manipulations. *Langmuir*, 16, 490-497.
167. Hostetler, M. J., Stokes, J. J., & Murray, R. W. (1996). Infrared Spectroscopy of Three-Dimensional Self-Assembled Monolayers: N-Alkanethiolate Monolayers on Gold Cluster Compounds. *Langmuir*, 12, 3604-3612.
168. Hostetler, M. J., Wingate, J. E., Zhong, C.-J., Harris, J. E., Vachet, R. W., Clark, M. R., Londono, J. D., Green, S. J., Stokes, J. J., Wignall, G. D., Glish, G. L., Porter, M. D., Evans, N. D., & Murray, R. W. (1998). Alkanethiolate Gold Cluster Molecules with Core Diameters from 1.5 to

- 5.2 nm: Core and Monolayer Properties as a Function of Core Size. *Langmuir*, 14, 17-30.
169. Nuzzo, R. G., Dubois, L. H., & Allara, D. L. (1990). Fundamental studies of microscopic wetting on organic surfaces. 1. Formation and structural characterization of a self-consistent series of polyfunctional organic monolayers. *J. Am. Chem. Soc.*, 112, 558-569.
 170. Walczak, M. M., Chung, C., Stole, S. M., Widrig, C. A., & Porter, M. D. (1991). Structure and interfacial properties of spontaneously adsorbed n-alkanethiolate monolayers on evaporated silver surfaces. *J. Am. Chem. Soc.*, 113, 2370-2378.
 171. Hay, R. S. (1993). Phase transformations and microstructure evolution in sol-gel derived yttrium-aluminium garnet films. *Journal of Materials Research*, 8, 578.
 172. Gowda, G. (1986). Synthesis of Yttrium Aluminates by the sol-gel process. *Journal of Materials Science Letters*, 5, 1029.
 173. Manalart, R. & Rahaman, M. N. (1996). Sol-gel processing and sintering of yttrium aluminum garnet (YAG) powders. *Journal of Materials Science*, 31, 3453-3458.
 174. Liu, Y., Zhang, Z. F., Halloran, J., King, B., & Laine, R. M. (1996). *Journal of the American Ceramic Society*, 79, 385.
 175. Messier, D. R. & Gazza, G. E. (1972). *Americical Ceramic Society Bulletin*, 51, 692.
 176. Hubert-Pfalzgraf, L. G., Poncelet, O., & Daran, J.-C. (1990). Tailored molecular precursors of yttrium oxide using functional alcohols and acetylacetone as modifiers. In B.J.J. Zelinski, et al. (Eds.), *Materials research society symposium proceedings-Better ceramics through chemistry IV*. Pittsburgh: Materials Research Society.
 177. Ji, L., Lin, J., Tan, K. L., & Zeng, H. C. (2000). Synthesis of high-surface-area alumina using aluminium tri-sec-butoxide-2,4-pentanedione-2-propanol-nitric acid precursors. *Chemistry of Materials*, 12, 931-939.
 178. Debsikdar, J. C. (1986). Transparent zirconia gel-monolith from zirconium alkoxide. *Journal of Non-Crystalline Solids*, 86, 231-240.
 179. Leaustic, A., Babonneau, F., & Livage, J. (1989). Structural investigation of the hydrolysis-condensation process of Titanium alkoxides $Ti(OR)_4$ (OR = OPri, OEt) Modified by Acetylacetone. 1. Study of the alkoxide modification. *Chemistry of Materials*, 1, 240-247.
 180. Leaustic, A., Babonneau, F., & Livage, J. (1989). Structural investigation of the hydrolysis-condensation process of Titanium alkoxides $Ti(OR)_4$ (OR = OPri, OEt) Modified by Acetylacetone. 2. From the modifies precursor to the colloids. *Chemistry of Materials*, 1, 248-252.

181. Schmidt, H. (1988). Chemistry of material preparation by the sol-gel process. *Journal of Non-Crystalline Solids*, 100, 51-64.
182. Ribot, F., Toledano, P., & Sanchez, C. (1991). Hydrolysis-Condensation Process of beta-Diketonates-Modified Cerium(IV) Isopropoxide. *Chemistry of Materials*, 3, 759-764.
183. Sanchez, C., Livage, J., Henry, M., & Babonneau, F. (1988). Chemical modification of alkoxide precursors. *Journal of Non-Crystalline Solids*, 100, 65-76.
184. Brown, D. (2002). *The chemical bond in inorganic chemistry-the bond valence model*. Oxford: Oxford University Press.
185. Murphy, J. E., Beard, M. C., Norman, A. G., Ahrenkiel, S. P., Johnson, J. C., Yu, P., Micic, O. I., Ellingson, R. J., & Nozik, A. J. (2006). PbTe Colloidal Nanocrystals: Synthesis, Characterization, and Multiple Exciton Generation. *J. Am. Chem. Soc.*, 128, 3241-3247.
186. Lamer, V. K. & Dinegar, R. H. (1950). Theory, production and mechanism of formation of monodispersed hydrosols. *Journal of the American Chemical Society*, 72, 4847-4854.
187. Lee, S.-M., Cho, S.-N., & Cheon, J. (2003). Anisotropic shape control of colloidal inorganic nanocrystals. *Advanced Materials*, 15, 441-444.
188. Attard, G. & Barnes, C. (1998). *Surfaces*. Oxford: Oxford University Press.
189. Lu, W., Fang, J., Stokes, K. L., & Lin, J. (2004). Shape Evolution and Self Assembly of Monodisperse PbTe Nanocrystals. *J. Am. Chem. Soc.*, 126, 11798-11799.
190. Jun, Y.-w., Lee, J.-H., Choi, J.-s., & Cheon, J. (2005). Symmetry-Controlled Colloidal Nanocrystals: Nonhydrolytic Chemical Synthesis and Shape Determining Parameters. *J. Phys. Chem. B*, 109, 14795-14806.
191. Wang, Z. L. (2000). Transmission Electron Microscopy of Shape-Controlled Nanocrystals and Their Assemblies. *J. Phys. Chem. B*, 104, 1153-1175.
192. Feng, X., Sayle, D. C., Wang, Z. L., Paras, M. S., Santora, B., Sutorik, A. C., Sayle, T. X. T., Yang, Y., Ding, Y., Wang, X., & Her, Y.-S. (2006). Converting ceria polyhedral nanoparticles into single-crystal nanospheres. *Science*, 312, 1504-1508.
193. Bowers II, M. J., McBride, J. R., & Rosenthal, S. J. (2005). White-Light Emission from Magic-Sized Cadmium Selenide Nanocrystals. *Journal of the American Chemical Society*, 127, 15378-15379.
194. Achermann, M., Petruska, M. A., Kos, S., Smith, D. L., Koleske, D. D., & Klimov, V. I. (2004). Energy-transfer pumping of semiconductor nanocrystals using an epitaxial quantum well. *Nature*, 429, 642-646.

195. Mueller, A. H., Petruska, M. A., Achermann, M., Werder, D. J., Akhadow, E. A., Koleske, D. D., Hoffbauer, M. A., & Klimov, V. I. (2005). Multicolor Light-Emitting Diodes Based on Semiconductor Nanocrystals Encapsulated in GaN Charge Injection Layers. *Nano Lett.*, 5, 1039-1044.
196. Su, L. T., Tok, A. I. Y., Boey, F. Y. C., Zhang, X. H., Woodhead, J. L., & Summers, C. J. (2007). Photoluminescence phenomena of Ce^{3+} -doped $\text{Y}_3\text{Al}_5\text{O}_{12}$ nanophosphors. *Journal of Applied Physics*, 102, 083541.
197. Praline, G., Koel, B. E., Hance, R. L., Lee, H.-I., & White, J. M. (1980). X-Ray photoelectron study of the reaction of oxygen with cerium. *Journal of Electron Spectroscopy and Related Phenomena*, 21, 17-30.
198. Iacona, F., Franzo, G., & Spinella, C. (2000). Correlation between luminescence and structural properties of Si nanocrystals. *Journal of Applied Physics*, 87, 1295-1303.
199. Hodes, G. (2007). When small is different: Some recent advances in concepts and applications of nanoscale phenomena. *Advanced Materials*, 19, 639-655.
200. Raukas, M., Basun, S. A., Schail, W. v., Yen, W. M., & Happek, U. (1996). Luminescence efficiency of cerium doped insulators: The role of electron transfer processes. *Applied Physics Letter*, 69, 3300-3302.
201. Capobianco, J. A., Vetrone, F., Alesio, T. D., Tessari, G., Speghini, A., & Bettinelli, M. (2000). Optical spectroscopy of nanocrystalline cubic $\text{Y}_2\text{O}_3:\text{Er}^{3+}$ obtained by combustion synthesis. *Physical Chemistry Chemical Physics*, 2, 3203-3207.
202. Zhou, P., Yu, X., Yang, L., Yang, S., & Gao, W. (2007). Synthesis of $\text{Y}_2\text{Si}_2\text{O}_7:\text{Eu}$ nanocrystal and its optical properties. *Journal of Luminescence*, 124, 241-244.
203. Slack, G. A., Dole, S. L., Tsoukala, V., & Nolas, G. S. (1994). Optical absorption spectrum of trivalent cerium in Y_2O_3 , $\text{Ba}_2\text{GdTaO}_6$, ThO_2 , and related compounds. *Journal of the Optical Society of America B*, 11, 961-974.
204. Di Valentin, C., Ricci, D., Pacchioni, G., Chiesa, M., Paganini, M. C., & Giamello, E. (2002). O- radical anions on polycrystalline MgO. *Surface Science*, 521, 104-116.
205. Yang, H. & Holloway, P. H. (2003). Enhanced photoluminescence from $\text{CdS}:\text{Mn}/\text{ZnS}$ core/shell quantum dots. *Applied Physics Letters*, 82, 1965.
206. Cao, L., Zhang, J., Ren, S., & Huang, S. (2002). Luminescence enhancement of core-shell $\text{ZnS}:\text{Mn}/\text{ZnS}$ nanoparticles. *Applied Physics Letters*, 80, 4300.
207. Brus, L. (1986). Electronic wave functions in semiconductor clusters: experiment and theory. *J. Phys. Chem.*, 90, 2555-2560.

208. Henderson, B. & Imbusch, G. F. (1989). *Optical Spectroscopy of Inorganic Solids*. Oxford: Clarendon Press.
209. Sun, H. D., Makino, T., Segawa, Y., Kawasaki, M., Ohtomo, A., Tamura, K., & Koinuma, H. (2001). Biexciton emission from ZnO/Zn_{0.74}Mg_{0.26}O multiquantum wells. *Applied Physics Letters*, 78, 3385-3387.
210. Batentschuk, M., Osvet, A., Schierner, G., Klier, A., Schneider, J., & Winnacker, A. (2004). Simultaneous excitation of Ce³⁺ and Eu³⁺ ions in Tb₃Al₅O₁₂. *Radiation Measurements*, 38, 539-543.

Appendix A: Crystallography of YAG: Ce³⁺

The electronic structure of the rare-earth ions determines the absorption and emission wavelengths of the phosphors. This electronic structure is, in turn depends on the local crystal environment. Any changes of the bonding with the surrounding ions will affect the electronic structure. For example, the luminescence of Ce³⁺ varies from one host lattice to another due to the strong influences from the local crystal environment [1, 2]. Hence, in this appendix, the crystallography of the bulk YAG: Ce³⁺ will be reviewed.

The crystal chemistry of yttrium aluminium garnet (YAG)

A YAG crystal has a general formula $[RE_3^c][Al_2^a][Al_3^d][O_{12}]$, where RE is the rare earth ions and the superscripts c , a , and d denote the Wyckoff symbols for the ions occupancy sites in the lattice [3-6]. The garnet crystallizes in the most symmetric space group of the cubic crystal system (space group number 230; $Ia\bar{3}d$). The highly symmetrical structure of the garnet can be envisioned through different projections of plane groups (Figure 1).

YAG is one of the large-form of crystals with complex unit cell. It is a body-centered cubic (BCC) crystal with a lattice constant of $a_0=12.00\text{\AA}$ (Table 1) [6, 7]. It has 160 atoms and 8 formula units per unit cell. Each formula unit consists of trivalent cations arranged on a BCC lattice with c and d ions lying on the faces. Each a and d ion occupies an octahedral site (AlO_6) and tetrahedral sites

(AlO_4), respectively. Each c ion, being the larger ion, is coordinated by 8 oxygen ions forming a severe distorted cube (Figure 2). This distortion has caused the cube to form twelve triangular faces; hence it is also known as triangular dodecahedron.

Polyhedral topology in YAG lattice structure

The highly symmetrical structure of YAG can be envisioned from the topology of the lattice. The tetrahedra and octahedra are linked by sharing all corners (Figure 3). The linkage is such that each octahedron is connected to another six octahedra through the corner-sharing tetrahedra and each tetrahedron shares corners with four octahedra. In YAG, the polyhedrals are also connected via edges. Each tetrahedron and octahedron shares edges with two and six triangular dodecahedra, respectively. Each triangular dodecahedron which in turn, shared edges with four octahedra, two tetrahedra, and four other triangular dodecahedra (Figure 4 and 5).

Ce^{3+} occupies the triangular dodecahedral site in YAG lattice, that is, it substitutes the yttrium ion. As mentioned previously, the triangular dodecahedron is a distorted cube (with CsCl type of coordination) with four short (d_{8-s}) and four long (d_{8-l}) bond distances ($RE^{3+}-O^{2-}$) (Figure 5). On average, the $Y^{3+}-O^{2-}$ distance is 2.37Å [6].

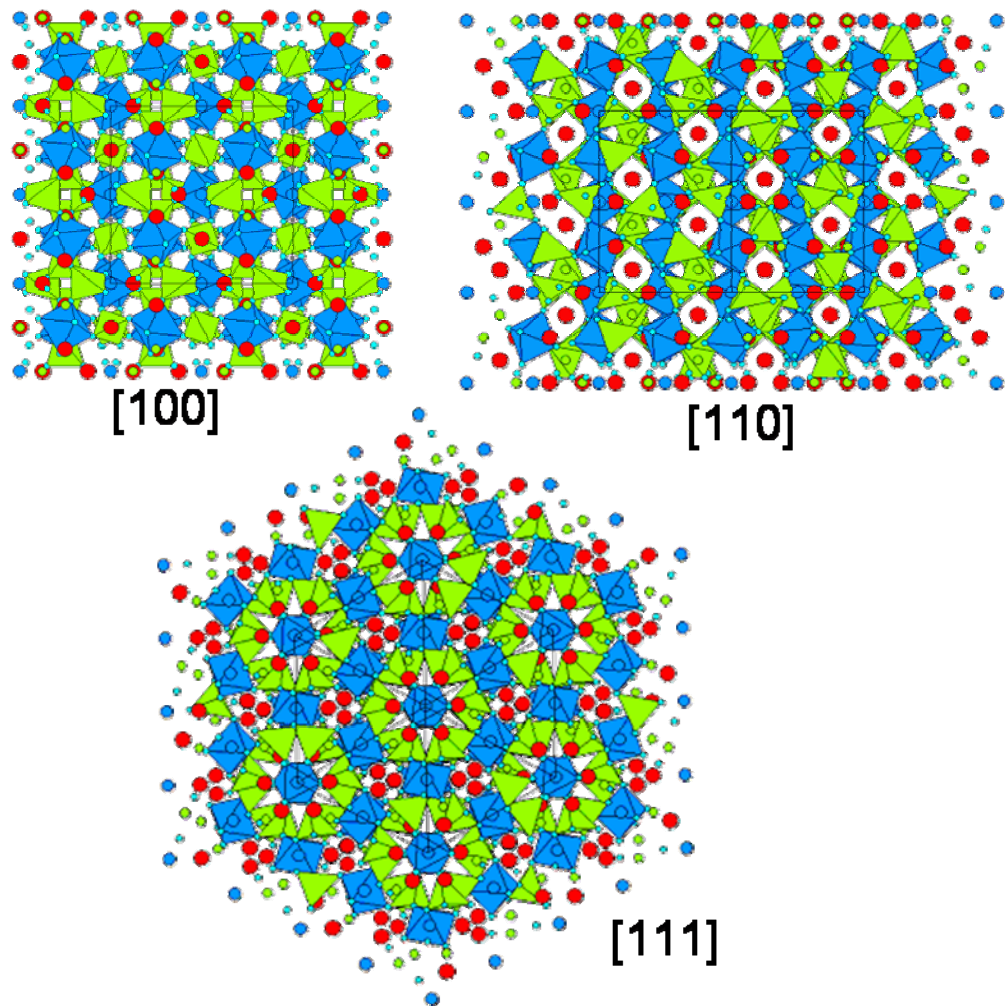


Figure 1: YAG host lattice at different projections view

Table 1: Structural parameters of the YAG [6]

$$Y_3Al_5O_{12} \text{ (Garnet),}$$

$$Ia-3d \text{ (230), } a=12.0031\text{\AA}$$

Atom	Site	x	y	z
Y	24c	1/8	0	1/4
Al(1)	16a	0	0	0
Al(2)	24d	3/8	0	0.25
O	96h	0.97	0.05	0.15

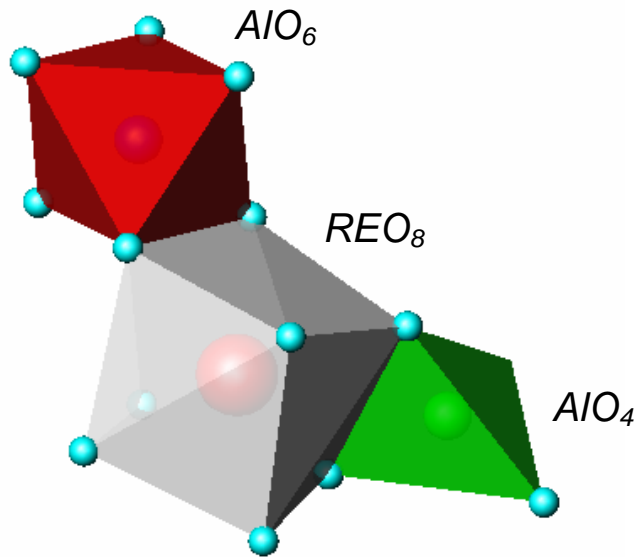


Figure 2: A simplified garnet structure presented as coordination polyhedral

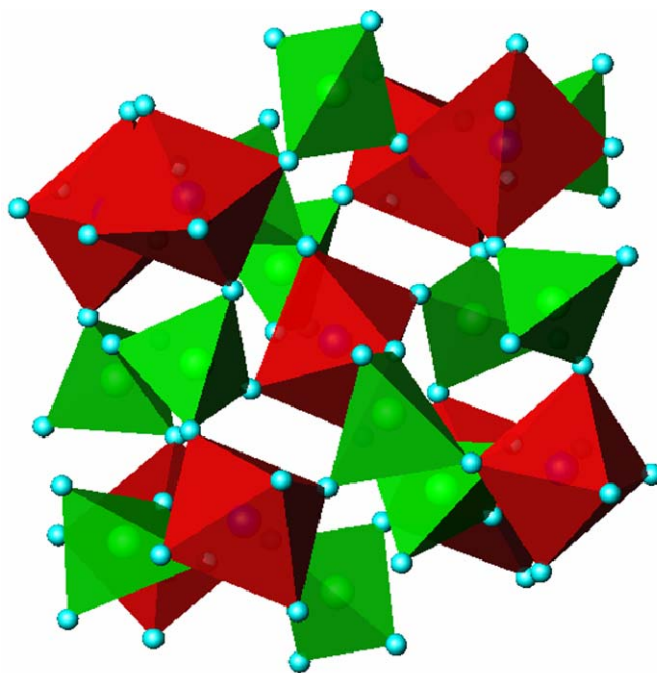


Figure 3: Corner sharing of the octahedra and tetrahedra

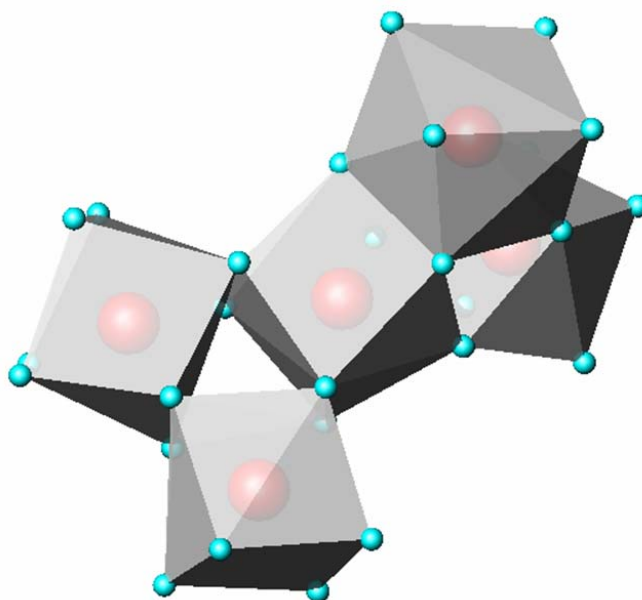


Figure 4: Edge sharing of the triangular dodecahedra

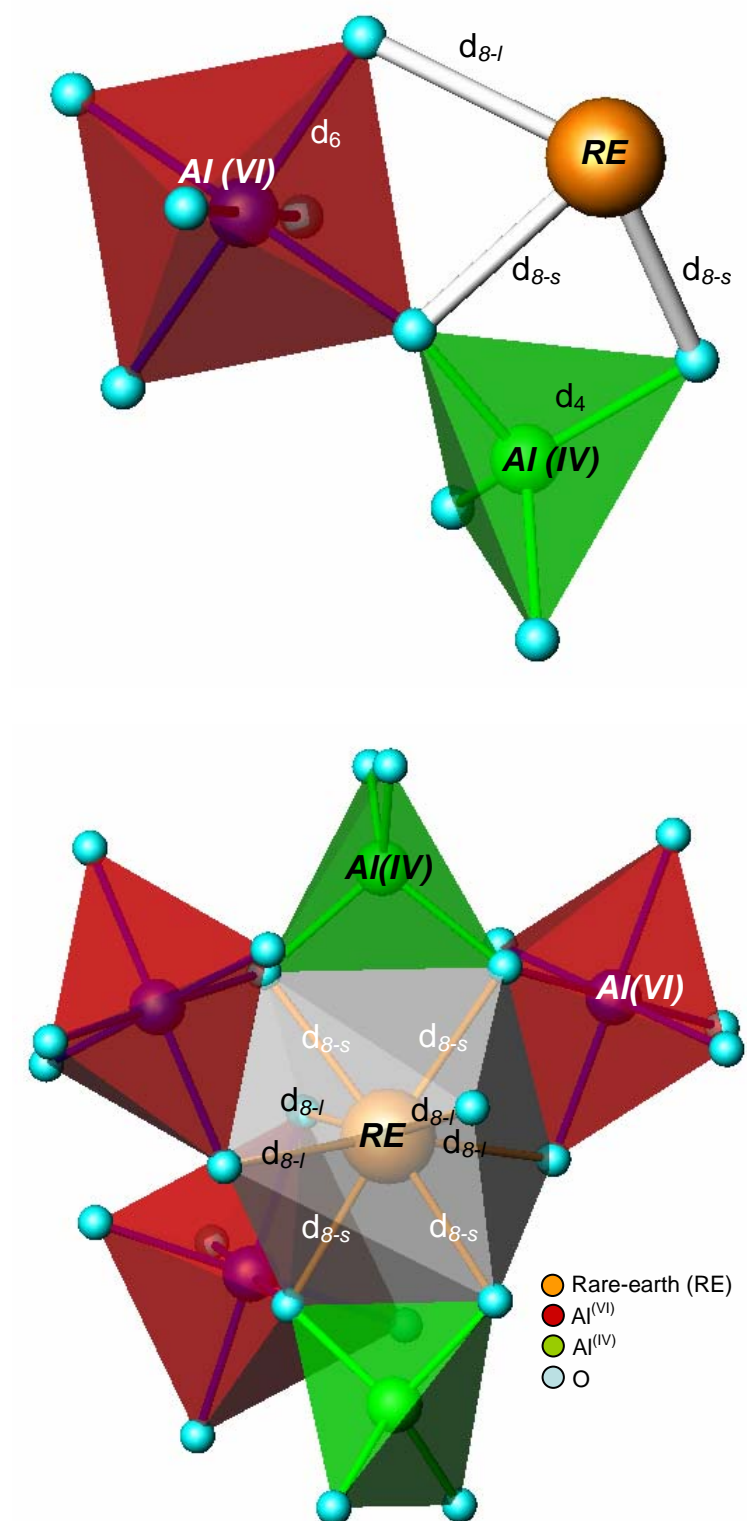


Figure 5: Interatomic distances in the YAG structure (Note: One of the octahedra is omitted in the figure (below) so that the bonds in REO_8 can be shown clearly)

References

1. Van Uitert, L. G. (1984). An empirical relation fitting the position in energy of the lower d-band edge for Eu²⁺ or Ce³⁺ in various compounds. *Journal of Luminescence*, 29, 1-9.
2. Dorenbos, P. (2002). 5d-level energies of Ce³⁺ and the crystalline environment. IV. Aluminates and "simple" oxides. *Journal of Luminescence*, 99, 283-299.
3. Kingery, W. D., Bowen, H. K., & Uhlmann, D. R. (1976). *Introduction to ceramics*. New York: John Wiley & Sons.
4. Hahn, T. (1996). *International Crystallography Table*. Dordrecht: Kluwer Academic Publishers.
5. Jaffe, H. W. (1988). *Crystal chemistry and refractivity*. Cambridge: Cambridge University Press.
6. Rodic, D., Mitric, M., Tellgren, R., & Rundlof, H. (2001). The cation distribution and magnetic structure of Y₃Fe_{5-x}Al_xO₁₂. *Journal of Magnetism and Magnetic Materials*, 232, 1-8.
7. Dobrzycki, L., Bulska, E., Pawlak, D. A., Frukacz, Z., & Wozniak, K. (2004). Structure of YAG Crystals Doped/Substituted with Erbium and Ytterbium. *Inorg. Chem.*, 43, 7656-7664.

Appendix B: The Brownian oscillator model

The linear absorption and the photoluminescence spectra line shapes can be calculated from a spectral broadening function $g(t)$:

$$\sigma_{BO}(\omega) = \frac{1}{\pi} \text{Re} \int_0^\infty dt \exp \left[i \left(\omega - \omega_{eg}^0 - \lambda_j \right) t - g(t) \right] \quad (\text{B1})$$

$$I_{BO}(\omega) = \frac{1}{\pi} \text{Re} \int_0^\infty \exp \left[i \left(\omega - \omega_{eg}^0 + \lambda \right) t - g^*(t) \right] dt \quad (\text{B2})$$

where ω_{eg}^0 is the pure electronic transition frequency or the zero-phonon line, $\lambda = S\hbar\omega_j$ is the Stokes shift, $g^*(t)$ is the complex conjugate of the spectral broadening function $g(t)$, $g(t)$ is related to the polarisation of the material system and is shown in the following:

A Taylor expansion of the polarisation in powers of the radiation field $E(r, t)$ is:

$$P(r, t) = P^{(1)}(r, t) + P^{(2)}(r, t) + P^{(3)}(r, t) + \dots \quad (\text{B3})$$

The term $P^{(1)}(r, t)$ is for linear optics. Hence, the linear response function $S^{(1)}(r, t)$ is defined as the first-order susceptibility via the polarisation $P^{(1)}(r, t)$:

$$P^{(1)}(r, t) = \int_0^\infty dt_1 S^{(1)}(r, t_1) E(r, t - t_1) \quad (\text{B4})$$

and the susceptibility takes the form:

$$S^{(1)}(t_1) = \frac{i}{\hbar} \theta(t) [R(t) - R^*(t)] \quad (\text{B5})$$

where

$$R(t) = \exp(-i\omega_{eg}t) \exp[-g(t)] \quad (\text{B6})$$

and

$$\omega_{eg} = \omega_{eg}^0 + \langle U \rho_g \rangle \quad (\text{B7})$$

Here U is the collective bath coordinate that is responsible for the spectral shift and broadening, and the ρ_g is the ground-state vibrational density matrix:

$$\rho_g = \frac{|g\rangle\langle g| \exp(-\beta \hat{H}_g)}{\text{Tr}[\exp(-\beta \hat{H}_g)]} \quad (\text{B8})$$

where $\beta=1/k_B T$ (k_B is the Boltzman constant) which reflects the thermal population of the bath modes.

The spectral broadening function $g(t)$ can be expressed as the frequency-domain correlation function $C''(\omega)$ using the truncation of the second-order cumulant expansion:

$$g(t) = \frac{1}{2\pi} \int_{-\infty}^{\infty} d\omega \frac{C''(\omega)}{\omega^2} \left[1 + \coth\left(\frac{\beta\hbar\omega}{2}\right) \right] \left[e^{-i\omega t} + i\omega t - 1 \right] \quad (\text{B9})$$

with the correlation function:

$$C''(\omega) = -i \int_{-\infty}^{\infty} dt e^{-i\omega t} \tilde{C}(t) \quad (\text{B10})$$

and the parameters of the Hamiltonian are transferred to a correlation function:

$$\tilde{C}(t) = -\frac{1}{2\hbar^2} \left[\langle U(t)U(0)\rho_g \rangle - \langle U(0)U(t)\rho_g \rangle \right] \quad (\text{B11})$$

where $U(t)$ is the operator U in the interaction representation and ρ_g is the ground-state vibrational density matrix. $C''(\omega)$ is in fact the imaginary part of the frequency-domain correlation function $C(\omega)$ whose real part $C'(\omega)$ related to $C''(\omega)$ by

$$C'(\omega) = \coth\frac{\beta\hbar\omega}{2} C''(\omega) \quad (\text{B12})$$

The correlation function $C''(\omega)$ is a collective contribution from each primary oscillator:

$$C''(\omega) = \sum_j C''_j(\omega) \quad (\text{B13})$$

where the Fourier transform of the correlation function has an imaginary part which is the spectral density [1]:

$$C''(\omega) = \frac{2\lambda_j \omega_j^2 \omega \gamma_j(\omega)}{\omega^2 \gamma_j^2(\omega) + \left(\omega_j^2 + \omega \sum_j (\omega) - \omega^2\right)^2} \quad (\text{B14})$$

Here $2\lambda_j$ is the j th mode collective contribution to the Stokes shift.

$$2\lambda_j = \frac{m_j \omega_j^2 d_j^2}{\hbar} \quad (\text{B15})$$

Another expression is $\lambda_j = S_j \hbar \omega_j$, where Huang-Rhys factor (S) indicating the electron-LO-phonon coupling strength[2]. S_j can vary from less than unity for weak coupling case to equal and to greater than unity for medium and strong coupling cases, respectively. For example, the InGaN/GaN quantum dots, the photoluminescence spectrum of the optical center is weakly coupled to the lattice vibrational mode 740 cm^{-1} with $S_j=0.20$ [3].

The spectral distribution of the coupling is:

$$\gamma_j(\omega) = \frac{\pi}{m_j} \sum_n \frac{c_{nj}^2}{2m_n \omega_n^2} \left[\delta(\omega - \omega_n) + \delta(\omega + \omega_n) \right] \quad (\text{B16})$$

and the real part $\Sigma_j(\omega)$ of the self-energy is related to $\gamma_j(\omega)$ by the Kramers-Kronig relation [4, 5]:

$$\sum_j(\omega) = -\frac{1}{\pi} PP \int_{-\infty}^{\infty} d\omega' \frac{\gamma_j(\omega')}{\omega' - \omega} \quad (\text{B17})$$

where PP represents the Cauchy principal part. Therefore, this gives:

$$\sum_j(\omega) = \frac{1}{m_j} PP \sum_n \frac{c_{nj}^2}{2m_n \omega_n^2} \left[\frac{1}{\omega - \omega_n + i\eta} + \frac{1}{\omega + \omega_n + i\eta} \right] \quad (\text{B18})$$

where the η is infinitesimal.

In order to facilitate the numerical calculations, the real and imaginary parts of the spectral broadening function $g(t) = g'(t) + g''(t)$ can be expressed in terms of $C''(\omega)$:

$$g'(t) = \frac{1}{\pi} \int_0^{\infty} d\omega \frac{1 - \cos(\omega t)}{\omega^2} \coth(\beta \hbar \omega / 2) C''(\omega) \quad (\text{B19})$$

$$g''(t) = \frac{i}{\pi} \int_0^{\infty} d\omega \frac{\sin(\omega t) - \omega t}{\omega^2} C''(\omega) \quad (\text{B20})$$

References:

1. Zhao, Y., Chernyak, V., & Mukamel, S. (1998). *J. Phys. Chem. A*, 102, 6614.
2. Huang, K. & Rhys, A. (1950). Theory of Light Absorption and Non-Radiative Transitions in F-Centres. *Proceedings of the Royal Society of London. Series A, Mathematical and Physical Sciences*, 204, 406-423.
3. Xu, S. J., Li, G. Q., Wang, Y. J., Zhao, Y., Chen, G. H., Zhao, D. G., Zhu, J. J., Yang, H., Yu, D. P., & Wang, J. N. (2006). Quantum dissipation and

- broadening mechanisms due to electron-phonon interactions in self-formed InGaN quantum dots. *Applied Physics Letters*, 88, 083123.
4. Avouris, P., Campion, A., & El-Sayed, M. A. (1977). *J. Chem. Phys.*, 3397.
 5. Jackson, J. D. (1975). *Classical electrodynamics*. New York: John Wiley & Sons